Magnetomechanical interactions in clinical MRI cryostats

DISSERTATION ZUR ERLANGUNG DES DOKTORGRADES
DER NATURWISSENSCHAFTEN (DR. RER. NAT.)
DER FAKULTÄT FÜR PHYSIK
DER UNIVERSITÄT REGENSBURG

vorgelegt von

Christopher Andreas Ströhlein aus

Nürnberg

im Jahr 2018

Promotionsgesuch eingereicht am: 15. Oktober 2018
Die Arbeit wurde angeleitet von: PD Dr. Wolfgang Nitz

Prüfungsausschuss:
Prof. Dr. Josef Zweck
Prof. Dr. Rupert Huber
Prof. Dr. Christoph Lehner

Datum Promotionskolloquium: 26 Juli 2019

Abstract

Magnetic Resonance Imaging (MRI) is one of the most utilized imaging modalities in medical diagnosis. Key components of common clinical MRI systems are the superconducting main coils and the so-called 'gradient coils'. The former generate a strong static magnetic field (several Tesla of field strength) while the latter can be operated dynamically, producing linear magnetic field gradients. For maintaining the superconductive state, the main coils are cooled with liquid helium, which is enclosed in several metallic cylinders. This so-called cryostat is to some extent assembled with materials possessing high electrical and thermal conductivity. The dynamic fields generated by the gradient coils will induce eddy currents within these materials. Lorentz forces from the interaction of these currents with the static main magnetic field lead to mechanical vibrations of the conductive parts. These vibrations in turn induce eddy currents according to Lenz's law, as the conductors move within a magnetic field. The fields emitted by these additional eddy currents initiate the described magnetomechanical interaction process on other conductive parts in the MRI system. Consequences of this magnetomechanical coupling are phenomena like image artifacts or heat loads caused by eddy current losses which show a strong resonant behavior. Whereas a dependency of eddy current losses on magnetomechanical interactions was already reported and could also be simulated for simple configurations, imaging artifacts as a cause of magnetomechanical effects were so far not described. Purpose of this work is to demonstrate this connection for the example of so-called 'ghosting artifacts' in echo planar imaging and to provide methods for analyzing and mitigating negative magnetomechanical implications.

Since a general analytical solution of the complex (non-linear) coupled mechanisms is not available, numerical simulations via finite elements are employed to describe and analyze the system behavior. Former investigations of this kind have been limited to axial symmetric gradient coils reducing the problem to two dimensions. This thesis expands the analysis to coil shapes demanding a complete three-dimensional approach. The developed framework is successfully applied to reproduce and reduce cryostat

resonances excited by the magnetomechanical coupling that leads to excessive eddy current losses. Capabilities, limitations and the reliability of the presented simulation setup are discussed.

The system understanding obtained from the finite element simulations is used to develop a fast and drastically simplified algorithm to calculate estimations concerning the magnetomechanical behavior of the MRI system. Therefore, it is assumed that the main characteristics of the system are described by modal participation factors of the cryogenic shielding, reacting to the excitation generated by the gradient coil stray field. This method allows the identification of crucial mode shapes concerning eddy current losses as well as ghosting artifacts. Measurements verify that a reduction of the ascribed participation factors leads to a clear mitigation of the related effects.

An experimental evidence of the imaging relevant influence of magnetomechanical interactions is provided with a series of measurements using magnetic resonance techniques combined with direct magnetic flux measurements utilizing a pickup coil. The results allow to establish a dependency between the ghosting provoking magnetic fields in the imaging volume of the MRI system and fields emitted from movements of the cryostat.

List of abbreviations

a.u.	arbitrary unit
App.	appendix
CPU	central processing unit
CS	cryogenic shield - highly conductive part of the MRI cryostat
ECL	eddy current loss - mostly considered on the HeV
e.g.	example(s) given
EPI	echo-planar-imaging - MR imaging technique
emf	electromotive force
Eq.	equation
FE	finite element
FEM	finite element method
FID	free induction decay
Fig.	figure
FOV	field of view - spatial volume suitable for MR imaging
GC	gradient coil - resistive coil, producing a magnetic field gradient
HeV	helium-vessel - inner part of the MRI cryostat, containing liquid helium
i.e.	that means (from latin 'id est')
MR	magnetic resonance
MRI	magnetic resonance imaging
OVC	outer vacuum chamber - outer shell of the MRI cryostat
PF	participation factor
pg.	pages
PT	prototype
ref.	reference
RF	radio frequency
Sec.	section
Tab.	table

Notation

In general bold symbols indicate vectors and an additional 'hat-symbol' stands for matrices. Symbols written regular are scalars or amplitudes of vectors. If a quantity is indexed with a symbol representing a dimensions of a vector space, it describes the amplitude of the given quantity in the according dimension, e.g. u_x indicates the amplitude of $\boldsymbol{u}$ in x-direction.

a	amplitude of additional signal modulation in S_a	E_p	potential energy of a proton within a magnetic field
a_n, b_n	Fourier coefficients	ΔE	energy difference of two proton spin states
$\boldsymbol{A}$	magnetic vector potential	$\boldsymbol{f}$	force density
$\mathcal{A}(3,3)$	real valued average of spherical harmonics $Y_{3,3}$ and $Y_{3,-3}$	$\boldsymbol{f}_{\text{PF}}$	Lorentz force density used to calculate PFs
$\boldsymbol{B}$	magnetic field	$\boldsymbol{F}$	force
$\boldsymbol{B_0}$	static magnetic background field	$\boldsymbol{F_P}$	Lorentz force due to $\boldsymbol{I_P}$
$\boldsymbol{B_1}$	RF field	$\mathcal{F}$	fitted exponential function
$\boldsymbol{B}_e$	magnetic field disturbance caused by eddy currents	$\boldsymbol{G}$	linear magnetic field gradient of B_z in FOV
$\boldsymbol{B_G}$	magnetic fields generated by the GC	$\boldsymbol{G}_{\text{phase}}$	phase encoding gradient
$\boldsymbol{B_{G,0}}$	superposition of gradient fields and $\boldsymbol{B_0}$	$\boldsymbol{G}_{\text{read}}$	read-out gradient
$\hat{\boldsymbol{\mathcal{B}}}$	differential operator (see Eq. 2.38)	$\boldsymbol{G}_{\text{slice}}$	slice encoding gradient
c, c_x, c_y	polynominal coefficients for Eq. 4.4 - 4.7	$\hbar$	reduced Planck constant
c_a, c_b	fit coefficients for exponential function $\mathcal{F}$	I	electrical current
$\hat{\boldsymbol{c}}$	tensor of elasticity moduli	I_0	amplitude of the electrical current
$\mathcal{C}$	convolution of $\mathcal{M}$ and $\mathcal{V}$	I_{ECL}	electrical current responsible for eddy current losses in the cryostat
$\hat{\boldsymbol{C}}_{\boldsymbol{uu}}$, $\hat{\boldsymbol{C}}_{\boldsymbol{Au}}$, $\hat{\boldsymbol{C}}_{\boldsymbol{uA}}$	magnetomechanical coupling matrices in harmonic matrix solution	$\boldsymbol{I_P}$	primary eddy currents
		$\boldsymbol{I_S}$	secondary eddy currents
$\boldsymbol{e}$	unit vector	$\mathcal{I}$	frequency spectrum of the electrical current
$\boldsymbol{E}$	electric field	$\boldsymbol{J}$	electrical current density
		$\hat{\boldsymbol{\mathcal{J}}}$	FE electrical current matrix
		$\boldsymbol{k}$	position vector in k-space

k_B	Boltzmann constant
k_x, k_y, k_z	k-space coordinates equivalent to x, y and z in real space
Δk_y	distance of neighboring k-space voxel in k_y-direction
K	scalar distribution in k-space
$\hat{\boldsymbol{\mathcal{K}}}_{\boldsymbol{A}}$	FE magnetic stiffness matrix
$\hat{\boldsymbol{\mathcal{K}}}_{\boldsymbol{u}}$	FE mechanical stiffness matrix
l_b	length of local modal extrema
L	inductance of eddy current paths
M_z^0	z-component of the macroscopic magnetization in equilibrium
$\boldsymbol{M}$	macroscopic magnetization
$\hat{\boldsymbol{M}}$	FE mass matrix
$\mathcal{M}$	signal measured with pickup coil
n	counting variable
n_d	number of elements along the thickness of a cryostat vessel
N_p, N_{ap}	number of parallel and antiparallel spins
N_x, N_y	number of image voxels in x- and y-direction
N_z, N_φ	number of mode extrema in axial or circumferential direction on a cylinder
ΔN	superior number of parallel spins
ΔN_0	superior number of parallel spins in equilibrium
P	scalar distribution in real space
$\mathcal{P}_l^m$	associated Legendre function
PF_q	modal participation factor of mode q
q	mode number
$\boldsymbol{Q_1}, \boldsymbol{Q_2}, \boldsymbol{Q_3}$	terms neglected in the harmonic matrix coupled solution (see Eqs. 2.62-2.64)
$\boldsymbol{r}$	position vector
r_c, φ_c, z	cylindrical coordinates (see App. A.2)
r_s, φ_s, θ_s	spherical coordinates (see App. A.2)
R_α, R_β	Rayleigh damping parameters
$\boldsymbol{R}$	velocity proportional damping
$\hat{\boldsymbol{R}}$	FE velocity proportional damping matrix
s	magnetic quantum number
S	MRI signal
S_a	amplitude modulated MRI signal
$\boldsymbol{S}$	mechanical strain
$\hat{\boldsymbol{S}}$	mechanical strain tensor
t	time
t_0	time point of RF excitation
t_{Gy}	duration of G_y application
t_α	RF duration to achieve the flip angle α
Δt	time step size used for the transient simulations
T	period of a periodic function
T_1, T_2, T_2^*	time constants describing the relaxation process of proton magnetization
T_E	echo time
$T_{E_{\mathrm{EPI}}}$	time between EPI echos
T_{th}	temperature
$\boldsymbol{u}$	mechanical displacement
U_P	voltage induced by dynamic $\boldsymbol{B_G}$; generating $\boldsymbol{I_P}$

$\mathcal{V}$	'virtual' sinusoidal signal with phase and frequency of the gradient excitation
$\mathcal{V}_0$	amplitude of $\mathcal{V}$
x, y, z	cartesian coordinates
x', y', z'	cartesian coordinates of a rotating coordinate system revolving around z'
y_{max}	half of the MR image size in y-direction
Δy	a variation in y-direction
$Y_{l,m}$	spherical harmonics
Δz	a variation in z-direction
α	flip angle of magnetization
γ	electric conductivity
γ_B	gyromagnetic ratio
$\hat{\boldsymbol{\gamma}}_{\boldsymbol{AA}}$	FE electric conductivity matrix
$\boldsymbol{\Gamma}$	quantum mechanical spin
δ	thickness of the CS vessel
δ_q	$\tan\delta_q$ represents the loss factor for the q-th eigenfrequency
ϵ	electric permittivity
η	ratio of N_p and N_{ap}
ϑ	temporal phase shift between the GC fields and the eddy current field disturbance
κ	tilting angle at knots of modal shapes
$\boldsymbol{\mu}$	magnetic momentum or magnetization
ν	magnetic reluctivity
ρ	spin density
ρ_m	mass density
$\boldsymbol{\sigma}$	mechanical stress
$\hat{\boldsymbol{\sigma}}$	mechanical stress tensor
τ	decay time constant of oscillations
Φ	phase of the magnetization
Φ_e	phase of the magnetization generated by field disturbances in the FOV
Φ_G	phase of the magnetization generated by gradient activity
ξ	volume of an FEM element
ω	angular frequency
ω_L	Larmor frequency
ω_n	n-th harmonic of ω_{EPI}
ω_{EPI}	frequency of EPI read-out gradient
ω_q	q-th eigenfrequency
$\Delta\omega$	difference of ω and ω_L

Table of contents

1 Introduction

Magnetic resonance imaging (MRI) is used to document tissue properties, like the proton distribution, diffusion rates or susceptibility. Such tissue characteristics allow to distinguish normal anatomy from pathologic changes and have become an indispensable tool in modern diagnostic imaging since the first MRI systems became available in 1983.

The information about the tissue properties is extracted from the behavior of the nuclear spin within a superposition of magnetic fields. In order to observe the nuclear spin, a (high) magnetic field is necessary. For imaging purposes, it is commonly desired to bare a constant field during measurements and ideally homogeneous within the investigated volume. The so-called main magnetic field is generated via permanent magnets, resistive magnets or superconductive magnets. All types of these magnets are currently available, whereas the majority uses cylindrical superconducting magnets (see Fig. 1.1). This thesis focuses on those systems.
Additional dynamic magnetic field variations are required to enable the selective excitation of a specific location and to encode spatial information into the generated electromagnetic signal [1]. Those field variations are preferably spatially linear, describing a constant magnetic gradient field over the imaging volume. Hence, the coils carrying the responsible electrical currents are usually referred to as 'gradient coils' (GCs). Since spatial encoding is performed in three dimensions, three gradient coils are usually assembled producing orthogonal gradient fields named X-, Y- and Z-gradients.

As is well known, the dynamic switching of magnetic fields induces eddy currents in surrounding conductive material, counteracting on the changes of magnetic flux. The interaction of these currents with the static main magnetic field causes Lorentz forces which excite vibrations of the conductive components. Since these movements within the magnetic field change the magnetic flux through the conductive surfaces,

Figure 1.1 – Exemplary image of an MRI system with superconducting magnets, showing a lateral and frontal perspective.

additional eddy currents are induced, according to Lenz's law. The field emitted by these eddy currents in turn initiates the outlined process on other conductive parts in the MRI system, resulting in a complex magnetomechanically coupled system.

Any deviations from the desired magnetic field gradient, whether in space or in time, potentially create undesired artifacts within the MRI images. Content of this work is to demonstrate that the just described magnetomechanical interactions can cause significant disturbing field deviations, which interfere with the gradient activity. For this purpose a novel 3D finite element (FE) framework is presented, which is an expansion of a refined 2D approach based on techniques previously established by [2, 3]. The focus of the work done by [2, 3], concerning the magnetomechanical interactions, were the ohmic heat loads produced by the generated eddy currents. For the superconducting main magnets it is essential to maintain operating temperatures below the critical temperature of the superconductive material. To achieve this, the magnets are encapsulated in a cryostat and need active cooling. Reliable computed estimations of the influence of different geometries or material properties on this magnetomechanical process can save far more expensive experimental verifications.
Another 2D FE formulation dealing with this direct magnetomechanical coupling is described by [4]. Any other ansatz covering the problem with 3D simulations is currently not known to the author. The framework introduced with this thesis grants a deeper insight into the system behavior, improving the understanding of magnetome-

chanically induced eddy current losses and adding simulations considering fields emitted towards the imaging volume. This allows to identify dependencies and dominant effects responsible for the disturbing fields that interfere with the magnetic field gradients.

After summarizing the basic theoretical background of MRI, the magnetomechanical coupling and the utilized FE formalism, the transition from 2D to 3D FE-models will be described. Therefore, the eddy current loss simulations serve as benchmark for the validity of the method. It will be shown that the models are capable of supporting the GC design process on various measured prototype setups. The gathered information about the magnetomechanical interactions is then applied to reduce the dedicated generation of the gradient field disturbances, eliminating an actual image artifact.
As further proof of the effectiveness of the implemented changes, supplemental series of magnetic field measurements using MR methods and direct field measurements with a pickup coil are presented. The acquired results confirm theoretical considerations of the disturbing field properties and allow to reproduce the shape of the responsible movement inside the MRI system.

2 Background

2.1 MRI physics

2.1.1 Interaction of proton spins and static magnetic fields

For MR imaging the quantum mechanical proton spin represents the fundamental property of compounds or tissues that is exploited for tomography by the dedicated application of magnetic fields. The existence of a 'two-valuedness not describable classically' [5] describing a quantum property, later named spin, has been proposed by Wolfgang Pauli (Nobel Prize in Physics 1945) in order to explain the hyperfine structure of atomic spectra. Following this postulation the experimental verification with measurements is credited to Felix Bloch and Edward Purcell (Nobel Prize in Physics 1952). Utilizing the spin properties for imaging purposes was initiated by Paul Lauterbur and Peter Mansfield, who received the Nobel Prize 2003 in Physiology or Medicine for their discoveries concerning magnetic resonance imaging.

As a quantum mechanical quantity the spin can only adopt discrete values. Since the spin is also associated with a spatial direction, it is described as a vector with magnitude

$$|\mathbf{\Gamma}| = \sqrt{\Gamma(\Gamma+1)} \cdot \hbar \tag{2.1}$$

where $\hbar$ represents the reduced Planck constant[1] and Γ being half-integer or integer, called spin quantum number [6]. Of particular interest for MRI is hereby the ^{1}H-nucleus, a single proton. Protons are fermions, which possess a spin quantum number of $\frac{1}{2}$.

Knowing $\mathbf{\Gamma}$ and the particle specific gyromagnetic ratio γ_B, it is possible to determine

[1] Planck's constant h is of fundamental meaning for describing quantum mechanical behavior in mathematical context. $h/2\pi = \hbar = 6.58 \cdot 10^{-16}$ eV/s

the magnetic momentum

$$\boldsymbol{\mu} = \gamma_B \cdot \boldsymbol{\Gamma} \tag{2.2}$$

In the case of a magnetic field pointing in z-direction, the component Γ_z of $\boldsymbol{\Gamma}$ is quantized to

$$\Gamma_z = s \cdot \hbar \tag{2.3}$$

s being the magnetic quantum number that can range between $-\Gamma$ and $+\Gamma$ in steps of 1. Thus, $s \in \{-\frac{1}{2}, \frac{1}{2}\}$ applies for single protons.
Therewith, the energy $E_p(s)$ of a proton with quantum number s within an external magnetic field $\boldsymbol{B_0} = B_0\, \boldsymbol{e_z}$, can be calculated

$$E_p(s) = -\boldsymbol{B_0}\ \boldsymbol{\mu} = -B_0\mu_z = -\gamma_B B_0 s\hbar \tag{2.4}$$

Accordingly, this gives the difference in energy between the two spin states.
Each proton spin can only occupy the state parallel ($s = \frac{1}{2}$) or anti-parallel($s = -\frac{1}{2}$) to $\boldsymbol{B_0}$, which yields an energy difference of

$$\Delta E = \gamma_B B_0 \hbar \tag{2.5}$$

From this, one can already deduce, that the transition between the two states involves the absorption or respectively the disposal of ΔE from or to the environment of the proton. Electromagnetic radiation with the frequency [7]

$$\omega_L = \frac{\Delta E}{\hbar} = \gamma_B B_0 \tag{2.6}$$

is hence predestined to interact with the spins (resonance criterion). Such interactions are covered in section 2.1.2.

The presence of the static field leads to an expectation value of the spin state with a higher probability assigned to the parallel state, as it is the state with less energy. For a large collection of spins one can utilize the Fermi-Dirac distribution to describe the relation of the two spin states. At body temperature, as it is in the case of clinical MRI, the Fermi-Dirac distribution converges to Boltzmann's distribution [8]. Thus, the

relationship between the number of parallel and anti-parallel spins N_p and N_{ap} yields

$$\eta = \frac{N_p}{N_{ap}} = \exp\left(\frac{\Delta E}{k_B T_{\text{th}}}\right) \tag{2.7}$$

with the Boltzmann constant $k_B = 1.39 \cdot 10^{-23}$J/K and the temperature T_{th} of the spin ensemble in degrees Kelvin. Although the parallel state is more preferable for the spins, as it leads to a reduction in their overall energy, η is very close to one, since $\Delta E \ll k_B T_{\text{th}}$ holds for common MRI field strengths and T_{th} at body temperature.

Although the percentage of counterbalanced parallel spins is very high, the remaining unbalanced spins still possess enough magnetization to finally generate a measurable MRI signal, due to the commonly vast number of considered particles. The spin system exhibits a dynamic equilibrium with a superior number of parallel spins, which is directly proportional to the magnetic field magnitude B_0 [9]. At a magnetic field strength of 1.0 Tesla this yields a difference between parallel and anti-parallel spins in the range of 6 parts per million.

If the nuclear magnetization $\boldsymbol{\mu}$ is not parallel to $\boldsymbol{B_0}$ the equation of motion applies

$$\frac{d\boldsymbol{\mu}}{dt} = \gamma_B \boldsymbol{\mu} \times \boldsymbol{B_0} \tag{2.8}$$

leading to a precession movement of $\boldsymbol{\mu}$ around $\boldsymbol{B_0}$ (Fig. 2.1A). The precession of a magnetization moment around a magnetic field (initially described for circulating charged particles [10]) is known as Larmor-Precession with the Larmor-Frequency ω_L.
To facilitate the further treatment of this topic a rotating coordinate system (from stationary cartesian (x,y,z) to (x',y',z')) is introduced. Let z' and z be alined while x' and y' rotate around z with an angular velocity represented by a vector $\boldsymbol{\omega}$. This coordinate transformation demands to calculate the total derivative of $\boldsymbol{\mu}$ with respect to time as [11]

$$\frac{d\boldsymbol{\mu}}{dt} = \frac{\partial \boldsymbol{\mu}}{\partial t} + \boldsymbol{\omega} \times \boldsymbol{\mu} \tag{2.9}$$

Inserting in Eq. 2.8 gives

$$\frac{\partial \boldsymbol{\mu}}{\partial t} = \gamma_B \boldsymbol{\mu} \times \left(\boldsymbol{B_0} + \frac{\boldsymbol{\omega}}{\gamma_B}\right) \tag{2.10}$$

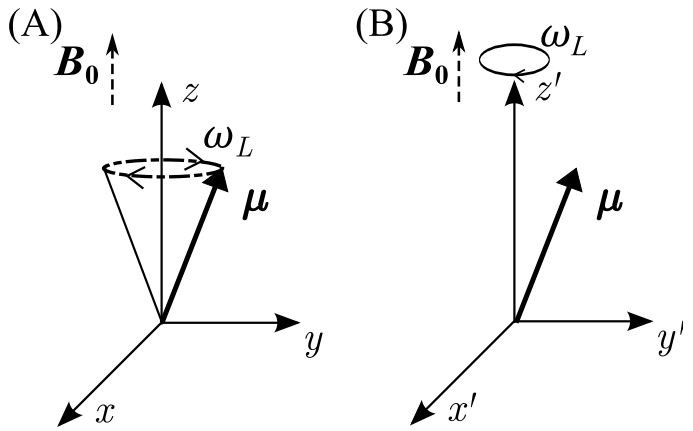

Figure 2.1 – (A) The precession of $\boldsymbol{\mu}$ around the external magnetic field $\boldsymbol{B_0}$ with the frequency $\omega_L = -\gamma_B B_0$. (B) $\boldsymbol{\mu}$ in a coordinate system rotating with ω_L around $z' = z$, so $\boldsymbol{\mu}$ constantly remains in the y'-z' plane.

This equation shows that it is convenient to chose the angular velocity of the rotating coordinate system as $\boldsymbol{\omega} = -\boldsymbol{\omega_L} = -\gamma_B \boldsymbol{B_0}$, since $\boldsymbol{\mu}$ remains constant in time with this choice (compare Fig. 2.1 B). A comparison of this condition to Eq. 2.6 shows that the Larmor-Frequency corresponds to the energy difference of the two spin eigenstates.
Quantum mechanics yields that the expectation value of the magnetization can obtain an arbitrary direction [7]. With $\boldsymbol{B_0}$ pointing in z direction the z-component of $\boldsymbol{\mu}$ has a higher probability to be parallel than anti-parallel, while the average x- and y-component of a multitude of protons in thermal equilibrium is zero. The resulting total magnetization $\boldsymbol{M}$, hence only possesses a z-component.

2.1.2 Interaction of the total magnetization with dynamic fields

So far, the description of the proton spin behavior (except for Eq. 2.7) was limited to the treatment of free unbound spins, meaning the protons were considered to have no contact to their environment (also called 'resort'). This treatment is now expanded and allows small field perturbations with frequencies in the neighborhood of ω_L. Thereby, the relevant energy levels of the system can be reduced to the two spin states (parallel and anti-parallel to $\boldsymbol{B_0}$) in good approximation [11].
Two possible interactions for the spins are distinguished. Either the resort compensates the energy difference $\Delta E \approx \hbar\omega_L$ necessary to change the spin state or a couple of two spins (one parallel one anti-parallel) exchange the energy and respectively change their

states. In the first case the spin-system losses or gains energy from the resort, while in the second case the energy of the spin-system is preserved.
In thermal equilibrium the superior number of parallel spins $\Delta N = N_p - N_{ap}$ is constant (ΔN_0) and defined by Eq. 2.7. Considering a situation when the system has been disturbed from its steady state, ΔN will return to equilibrium over time, following the equation

$$\frac{d\Delta N}{dt} = \frac{\Delta N_0 - \Delta N}{T_1} \tag{2.11}$$

where t represents time and T_1 denotes a time constant that is dependent on the environment of the regarded protons.
This process can also be described with the macroscopic magnetization $\boldsymbol{M}$. The disturbed state of the system can be represented by an arbitrarily oriented vector $\boldsymbol{M}(t)$. As explained in the section above, in equilibrium $\boldsymbol{M}$ is described by $M_z = M_z^0$ and $M_x = M_y = 0$.
In analogy to Eq. 2.11 and by expanding Eq. 2.8 Felix Bloch described the relaxation of $\boldsymbol{M}$ with the so-called Bloch equations.

$$\frac{dM_z}{dt} = \frac{M_z^0 - M_z}{T_1} + \gamma_B \left(\boldsymbol{M} \times \boldsymbol{B}\right)_z \tag{2.12}$$

$$\frac{dM_x}{dt} = \gamma_B \left(\boldsymbol{M} \times \boldsymbol{B}\right)_x - \frac{M_x}{T_2} \tag{2.13}$$

$$\frac{dM_y}{dt} = \gamma_B \left(\boldsymbol{M} \times \boldsymbol{B}\right)_y - \frac{M_y}{T_2} \tag{2.14}$$

Here a second time constant T_2 is introduced for the description of the phase coherence loss of the microscopic magnetizations, that eliminates M_x and M_y. It is different from T_1 since the underlying mechanisms involve different interaction partners. T_1 describes changes in M_z, which correspond to a gain or loss of energy. Thus, these processes must include the participation of the resort and are called spin-lattice-interaction. An example for a spin-lattice-interaction can be the movement of a dipole-molecule emitting radiation which is absorbed, causing a flip of the spin state.
Mechanisms covered by T_2 do not change the energy of the spin-system. Consequently, the energy must be exchanged between spins in the system. These processes, are interpreted as intramolecular dipole-dipole interactions causing field fluctuations, which lead to a dephasing of the transverse nuclear magnetization [11].

These differences in relaxation behavior, due to the surrounding of the protons (in addition to the proton density itself), allow MRI to distinguish different tissue types, using imaging protocols with desired contrast weighting. To analyze the relaxation process it is necessary to actively distort ('to excite') the equilibrium state of the total magnetization $\boldsymbol{M}$.
Therefore, additionally to $\boldsymbol{B}_0 = B_0 \boldsymbol{e_{z'}}$ the time dependent external field

$$\boldsymbol{B_1}(t) = B_1 \left((\cos(\Delta\omega t)\boldsymbol{e_{x'}} + \sin(\Delta\omega t)\boldsymbol{e_{y'}}) \right) \tag{2.15}$$

is applied with $\Delta\omega = \omega_L - \omega$ within the coordinate system rotating with ω_L around the z-axis. This $\boldsymbol{B_1}$-field is part of an externally applied electromagnetic field called radio frequency (RF) pulse. For simplicity only time scales short enough to neglect relaxation effects are considered and the phase of $\boldsymbol{B_1}$ is defined so that $\boldsymbol{B_1}(t=0) = B_1 \boldsymbol{e_{x'}}$. Thus, $\boldsymbol{M}$ follows

$$\frac{dM_z}{dt} = \gamma_B B_1 \left(M_{x'} \sin(\Delta\omega t) - M_{y'} \cos(\Delta\omega t) \right) \tag{2.16}$$

$$\frac{dM_{x'}}{dt} = -\gamma_B M_z B_1 \sin(\Delta\omega t) \tag{2.17}$$

$$\frac{dM_{y'}}{dt} = \gamma_B M_z B_1 \cos(\Delta\omega t) \tag{2.18}$$

One can see, that, when $\boldsymbol{B_1}$ is in resonance (resonance condition: $\Delta\omega \to 0$) the terms containing sine disappear, while the cosine terms become constant. $\boldsymbol{M}$ then describes a continuous circular movement in the y'-z'-plane around $\boldsymbol{B_1}$ with constant angular velocity γB_1. For slightly off resonant frequencies the movement of $\boldsymbol{M}$ is more complex, as it also rotates around the y-axis. Regarding frequencies far off the resonance condition obviously leads to comparably small disturbances of $\boldsymbol{M}$ because of the self-compensation of the sine and cosine terms within one period of ω.
Thus, it is possible to tilt the total magnetization in the y'-z'-plane by any flip angle α with a resonant magnetic field $\boldsymbol{B_1}$. The angle is a function of the RF duration t_α and the $\boldsymbol{B_1}$ amplitude.

$$\alpha = -\gamma_B B_1 t_\alpha \tag{2.19}$$

Due to the typical MRI Larmor-Frequencies being in the range of MHz, such $\boldsymbol{B_1}$ fields are called Radio-Frequency (RF) pulses. The relaxation of $\boldsymbol{M}$ following the excitation

of an RF pulse can be measured as alternating field by the MRI system. The rotating transverse magnetization $\boldsymbol{M_{xy}}$ induces currents within the receive coils of the system. According to the decay of $\boldsymbol{M_{xy}}$ (compare Bloch equations 2.12 - 2.14) the currents show a decrescent temporal development, called free induction decay (FID).
Considering real MRI measurements, the FID is dominated by an additional effect, caused by local $\boldsymbol{B_0}$ inhomogeneities that are introduced by technical imperfections or susceptibility differences between tissues [9]. As a consequence, the measured $\boldsymbol{M}$ is a combination of spatial distributed local magnetizations that develop differently in time, as they possess different Larmor-Frequencies. Thus, the dephasing between magnetizations is amplified, resulting in a relaxation time constant $T_2^* < T_2$.

2.2 MRI data acquisition

Following the introduction of the FID and the interaction mechanisms taking place in MRI, this section covers the description of how topographic information is generated. With the basic example of so-called gradient echos the relationship between the spatial phase distribution $\Phi(\boldsymbol{r})$ of the magnetization and linear varying magnetic field gradients $\boldsymbol{G}(t)$ is introduced. The mutual dependency of these two quantities describes the connection of information acquired in time domain to information present in the spatial domain. Therefore the concept of the k-space will be introduced before the principles of the spatial encoding procedures are addressed.

2.2.1 Gradient echo sequences

In MRI many data acquisition techniques base on the concept of an effect called echo. The first description of echos was published by Erwin Hahn [12]. He discovered that after an initial RF pulse, a second one can restore the signal loss due to dephasing mechanisms that are constant in time and location. The signal is called 'spin echo'. Later he also investigated echos generated by an overlayed supplemental field gradient with alternating polarity [13]. This so-called 'gradient echo' occurs due to an active dephasing and refocusing effect of the gradient field during the FID. The maximum of this echo is reached at the echo time T_E after the initial RF pulse (usually with $\alpha \leq 90°$, see Eq. 2.19). The peak amplitude of the echo is set by the T_2^* decay (Fig. 2.2). These two types of echos span a variety of possible imaging methods in MRI. Since the

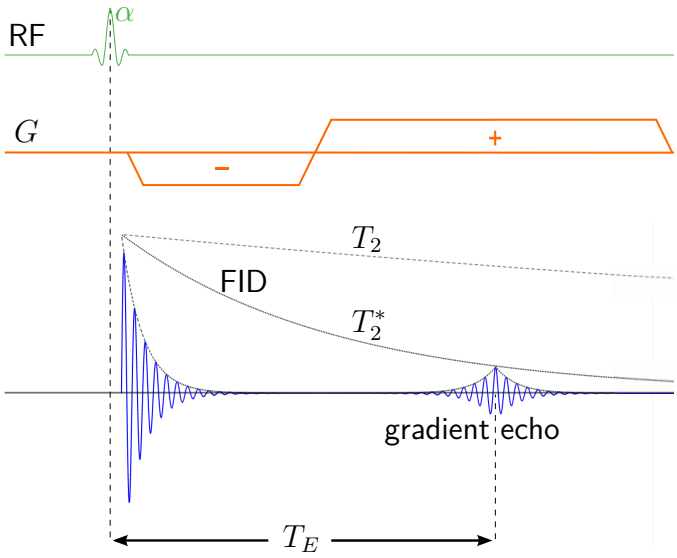

Figure 2.2 – Illustration of a gradient echo generated via a dephasing and a rephasing gradient after an RF excitation ($\alpha \leq 90°$). Note that the echo amplitude is given by the T_2^* decay.

main effects investigated later in this work are associated with a method based on the gradient echo, the further introduction is limited to this sequence type.

As already mentioned the gradient echo is achieved by an active signal dephasing and rebuilding by a magnetic field gradient $\boldsymbol{G}$, an additional spatial linear varying inhomogeneity to the z-component of the $\boldsymbol{B_0}$ field.

$$\boldsymbol{G}(t) = G_x \boldsymbol{e_x} + G_y \boldsymbol{e_y} + G_z \boldsymbol{e_z} = \frac{\partial B_z}{\partial x}(t)\boldsymbol{e_x} + \frac{\partial B_z}{\partial y}(t)\boldsymbol{e_y} + \frac{\partial B_z}{\partial z}(t)\boldsymbol{e_z} \tag{2.20}$$

The accumulated phase difference at the position $\boldsymbol{r}$, induced by $\boldsymbol{G}(t)$ since the time of the RF excitation t_0 is

$$\Phi_G(\boldsymbol{r}, t') = -\gamma_B \, \boldsymbol{r} \int_{t_0}^{t'} \boldsymbol{G}(t) dt \tag{2.21}$$

The peak amplitude of gradient echos appear when the zeroth gradient momentum vanishes [14].

$$\int_{t_0}^{t'} \boldsymbol{G}(t) dt = 0 \tag{2.22}$$

A simple example for generating a gradient echo for a given T_E is to use a constant

gradient amplitude G and changing the polarity of the gradient after $T_E/2$

$$\int_{t_0}^{T_E/2} \boldsymbol{G} dt + \int_{T_E/2}^{T_E} (-\boldsymbol{G})\, dt = \mathbf{0} \tag{2.23}$$

where t_0 is the starting time of the FID. This treatment does not consider the possible movement of particles in the gradient field. Moving particles would in general experience different absolute amplitudes of $\boldsymbol{G}$ during the first and second half of T_E as they change position in an inhomogeneous field, an effect that can be used to determine relative particle velocities of signal emitting structures [13] which is actually utilized for flow or diffusion quantification or to make an imaging sequence insensitive to flow, diffusion and motion.

2.2.2 k-space

MRI uses so-called frequency encoding (explained in the next section) to identify location, the frequency domain is therewith corresponding with the spatial domain. The MRI signal is, however, acquired over time. Transferring the time resolved signal into the frequency domain (respectively spatial domain in MRI) is generally known as Fourier transformation. For a distribution $P(\boldsymbol{r})$ in real-space the Fourier transform $K(\boldsymbol{k})$ to the so-called k-space is given as:

$$K(\boldsymbol{k}) = (2\pi)^{-3} \iiint\limits_{\text{real-space}} P(\boldsymbol{r})\exp(i\boldsymbol{k}\boldsymbol{r})\, dx\, dy\, dz \tag{2.24}$$

and its inverse

$$P(\boldsymbol{r}) = \iiint\limits_{\text{k-space}} K(\boldsymbol{k})\exp(-i\boldsymbol{k}\boldsymbol{r})\, dk_x\, dk_y\, dk_z \tag{2.25}$$

with the origin $\boldsymbol{r}=\mathbf{0}$ describing the spatial center of P. The equations state that each point of P can be expressed in complex exponential functions (basically spatial waves) weighted with $K(\boldsymbol{k})$. This means $P(\boldsymbol{r})$ is a combination of various spatial waves with different wave numbers $\boldsymbol{k}$. This implies that a point of P can be expressed as a combination of all points in the k-space and vice versa. In other words, one point in k-space contains information about all points in the spatial domain.

$\boldsymbol{k}$ characterizes the phase arrangement and $K(\boldsymbol{k})$ the amplitude of the spatial wave

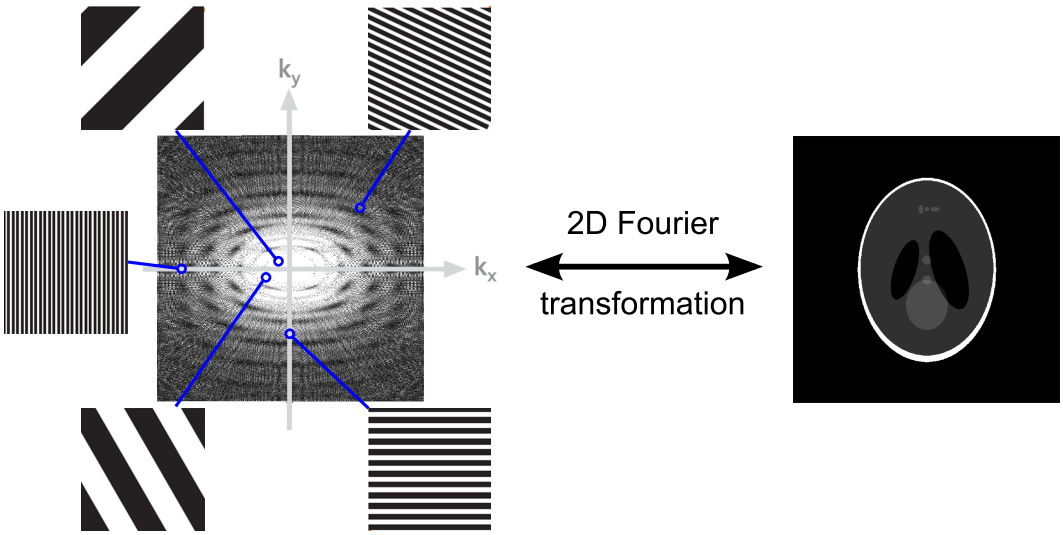

Figure 2.3 – A 2D example of the influence of a single k-space point on the real space image. On the left, a two dimensional k-space is shown. The points in k-space encode the phase arrangement (spatial waves) of the spins in real space, which is illustrated for some points. The right side illustrates the associated image (MATLAB Shepp-Logan phantom) in real space, a combination of all phase arrangements in k-space.

(see Fig. 2.3). Thus, the large $\boldsymbol{k}$ values far away from the center describe high frequency oscillating spatial waves and are responsible for coding sharp changes (contours) and small objects (image details) in the image domain. Whereas small $\boldsymbol{k}$ values close to the origin contain information about larger objects and general image contrast [15].

Note that $\boldsymbol{k}$ appears in the imaginary exponential function, hence $K(\boldsymbol{k})$ is periodic in each dimension.

2.2.3 Spatial encoding

The general mechanism of encoding and retrieving spatial information out of the electromagnetic signal response following an RF excitation will be the content of this section. An MRI sequence as described in Sec. 2.2.1 generates an echo, containing contributions from each volume element (voxel) of the investigated body meeting the resonance condition (Sec. 2.1.2). To reduce the responsive volume to a 2D slice, a linear magnetic

field gradient $\boldsymbol{G}_{\text{slice}}$ is utilized. When applied along the z-direction, $\boldsymbol{B_0}$ becomes

$$\boldsymbol{B}_{\boldsymbol{G},\mathbf{0}}(z) = z\, G_z(t)\boldsymbol{e_z} + \boldsymbol{B_0} \tag{2.26}$$

with $z, y, z = 0$ indicating the so-called 'isocenter' of the MRI system.

As a result of the generated magnetic field gradient, the resonance frequency becomes a function of location. Choosing a center frequency $\omega(z)$ as $-\gamma_B B_{G,0}(z)$ with a certain bandwidth excites a slice of a desired thickness around z within the field of view (with a few exceptions, the bandwidth of such a pulse usually remains constant while a change in gradient amplitude is used to control the thickness of the slice to be excited). Since the MRI system is capable of generating magnetic field gradients (superimposing on the B_0 amplitude) in all spatial dimensions, a slice selection with arbitrary orientation is achievable. Note that $\boldsymbol{G}_{\text{slice}}$ is only needed during RF pulse applications (compare Fig. 2.4).

The excited slice is subdivided in a regular grid of $N_x \times N_y$ voxels. The so-called 'spin density' $\rho(\boldsymbol{r})$ indicates how much excitable nuclear magnetization is present in each voxel. The transverse magnetization of each voxel generates a signal with phase $\Phi_G(\boldsymbol{r}, t')$. According to [14] the superposition of the signals $S(t')$ of the slice can be written as[2]

$$S(t') = \iiint \rho(\boldsymbol{r})\text{exp}(i\Phi_G(\boldsymbol{r}, t'))\, dx\, dy\, dz \tag{2.27}$$

As previously indicated, the amplitude of each point in k-space represents the contribution of a specific spatial frequency (intensity modulation across an image). Using Eq. 2.21, the spatial frequency $\boldsymbol{k}(t')$ can be expressed as a function of the applied magnetic field gradient $\boldsymbol{G}(t)$.

$$\begin{aligned} \boldsymbol{k}(t') &= \frac{\Phi_G(x,t')}{2\pi x}\boldsymbol{e_{k_x}} + \frac{\Phi_G(y,t')}{2\pi y}\boldsymbol{e_{k_y}} + \frac{\Phi_G(z,t')}{2\pi z}\boldsymbol{e_{k_z}} \\ &= -\frac{\gamma_B}{2\pi}\int_0^{t'} G_x(t)\boldsymbol{e_{k_x}} + G_y(t)\boldsymbol{e_{k_y}} + G_z(t)\boldsymbol{e_{k_z}} dt \end{aligned} \tag{2.28}$$

Combining Eqs. 2.27 and 2.28 yields

[2] For clarity relaxation effects (T_1, T_2) and other prefactors are neglected.

$$S\left(\boldsymbol{k}(t')\right) = \iiint \rho(\boldsymbol{r})\exp\left(i2\pi\boldsymbol{k}(t')\boldsymbol{r}\right)\, dx\, dy\, dz \tag{2.29}$$

In this equation the relation between k-space and MR signal becomes evident. The manipulation of the phase, by applying magnetic field gradients, allows to ascribed the sampled MR signal to points in k-space.

For example, when the peak amplitude of the echo signal after a gradient momentum $\boldsymbol{G}_{\text{Phase}}\, t_y = G_y t_y \boldsymbol{e}_{\boldsymbol{k_y}}$ is measured, the point in k-space ascribed to the measurement value is

$$\boldsymbol{k} = \frac{\gamma_B}{2\pi}\left(G_y \boldsymbol{e}_{\boldsymbol{k_y}} \cdot t_y + G_x \boldsymbol{e}_{\boldsymbol{k_y}} \cdot 0\right) \tag{2.30}$$

The signal is said to be 'phase encoded'. This encoding can be repeated for all necessary k-space points (defined by the desired image size and resolution; see Sec. 2.2.2) with adequate gradient activity combinations.

Encoding several k-space points with only one echo is called 'frequency encoding'. This technique samples the echo signal during the application of the refocusing gradient. The gradient linearly varies the Larmor frequencies within the imaged slice along the gradient direction. Consequently, the position (in gradient direction) of a nuclear magnetization can be associated with the emitted signal frequency. Consider a gradient echo with a refocusing gradient of the form $\boldsymbol{G}_{\text{read}} = G_x \boldsymbol{e}_{\boldsymbol{x}}$ (read-out). After a defocusing gradient pulse of $-G_x$ for $T_E/2$ equation 2.30 expands to

$$\boldsymbol{k}(t') = \frac{\gamma_B}{2\pi}(\overbrace{G_y t_y \boldsymbol{e}_{\boldsymbol{k_y}} - \frac{1}{2} G_x T_E \boldsymbol{e}_{\boldsymbol{k_x}}}^{\boldsymbol{k_0}} + G_x t \boldsymbol{e}_{\boldsymbol{k_x}}) \tag{2.31}$$

and describes a 'movement' $\frac{\partial \boldsymbol{k}}{\partial t} = G_x \boldsymbol{e}_{\boldsymbol{k_x}}$ through k-space along the k_x-axis, starting at a point $\boldsymbol{k_0}$. Thus, sampling the echo at equidistant time points is equivalent to measuring the values of $\boldsymbol{k}$ along a line. Repeating this approach with different values of G_y allows the coverage of the full k-space and is a basic example for a gradient echo imaging sequence (see Fig. 2.4).

The magnetic field gradient applied during the time of slice selection causes a phase dispersion based on the different frequencies and the duration of the slice selection

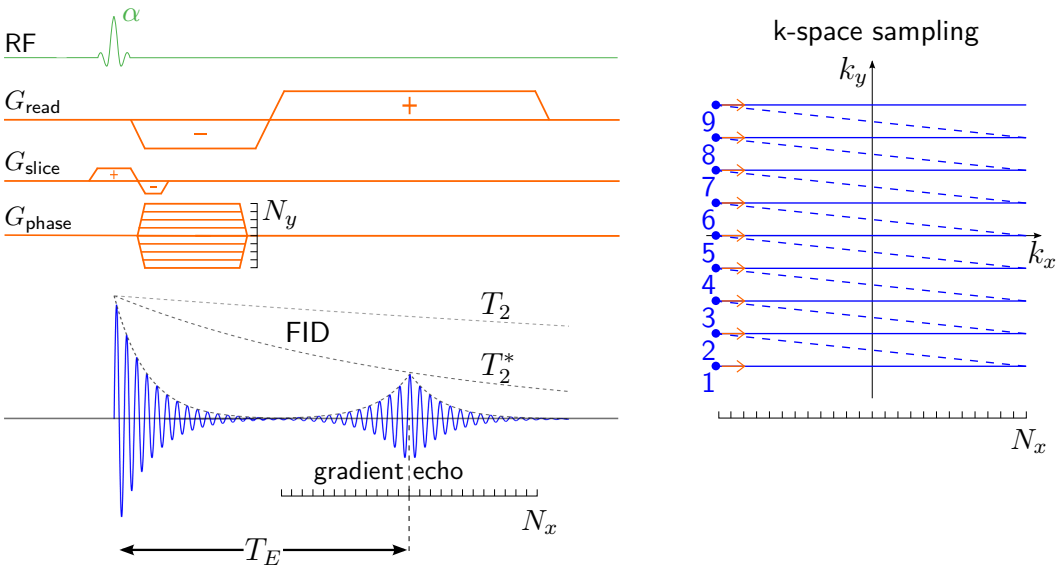

Figure 2.4 – Example for a basic gradient echo sequence for an image with N_y phase encoding steps and N_x sampling points during the frequency encoding gradient. One k-space line per sequence repetition is acquired with varying phase encoding amplitude, as indicated for $\boldsymbol{G}_{\text{phase}}$. The amplitude depends on the desired initial phase of the magnetization, setting the position in k-space where the echo sampling should begin. On the right the corresponding Cartesian sampling pattern is illustrated. The numbered points represent the read-out start for different $\boldsymbol{G}_{\text{phase}}$.

gradient. Hence, a compensating gradient pulse following the excitation is used to reverse that dispersion [16]. Where appropriate it can alternatively be played out after an RF refocusing pulse. Using a gradient with the amplitude $-G_{\text{slice}}$, the necessary time for the rephasing is approximately the time from the RF peak to the end of the RF excitation [17].

The majority of currently used k-space sampling strategies are called Cartesian sampling, using a rectangular sampling grid, with equidistant sampling points during data acquisition [18, 19]. As described in the above example, for each evenly distributed amplitude (integral) of phase-encoding gradient, a k-space line in frequency-encoding direction is sampled, giving parallel and equidistant sampling trajectories through k-space [17]. On the left side in figure 2.4 a sequence applicable for Cartesian sampling, using one FID per phase-encoding value is shown. The 'grid' in $\boldsymbol{G}_{\text{phase}}$ visualizes the

different amplitudes needed for the equidistant line by line stepping through the k-space .

The investigation of magnetomechanical effects is limited to an MRI Sequence using a Cartesian sampling scheme in this work. Alternative sampling methods (e.g. spiral or radial trajectories in k-space) are not covered. The focus lies on an MRI sequence called 'blipped' Echo-Planar-Imaging (EPI). It applies a periodically alternating read-out gradient in combination with short phase-encoding gradient pulses ('blips') to achieve fast cartesian sampling. A more detailed explanation is given in the next section.

2.2.4 Echo-planar-imaging & ghosting artifacts

EPI, first described by Mansfield [20], acquires the whole k-space utilizing multiple phase encoded echoes, following a single RF-excitation (single shot sequence). As the signal decays with T_2^*, the data acquisition window has to be kept short. [21] states an estimate total time window of $50\,\text{ms}$ to $100\,\text{ms}$ available for data acquisition.

One possible EPI acquisition scheme to achieve this short sampling is called blipped EPI and is illustrated in figure 2.5. Typically an alternating read-out gradient of trapezoidal shape (sampling along a k-space line) with frequency ω_{EPI} is accompanied by small phase-encoding 'blips' (stepping line by line) at the zero-crossing of the read-out gradient. Such a sampling pattern results in a meandering k-space trajectory. The oscillating read out gradient generates an echo train with a regular temporal distance $T_{E_{\text{EPI}}} = \frac{\pi}{\omega_{\text{EPI}}}$ between the echos. Each of these echos possesses a different amplitude due to the T_2^* decay, resulting in an asymmetric k-space data set.
In order to minimize the violation of k-space symmetry, the echo train should be as short as possible. This is achieved by using high imaging bandwidths causing short data acquisition windows (Fourier relationship). A drawback of fast imaging, utilizing a high imaging bandwidth, is the reduced filtering of noise. The imaged object is emitting electromagnetic noise in a wide frequency range while exposed to a strong magnetic field. A higher receive bandwidth acquires more noise superimposing on the imaging signal.
A reduced number of Fourier lines can be utilized to reduce the needed imaging time, which in turn limits the spatial resolution in the direction of phase encoding. Due to the noise limitation with high imaging bandwidth, the number of Fourier lines (and

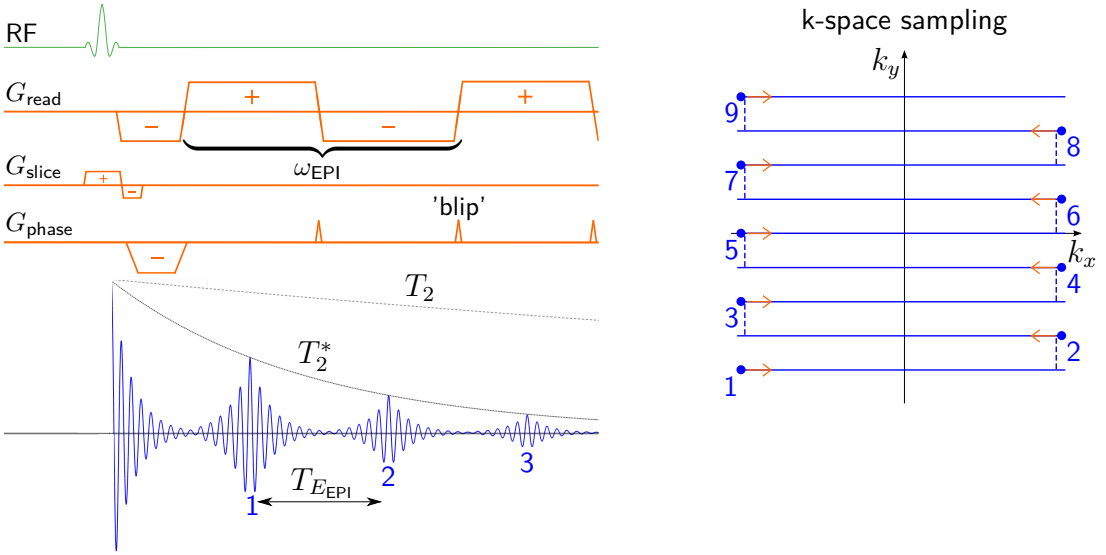

Figure 2.5 – Illustration of an EPI sequence with the according k-space sampling scheme. The alternating read-out gradient periodically generates echos with $T_{E_{\text{EPI}}} = \pi/\omega_{\text{EPI}}$ spacing. In between of the echos phase encoding blips cause a line wise stepping through the k-space. Only the first three lines of the sampling scheme are shown.

respectively echos) is typically not larger than 128 for single shot sequences [22]. An estimate of the upper limit of gradient switching frequency for EPI is roughly $1300\,\text{Hz}$, resulting from an acquisition of 128 echos in $50\,\text{ms}$.

With the short time span necessary for running a single-shot sequence, EPI offers the potential to visualize physical processes within the imaged body. It allows, for example, time-resolved imaging of the beating heart throughout a cardiac cycle or monitoring the diffusion of body liquids. MRI is the only imaging modality capable of imaging tissue specific diffusion and this information is utilized e.g. in imaging of the brain, not only following a suspected stroke, but also for the differential diagnosis of different mass lesions. Echo planar imaging is needed for diffusion measurements in order to overcome the sensitivity to bulk motions, such as cardiac-cycle-related pulsations [23]. Therefore, EPI is of high importance in functional imaging and especially neuroradiology.

At first, 1956 diffusion has been considered a potential source for a systematic error in

measuring T_2 relaxation times [24]. Denis Le Bihan introduced the concept of diffusion to imaging in 1986 [25].

As mentioned above, EPI is T_2^*-sensitive and therewith signal voids are to be expected for voxels exposed to patient or system related susceptibility gradients, which locally modify the Larmor frequency. Whereas a high bandwidth is used in frequency encoding direction, the blipped phase encoding gradient allows a low bandwidth, filtering those modified frequencies in that direction. Therewith a strong sensitivity to susceptibility gradients is introduced, possibly resulting in image distortions.
For more detailed discussions on general properties, advantages and problems in EPI and further information concerning different variants, it is referred to numerous textbooks e.g. [14, 17].

2.2.5 N/2-Ghosting in echo-planar imaging

This section will focus on the so-called 'N/2-Ghosting', a prominent artifact in EPI. Figure 2.6 illustrates the principal appearance of N/2-Ghosting. The left image is undisturbed by artifacts, while the right image shows N/2-Ghosting. Additional copies (ghosts) of the original object are visible. The N/2-Ghosts are shifted by half of the image size, which are N/2 voxels for a typical N×N image matrix. Any periodic disturbance within k-space results in ghost artifacts within the image. For N/2-Ghosting the disturbance possesses a time dependency, so that it is sampled every other k-space line. An exemplary effect of such a disturbance on the signal S (see Eq. 2.29) is analytically described in the following. For this example the disturbance is defined as a modification of the k-space in k_y direction. In k_x-direction no disturbance occurs, allowing a reduction of the problem to one dimension.

$$S(y) = \int S(k_y)\mathrm{exp}(-ik_y y)\, dk_y \tag{2.32}$$

Discretizing the integral to a sum yields

$$S(y) = \sum_{n_y=-N_y/2}^{N_y/2} \overbrace{S(k_y)\mathrm{exp}(-in_y \Delta k_y y)}^{S'} \tag{2.33}$$

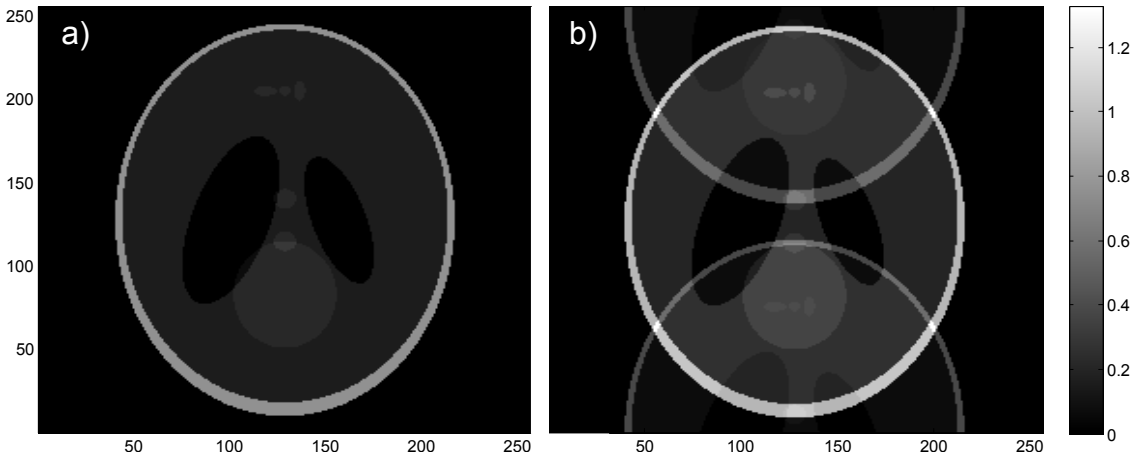

Figure 2.6 – a) Original image. - b) Image with ghosting artifacts generated by an amplitude modulation within the k-space of a) as described in Eq. 2.34. The modulation amplitude a was arbitrarily set to 0.2 to generate a distinct observable ghosting artifact.

with the discretization $\Delta k_y = \frac{\pi}{y_{\text{max}}}$ in k-space, where y_{max} indicates the maximal distance from the origin of the image in real space (half the image size in that direction).
A signal amplitude modulation of $\pm a$ for every even or odd k-space line can be expressed as

$$S_a(y) = \sum_{n_y=-N_y/2}^{N_y/2} S' \cdot (1 + a\cos(\pi n_y)) \tag{2.34}$$

Considering $\cos(\pi n_y) = \frac{1}{2}\left(\exp(i\pi n_y) + \exp(-i\pi n_y)\right)$ yields

$$\begin{aligned} S_a(y) &= \sum_{n_y=-N_y/2}^{N_y/2} S' \cdot \left(1 + \frac{a}{2}(\exp(i\pi n_y \cdot \Delta k_y/\Delta k_y) + \exp(-i\pi n_y \cdot \Delta k_y/\Delta k_y))\right) \\ &= \sum_{n_y=-N_y/2}^{N_y/2} S' \cdot \left(1 + \frac{a}{2}(\exp(in_y \Delta k_y y_{\text{max}}) + \exp(-in_y \cdot \Delta k_y y_{\text{max}}))\right) \\ &= s(y) + \frac{a}{2}\left(S(y + y_{\text{max}}) + S(y - y_{\text{max}})\right) \end{aligned} \tag{2.35}$$

This states that additionally to the original image the given modulation would generate two ghosts of $\frac{a}{2}$ times the amplitude of the original signal. The ghosts would thereby be shifted in space by $\pm y_{\text{max}}$ and would overlap constructively, which could easily be transferred into a mutual cancellation by adding a $180°$ phase-shift to the modulation. A demonstrative image, created via the described mathematics is shown in figure 2.6

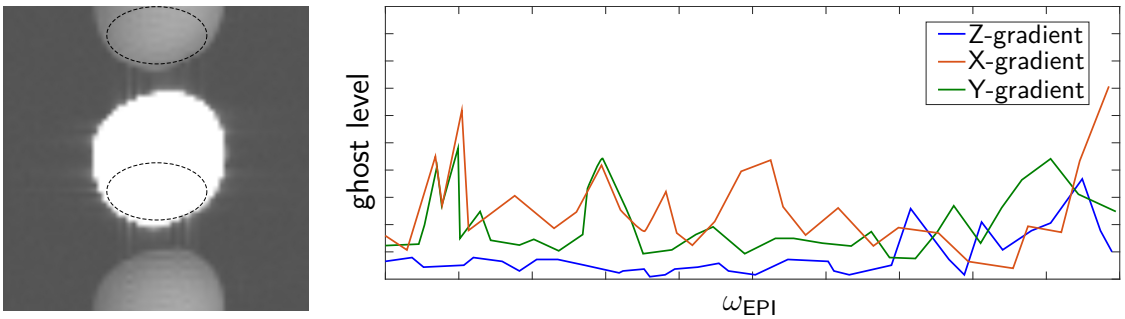

Figure 2.7 – Left) An exemplary EPI image with strong windowing showing a spherical phantom and a N/2-Ghosting artifact. The dashed ellipses indicate the areas in which the average signal values for the calculation of the ghost level were evaluated. Right) Drawing of typical ghosting spectra for the three orthogonal gradient axes. It shows how strongly the switching frequency ω_{EPI} of the read-out gradient influences the appearance of N/2-Ghosting artifacts.

for an artificial image with a being arbitrarily set to 0.2. It is obvious that the overlap of the ghosting artifact with the original image can cover important information for diagnostics. Thus, minimizing or preventing ghosting is fundamental for reliable EPI measurements.

Potential disturbances leading to such periodic signal modulations can be caused by oscillating eddy currents. A goal of the presented work is to demonstrate the connection of ghosting relevant oscillating currents to mechanical vibrations of the cryostat surrounding the magnet. Locating where and determining how these eddy currents are excited, as well as the resulting effects on imaging are investigated.

EPI measurements show a strong dependency on the frequency ω_{EPI} used for the read-out gradient. The operation of the gradient coils emits radiation with a certain frequency spectrum (discussed in more detail in Sec. 3.1.1), which is proposed to excite oscillating eddy currents via the magnetomachanical interactions. A possible method to demonstrate the read-out frequency dependency of ghosting is to evaluate the so-called 'ghost level' in images of a homogeneous spherical MRI phantom for different ω_{EPI}. Therefore the average signal value for an image region covered by the ghosting artifact is calculated and set in relation to the average value measured in an image region of the phantom itself. For all frequencies both average values are computed over the same respective image region. A possible choice for the two regions is indicated

(dashed ellipses) in the left picture of figure 2.7. It shows an EPI image of a spherical phantom for one read-out gradient frequency, which generates a ghosting artifact. The plot on the right gives an example of the frequency dependency of the ghost level. For each graph another gradient axes was used as read-out gradient.

While the X- and Y-gradients show several resonant peaks within the investigated frequency range, the Z-gradient basically remains on the background noise level. For higher frequencies Z becomes more relevant. Strong ghosting is also possible at the mechanical resonances of the GC. But these resonances are well known and not all EPI frequencies showing ghosting correlate with these resonances. Combined with the fact, that electromagnetic field decays with the distance, the cryostat is most likely the origin of field disturbances, which lead to ghosting. These disturbing fields are assumed to be a consequence of eddy currents induced by mechanical resonances of the cryostat. The number of according structural modes in the relevant frequency range (mode density) is very high so that guessing the resonant modes responsible for the ghosting is not possible. Measuring the vibrations of a cooled down cryostat, containing vacuum and with active $\boldsymbol{B_0}$ is also hard to realize, especially when it is unclear where to measure exactly. Thus, the FE-analysis is the method of choice to investigate the phenomenon.

2.3 MRI hardware

The hardware components of current MRI systems range from computer processors, over water pumps, RF and acoustic isolation to the movable patient table, electric amplifiers and ventilation systems. This section will focus on the hardware relevant for the magnetomechanical interactions investigated in this work, the main magnet, its cryogenic housing and the gradient coil (GC).

As mentioned in section 2.1.1 a high magnetic field is necessary to generate a sufficiently strong MR signal. The majority of MRI systems utilizes cylindrical superconductive magnet coils. Besides its primary task to achieve a homogenous field in the imaging volume also called field of view (FOV), the magnet design shall exhibit a fast decaying field distribution in the surrounding of the MRI system. The so-called 'fringe field' of the static magnetic field should be confined (also for installation requirements) to the

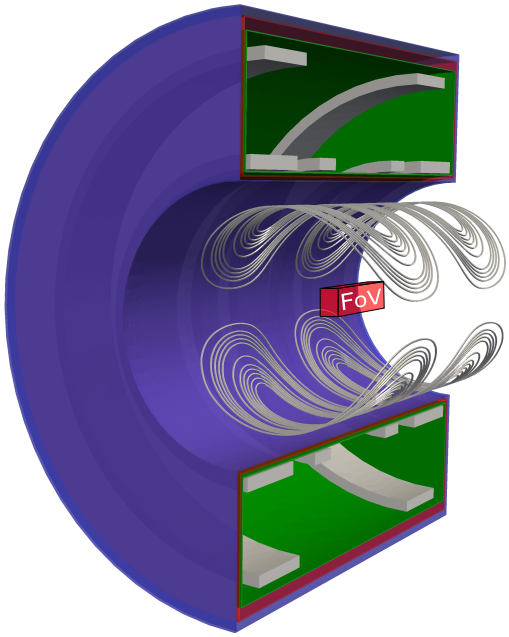

Figure 2.8 – Cut-out drawing of the relevant magnetomechanical components of the MRI system. The helium vessel (green) encloses the superconductive coils and is itself surrounded by the cryoshield (red) and the outer vacuum chamber (blue). The gray saddle like patterns around the field of view (FoV) depicts the wire pattern of a Y-gradient coil.

examination room as close as possible. This can be achieved either through passive shielding (iron in the floor, walls and ceiling) or through active shielding. The latter is used in the majority of current MRI systems. A field strength of $0.5\,\mathrm{mT}$ (historically referred to as 'five gauss', according to the centimeter-gram-second system of units) and below are considered 'safe' levels of static magnetic field exposure for the general public [26]. The five gauss line has to be indicated and should not extend into the patient waiting area. With the active shielding coils the fringe field decay behavior increases from linear to quadratic over the distance.

To maintain their superconductive state the magnet coils need to be kept at temperatures of only a few degrees Kelvin. Current superconductive magnets require the placement of the superconductive coils in a bath of liquid helium. A cryocooler system provides a zero boil-off of the helium. To minimize the necessary cooling power, the magnet coils and helium are encapsulated in a cryostat.

The cryostat consists of several metallic vessels. Magnets, considered in this work, only used three vessels (so-called 'shields'), thus the simulations and the following text have been restricted to describing a three shields setup as well. The shields of the cryostat are thermally isolated by vacuum against each other and each one forms a hollow cylinder consisting of an inner and outer bore, as well as 'shield ends' connecting the bores. The inner vessel is in direct contact with the helium and is therefore called Helium-Vessel (HeV). The outer vessel, containing the vacuum, is named Outer Vacuum Chamber (OVC). Between OVC and HeV the so-called cryogenic shield (CS) is located. It increases the cryogenic shielding of the magnet by additional absorption and partially reflection of heat radiation (compare Fig. 2.8). For expanding this functionality to electromagnetic radiation in general, the materials of the cryoshields are more conductive (electric and thermal) than the materials of the other vessels. The CS usually consists of aluminium, while the OVC and the HeV are typically made of stainless steel. The electric conductivity is shielding the superconductors against external electromagnetic fields and the thermal conductivity distributes potential heat loads, avoiding hot spots.

External electromagnetic fields transmitting to the magnet coils originate mainly from the gradient coil of the MRI system. The necessity of the gradient fields has been discussed in section 2.2. The gradient coil is located within the inner bore tube of the OVC and, like the cryostat, roughly has the form of a hollow cylinder. The coil is subdivided into coil pairs generating the magnetic field gradients in the three spatial dimensions. Along the z-direction the gradient is realized via two axial symmetric coils, while the X- and Y-gradients are produced by two so-called 'saddle coil' pairs each (see Fig. 2.8 and Fig. 3.17). The gradient coils, which were subject to this work, were all potted in glass-fiber reinforced composite material to suppress movement of the different coil parts during operation.

Besides several demands concerning the capabilities of the gradient coil, like low inductance and high gradient linearity, it is necessary, that the generated fields do not deposit too much energy (heat) within the cryostat shields via eddy currents. For this reason current gradient coils are actively shielded, meaning each gradient coil pair consists of two layers: The primary layer and a second layer at larger radius with opposite current

direction. Thereby the layers are designed in a way to maintain the demanded properties concerning the performance and accuracy of the magnetic field gradient within the FOV, while minimizing the stray field penetrating the cryostat.

2.4 Field transport within the cryostat due to magnetomechanic interactions

In section 2.3 the MRI components relevant for the investigated phenomena have been introduced. A rough outline of the expected interactions of these components shall be given in the following.

The starting point of the effects to be described is the gradient coil. When it is driven with a time dependent current it is generating dynamic electromagnetic fields. The spatial shape of the field distribution is determined by the wire pattern of the gradient coil. This distribution propagates mostly unaffected through the non-conductive gradient coil potting and air gaps before it encounters the conductive OVC. As stated by Faraday's law, the electromagnetic fields induce eddy currents within the OVC (see Fig. 2.9 a). According to Lenz's rule the direction of these eddy currents is oriented in such way, that the penetrating magnetic flux is compensated as far as possible. This has implications on the gradient fields within the FOV, as the eddy currents also emit fields towards the center of the MRI system. Thereby parts of the actual applied gradient fields in the FOV are temporarily canceled as long as the eddy currents are present.
Due to the limited conductivity and thickness of the OVC, parts of the magnetic field hitting the OVC are transmitted and can not be absorbed. A further effect influencing the absorption of radiation is the frequency dependent skin effect. An increasing frequency of the GC fields reduces the penetration depth of these fields and the according eddy currents. Within the frequency range of interest and for realistic material parameters, there are always parts of the field transcending the OVC.

These transcending fields as well as the unattenuated radiation are from now on named primary radiation or respectively primary fields. Eddy currents resulting from these primary fields are consequently called primary eddy currents.

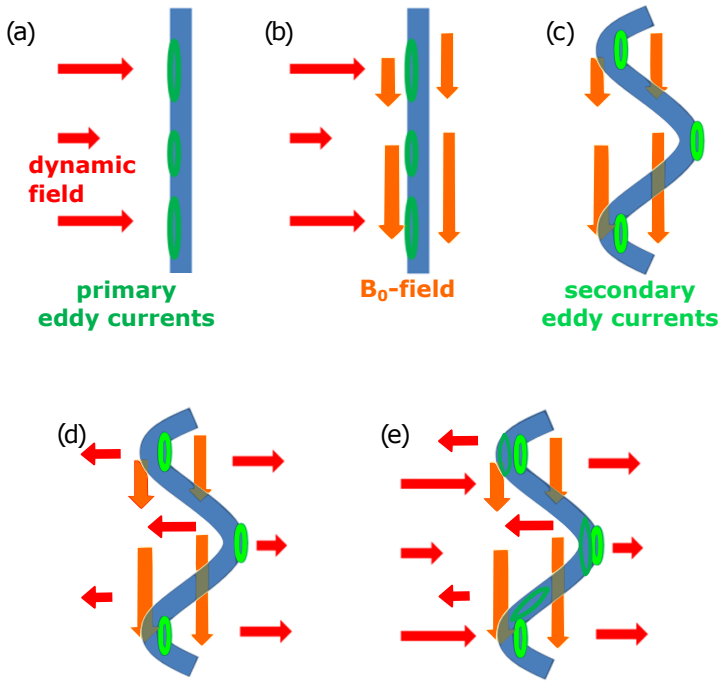

Figure 2.9 – Illustration of the influence of a conductive layer on the field transport. (a) Initially, dynamic electromagnetic fields generate primary eddy currents on the layer. (b) The primary Eddy currents interact dominantly with the present $\boldsymbol{B_0}$ field, generating Lorentz forces. (c) The Lorentz forces induce secondary eddy currents, as they move the conductive layer within the $\boldsymbol{B_0}$ field. (d) Additional fields are emitted by the secondary eddy currents. (e) A combined illustration of the previous images, indicating that the described processes are taking place simultaneously. For clarity fields transcending the layer without absorption and fields emitted by the primary eddy currents are not illustrated.

On top of these primary fields and currents occur secondary contributions via the magnetomechanical coupling. Source of the coupling is the interaction of the primary eddy currents with the present magnetic fields, which are dominated by the $\boldsymbol{B_0}$ field of the main magnet coils. These interaction causes Lorentz forces on the OVC, which translate into movement (see Fig. 2.9 b-c). The displacement resulting from this movement is influenced by various factors. First, the amplitude and spatial distribution of the exciting force, as it drives the shield movement. Then, the properties of the OVC come into account, like density, stiffness, shape and damping. Additionally, again a frequency dependency occurs due to the mechanical resonance behavior of the OVC. Resonances occur if the exciting force distribution suits to

eigenmode shapes of the body. Excessive displacements are caused by a relatively small excitation force, if it is applied with an eigenfrequency of the according eigenmode.

Since the $\boldsymbol{B_0}$ field is not homogenous away from the FOV, secondary eddy currents are induced within moving conductive components. In addition, the movement of the shield is tilting its surfaces in relation to the magnetic field orientation. Related to the amplitude and velocity of the displacement the magnetic flux through the layer changes, causing eddy currents. Lenz's law states that these eddy currents generate 'secondary' Lorentz forces that counteract on the displacements to minimize the change of the magnetic flux. Thus, their amplitudes and spatial distributions (of secondary eddy currents and respectively forces) are dependent on the excited shape of the motion and the distribution of the magnetic field strength. Consequently, the distribution of primary and secondary eddy currents can be very different. While the positions of the primary eddy currents are defined by the GC stray field distribution, the position of the secondary eddy currents are dependent on the excited structural eigenmodes and therewith on frequency.

This is important as the secondary eddy currents do not only generate forces, which in principle simply damp the movement, but also emit magnetic fields (called secondary fields). These show a different distribution than the primary fields and also spread in both directions, towards the main magnet coils as well as towards the field of view. One has to consider a superposition of primary and secondary fields for the further transport mechanism in the cryostat (additional interactions with CS and HeV) and for the possible disturbances in the imaging volume (see Fig. 2.9 d).

All effects described not only take place on the OVC but occur similarly on the other shields. Yet, it has to be considered, that the initial excitation is a combination of primary and secondary fields. Finally, it must also be taken into account, that fields emitted by CS and HeV going towards the magnet center also influence the characteristics of the effects happening on the OVC (and CS). As a consequence the movement of the shields is mutually coupled via the magnetomechanical interactions, leading to a complex, non linear behavior of the system.

2.5 Mathematical description

The mathematical description of the magnetomechanic coupling can be specified by as set of coupled partial differential equations. In this section the basic equations, introducing coupling terms, will briefly be derived before the outlines of the numerical solution algorithms are presented.

Detailed mathematical derivations of the fundamentals of FE simulations are well scripted in several textbooks like [27–31]. Since the focus of this work is set on the investigation of magnetomechanical interactions, the text will concentrate on giving a short introduction to the corresponding equations. If not stated differently the formulations follow [30].

2.5.1 Mechanical field equations

Fundamental for the mathematical description of the magnetomechanic formulation are magnetic and mechanical equations. The structural part, vibrations of the cryostat excited by the external force density $\boldsymbol{f}_{\text{ext}}$, is addressed with Navier's equation of motion.

$$\rho_m \ddot{\boldsymbol{u}} = \boldsymbol{f}_{\text{ext}} + \hat{\boldsymbol{\mathcal{B}}}^{\mathsf{T}} \hat{\boldsymbol{\sigma}} \tag{2.36}$$

Here the density of the material is denoted as ρ_m and the displacement of the described body as $\boldsymbol{u}$. The mechanical stress tensor $\hat{\boldsymbol{\sigma}}$ is symmetric and can be written using Voigt notation [32] as a vector of six components.

$$\hat{\boldsymbol{\sigma}} = \begin{bmatrix} \sigma_{xx} & \sigma_{xy} & \sigma_{xz} \\ \sigma_{yx} & \sigma_{yy} & \sigma_{yz} \\ \sigma_{zx} & \sigma_{zy} & \sigma_{zz} \end{bmatrix} \rightarrow \boldsymbol{\sigma} = \begin{pmatrix} \sigma_{xx} \\ \sigma_{yy} \\ \sigma_{zz} \\ \sigma_{yz} \\ \sigma_{xz} \\ \sigma_{xy} \end{pmatrix} \tag{2.37}$$

With this notation the differential operator $\hat{\boldsymbol{\mathcal{B}}}$ reads as

$$\hat{\boldsymbol{\mathcal{B}}} = \begin{pmatrix} \frac{\partial}{\partial x} & 0 & 0 & 0 & \frac{\partial}{\partial z} & \frac{\partial}{\partial y} \\ 0 & \frac{\partial}{\partial y} & 0 & \frac{\partial}{\partial z} & 0 & \frac{\partial}{\partial x} \\ 0 & 0 & \frac{\partial}{\partial z} & \frac{\partial}{\partial y} & \frac{\partial}{\partial x} & 0 \end{pmatrix}^{\mathsf{T}} \tag{2.38}$$

For small displacements the mechanical stress $\hat{\boldsymbol{\sigma}}$ and strain $\hat{\boldsymbol{S}}$ can be treated in a linear relation, which allows a conversion via the tensor of elasticity moduli $\hat{\boldsymbol{c}}$ (for further details see [30, pg. 56-61])

$$\hat{\boldsymbol{\sigma}} = \hat{\boldsymbol{c}}\hat{\boldsymbol{S}} \tag{2.39}$$

Combined with 2.36 and describing $\hat{\boldsymbol{S}} \rightarrow \boldsymbol{S}$ using Voigt notation by $\hat{\boldsymbol{\mathcal{B}}}\boldsymbol{u}$ this yields the following equation of motion.

$$\rho_m \ddot{\boldsymbol{u}} = \boldsymbol{f}_{\mathsf{ext}} + \hat{\boldsymbol{\mathcal{B}}}^{\mathsf{T}} \hat{\boldsymbol{c}} \hat{\boldsymbol{\mathcal{B}}} \boldsymbol{u} \tag{2.40}$$

For the movement of the cryostat vessels also a velocity proportional damping term $\hat{\boldsymbol{R}}$, typically describing friction within the material, is considered.

$$\rho_m \ddot{\boldsymbol{u}} = \boldsymbol{f}_{\mathsf{ext}} + \hat{\boldsymbol{\mathcal{B}}}^{\mathsf{T}} \hat{\boldsymbol{c}} \hat{\boldsymbol{\mathcal{B}}} \boldsymbol{u} - \boldsymbol{R}\dot{\boldsymbol{u}} \tag{2.41}$$

This is an often used approximation in linear structural FE formalisms, assuming a viscoelastic damping. Finding suitable parameters for the correct description of the damping behavior is complex, especially in the low temperature regime needed for the characterization of the MRI cryostat. An evaluation of the accuracy and relevance of this damping description is covered in section 3.1.5.

2.5.2 Magnetic field equations

For the magnetic part Maxwell equations are used:

$$\nabla \cdot \boldsymbol{B} = 0 \tag{2.42}$$

$$\nabla \cdot \boldsymbol{E} = 0 \tag{2.43}$$

$$\nabla \times \boldsymbol{E} = -\frac{\partial}{\partial t}\boldsymbol{B} \tag{2.44}$$

$$\nabla \times \nu \boldsymbol{B} = \boldsymbol{J} \tag{2.45}$$

Here $\boldsymbol{E}$, $\boldsymbol{J}$ and ν denote the electric field, the current density and the magnetic reluctivity. Since the investigated phenomena only aim at pure eddy current problems, $\boldsymbol{E}$ is represented by a solenoidal vector field (Eq. 2.43) and displacement currents can be neglected. From equation 2.44 directly follows

$$\begin{aligned} \nabla \times (\boldsymbol{E} + \frac{\partial}{\partial t}\boldsymbol{A}) &= 0 \\ \Rightarrow \ \frac{\partial}{\partial t}\boldsymbol{A} &= -\boldsymbol{E} \end{aligned} \tag{2.46}$$

with the magnetic vector potential $\boldsymbol{A}$ defined by $\boldsymbol{B} = \nabla \times \boldsymbol{A}$ and gauged using the Coulomb gauge [33].

$$\nabla \cdot \boldsymbol{A} = 0 \tag{2.47}$$

2.5.3 Magnetomechanical Coupling

The Lorentz force density $\boldsymbol{f_L}$ acts as a coupling quantity in the numerical description of the magnetomechanical interaction. It has to be considered as exciting force $\boldsymbol{f}_{\text{ext}}$ in the mechanical field equation 2.41 and is calculated by 'magnetic' quantities as

$$\boldsymbol{f_L} = \boldsymbol{J} \times \boldsymbol{B} = (\boldsymbol{J_i} + \boldsymbol{J_e} + \boldsymbol{J}_{\text{emf}}) \times \boldsymbol{B} \tag{2.48}$$

Here $\boldsymbol{J_i}$ denotes the impressed current density generated by possible electric potential differences, $\boldsymbol{J_e} = \gamma \dot{\boldsymbol{A}}$ the eddy currents produced by the varying magnetic field (Eq. 2.46) and $\boldsymbol{J}_{\text{emf}}$ the so-called electromotive force (emf) term. The latter induces eddy currents within moving conductive parts (with the electrical conductivity γ) due to the movement of intrinsic charged particles in magnetic fields.

$$\boldsymbol{J}_{\text{emf}} = \gamma \dot{\boldsymbol{u}} \times \boldsymbol{B} \tag{2.49}$$

Considering the additional emf term (Eq. 2.49) in Ampère's circuital law (Eq. 2.45) combined with Faraday's law of induction (Eq. 2.44) yields

$$\nabla \times \nu \ \nabla \times \boldsymbol{A} = \boldsymbol{J_i} - \gamma \frac{\partial}{\partial t}\boldsymbol{A} + \gamma \dot{\boldsymbol{u}} \times \nabla \times \boldsymbol{A} \tag{2.50}$$

Within this expression one can directly see the coupling of the magnetic equations to the mechanical regime by the inclusion of the 'mechanical' velocity $\dot{\boldsymbol{u}}$, whereas current density $\boldsymbol{J}$ and magnetic flux $\boldsymbol{B}$ appear in the equation of motion 2.41.

$$\rho_m \ddot{\boldsymbol{u}} + \boldsymbol{R}\dot{\boldsymbol{u}} - \hat{\boldsymbol{\mathcal{B}}}^{\mathsf{T}} \hat{\boldsymbol{c}} \hat{\boldsymbol{\mathcal{B}}} \boldsymbol{u} = \boldsymbol{J} \times \boldsymbol{B} \tag{2.51}$$

2.6 Finite element simulations

A well established tool for the numerical solution of partial differential equations within arbitrarily shaped volumes is the finite element method. As indicated by the name the basic idea of this calculation scheme is the subdivision of the underlying volume into several small parts called elements. Using specific interpolation or 'ansatz' functions (typically polynomial) within these elements, an approximate solution can be computed within the element. The overall solution for the complete domain can finally be expressed as a combination of the local, elemental solutions. As a consequence, the accuracy of such an approximation will be dependent on the quality of the subdivision (mesh) in combination with the degree of the utilized ansatz functions. The tradeoff for increased accuracy by refining the mesh or increasing the degree of the ansatz functions is an enhanced demand of computational resources and solving time.

With the fast progress in computer technology the possibilities of the FE method have equally been pushed forward. Thus, applications with larger and more complex problems have become feasible. Additionally, the costs for applying FE simulations are more and more reduced so that the field of application is steadily growing. One of these rather new applications is the simulation of magnetomechanical interactions, meaning the calculation of magnetic and mechanical processes in the same model simultaneously, while taking the mutual interactions into account. Such coupled systems demand additional computational resources as well as advanced algorithmic approaches. In the following section the mathematical description of the physical processes is elaborated while the sections 2.6.2 and 2.6.3 will explain the FE algorithms in more detail. The presented calculation schemes are then applied for virtually reproducing the magnetomechanical interactions within the cryostat of an MRI system.

2.6.1 Biôt-Savart currents

For the underlying problem the most complex structures to model with the FE-mesh are the X- and Y-gradient coils. The cross-sectional dimensions of the conductors are of a few millimeters and consequently the mesh has to represent this in its spatial resolution around the conductors. Additionally, the winding pattern is complex, so that regular and uniform meshes for the surrounding volume are not possible. This properties demand time intensive modeling and an increased number of finite elements to describe the problem, leading to long CPU times and high memory consumption.

To overcome these obstacles one can consider representing the conductors as a combination of small straight line currents. Therefore it is assumed, that the cross-section of the wire is negligible for the generated field distribution on the cryostat shields. Following calculation scheme provides a good approximation for sufficient fine subdivisions of the wire pattern. According to Biôt-Savart's law the field generated by such a line source is determined by the curve integral

$$\boldsymbol{B}(\boldsymbol{r}) = \frac{1}{4\pi\nu} \int_C \frac{I\boldsymbol{dl} \times \boldsymbol{r'}}{|\boldsymbol{r'}|^3} \tag{2.52}$$

where I is the current amplitude within the line source and $\boldsymbol{dl}$ its differential.

2.6.2 Iterative transient solution

In this thesis two solution schemes are applied in the FE simulations. The method described in this section is a general transient approach [30] which is used in section 4.2.4 to calculate the fields in the FOV of the MRI system emitted by the secondary eddy currents (compare Fig. 2.9). After the introduction of this general approach a dedicated harmonic method is presented, which is applied for the simulation of eddy current losses in MRI cryostats.

For the transient solution of the differential equations it is necessary to also discretize the time. Here, a time-stepping algorithm using a constant time step size Δt has been utilized. The implementation of this subdivison has different implications for the magnetic and mechanic equation. The magnetic equation 2.50 is parabolic and may be

addressed via an implicit backward Euler or backward difference scheme, a special case of the general trapezoidal difference rule for the time discretization [29]. Here the time derivative of $\boldsymbol{A}$ is approximated as

$$\dot{\boldsymbol{A}}(t) \approx \frac{\boldsymbol{A}(t_{n+1}) - \boldsymbol{A}(t_n)}{t_{n+1} - t_n} = \frac{\boldsymbol{A}_{n+1} - \boldsymbol{A}_n}{\Delta t} \tag{2.53}$$

where the indices n and $n+1$ denote the counters for the consecutive time steps. Using the backward difference scheme $\boldsymbol{A_{n+1}}$ is given by

$$\begin{aligned} \boldsymbol{A_{n+1}} &= \boldsymbol{A_n} + 0.5\Delta t \left(\dot{\boldsymbol{A}}_{\boldsymbol{n}} + \dot{\boldsymbol{A}}_{\boldsymbol{n+1}}\right) \\ \Rightarrow \dot{\boldsymbol{A}}_{\boldsymbol{n+1}} &= \frac{2\left(\boldsymbol{A}_{n+1} - \boldsymbol{A}_n\right)}{\Delta t} - \dot{\boldsymbol{A}}_{\boldsymbol{n}} \end{aligned} \tag{2.54}$$

For the hyperbolic mechanical equation 2.51 the Newmark method is employed, again a special case of the general trapezoidal scheme. Therein the relations between $\boldsymbol{u}$, $\dot{\boldsymbol{u}}$ and $\ddot{\boldsymbol{u}}$ are given by

$$\boldsymbol{u}_{n+1} = \boldsymbol{u}_n + \Delta t \dot{\boldsymbol{u}}_n + 0.25\Delta t^2 \left(\ddot{\boldsymbol{u}}_n + \ddot{\boldsymbol{u}}_{n+1}\right) \tag{2.55}$$

$$\dot{\boldsymbol{u}}_{n+1} = \dot{\boldsymbol{u}}_n + 0.5\Delta t \left(\ddot{\boldsymbol{u}}_n + \ddot{\boldsymbol{u}}_{n+1}\right) \tag{2.56}$$

To enable the numerical calculation, the weak formulation of the terms in equations 2.50 and 2.51 is formed. Therefore the equations are multiplied with appropriate test functions, followed by an integration over the underlying volume (also known as Galerkin method). The kernels of these integrals can then be expressed using the element shape functions. More detailed explanations can be found in many textbooks on FEM, like [30, pg. 66ff for mechanics and pg. 115ff for magnetics]. Eventually, from 2.51 one obtains the mechanical equation

$$\hat{\boldsymbol{\mathcal{K}}}_u \boldsymbol{u} + \hat{\boldsymbol{R}} \dot{\boldsymbol{u}} + \hat{\boldsymbol{M}} \ddot{\boldsymbol{u}} = \boldsymbol{F_L} \tag{2.57}$$

and from 2.50 the magnetic equation

$$\hat{\boldsymbol{\mathcal{K}}}_A(\boldsymbol{u})\, \boldsymbol{A} + \hat{\gamma}(\boldsymbol{u})\, \dot{\boldsymbol{A}} = \boldsymbol{\mathcal{J}} \tag{2.58}$$

introducing matrices describing the 'mechanical and magnetic stiffness' $\hat{\boldsymbol{\mathcal{K}}}_u$ and $\hat{\boldsymbol{\mathcal{K}}}_A$, velocity dependent damping $\hat{\boldsymbol{R}}$, electric conductivity $\hat{\gamma}$ and mass $\hat{\boldsymbol{M}}$ as well as the

right hand side vectors $\boldsymbol{F}_L$ and $\boldsymbol{\mathcal{J}}$ representing the Lorentz forces and eddy currents. The representation of equation 2.58 now explicitly indicates that the displacement $\boldsymbol{u}$ affects the 'magnetic' processes. $\hat{\boldsymbol{\mathcal{K}}}_A$ and $\hat{\gamma}$ depend on the current shape of the conductive components and therewith on the displacement. These coupled equations can not be solved analytically and are thus demanding a numerical approximation. Inserting equations 2.54 to 2.56 in 2.57 and 2.58 leads to an algebraic solvable approximation. Here an iterative approach is implemented for that purpose.

A principle outline of the iterative solving algorithm is given in figure 2.10. Starting with a set of boundary conditions and the geometry of the investigated system, first the magnetic equations are solved. This delivers an approximation for the coupling Lorentz forces. With these, the mechanical equation can be solved, yielding information about the provoked displacements. If these new displacements deviate more than a certain convergence criterion from the values before the execution of this iteration (e.g. $\frac{u_n - u_{n+1}}{u_n} < 10^{-3}$), they are reentered for another iteration step into the magnetic part with an implicit predictor-corrector algorithm. Consequently, this is repeated until all convergence criteria are met and the calculation can be proceeded with the next time step.

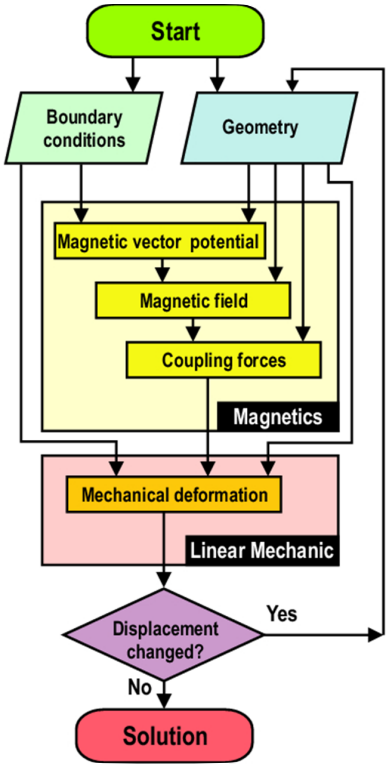

Figure 2.10 – Illustration of the solution algorithm used for the transient iterative solver. The image is taken from [30].

Note, that the geometry for the 'magnetic' system is updated for every iteration, adapting the finite element shapes to the estimated displacements. Therewith a so-called 'moving mesh' method results. Occurring movements are translated into a change of the coordinates of the finite elements, while keeping the distortion of the elements minimal. This is a time consuming task for the CPU so it is recommended to minimize the regions in the FE mesh where the geometry updating is performed.

For transient simulations of purely magnetic setups performed in this work (occurring in the sections 3.2.1 to 3.2.3 and 4.2.4), the iteration loop is obviously not required, since no coupling to mechanical movements needs to be considered.

2.6.3 Harmonic matrix coupled solution

The magnetomechanical interactions investigated in this work take place within the cryostat or more precisely in the conductive shields. The distance between these shields and the main coils generating the static $\boldsymbol{B_0}$ field is in the order of a few centimeters. Consequently, the field strength at the shields is significantly greater than at the isocenter. For 3 T systems the B_z field can reach values up to 5 T. Comparing this to the excitation fields of the gradient coils, reaching amplitudes in the small mT range, it is comprehensible that the $\boldsymbol{B}$ terms in the discussed equations are mainly dominated by the static $\boldsymbol{B_0}$ field. This fact can be used to derive simplifications for the solution process. A corresponding FE solution method, as presented in the following, has been formulated by Landes [34] and is used throughout the thesis for the simulation of eddy current losses in the MRI cryostat.

All time-dependent terms are separated in a stationary and a dynamic part:

$$\boldsymbol{A} = \boldsymbol{A_0} + \boldsymbol{A_\sim}; \quad \boldsymbol{B} = \boldsymbol{B_0} + \boldsymbol{B_\sim}; \quad \boldsymbol{J_i} = \boldsymbol{J_0} + \boldsymbol{J_\sim} = \nabla \times \nu \boldsymbol{B_0} + \boldsymbol{J_\sim} \tag{2.59}$$

where the index "$\sim$" denotes the time varying part and "0" the constant terms. Consequently, the time derivatives of $\boldsymbol{A_0}$, $\boldsymbol{B_0}$ and $\boldsymbol{J_0}$ are zero. Substituting these separations in equation 2.50 gives

$$\nabla \times \nu \nabla \times \boldsymbol{A_\sim} + \gamma \dot{\boldsymbol{A}}_\sim - \gamma \dot{\boldsymbol{u}} \times \nabla \times \boldsymbol{A_\sim} = \boldsymbol{J_\sim} + \gamma \dot{\boldsymbol{u}} \times \boldsymbol{B_0} \tag{2.60}$$

Equation 2.51 can accordingly be rewritten

$$\hat{\boldsymbol{\mathcal{B}}}^\mathsf{T} \hat{\boldsymbol{c}} \hat{\boldsymbol{\mathcal{B}}} \boldsymbol{u} + \boldsymbol{R} \dot{\boldsymbol{u}} + \gamma (\dot{\boldsymbol{u}} \times \boldsymbol{B_0}) \times \boldsymbol{B_0} - \rho_m \ddot{\boldsymbol{u}} - \gamma \dot{\boldsymbol{A}}_\sim \times \boldsymbol{B_0} = -\boldsymbol{J_\sim} \times \boldsymbol{B_0} - \boldsymbol{Q_1} - \boldsymbol{Q_2} \tag{2.61}$$

Two new substitutions are applied herein

$$\boldsymbol{Q_1} = \boldsymbol{J_0} \times \boldsymbol{B_0} + \boldsymbol{J_0} \times \boldsymbol{B_\sim} \tag{2.62}$$

$$\boldsymbol{Q_2} = \boldsymbol{J}_\sim \times \boldsymbol{B}_\sim + \gamma(\dot{\boldsymbol{u}} \times \boldsymbol{B_0}) \times \boldsymbol{B}_\sim + \gamma(\dot{\boldsymbol{u}} \times \boldsymbol{B}_\sim) \times \boldsymbol{B_0} - \gamma \dot{\boldsymbol{A}}_\sim \times \boldsymbol{B}_\sim + \gamma(\dot{\boldsymbol{u}} \times \boldsymbol{B}_\sim) \times \boldsymbol{B}_\sim \tag{2.63}$$

A further substitution is

$$\boldsymbol{Q_3} = \gamma \dot{\boldsymbol{u}} \times \nabla \times \boldsymbol{A}_\sim \tag{2.64}$$

which simplifies equation 2.60 to

$$\nabla \times \nu \nabla \times \boldsymbol{A}_\sim + \gamma \dot{\boldsymbol{A}}_\sim - \gamma \dot{\boldsymbol{u}} \times \boldsymbol{B_0} = \boldsymbol{J}_\sim + \boldsymbol{Q_3} \tag{2.65}$$

The $\boldsymbol{Q}$-terms introduced here, are neglected in the linearized simulation scheme. This can be justified as follows, when considering the context of the application within MRI systems as well as the boundary conditions of the simulations:

- $\boldsymbol{Q_1}$ represents the forces caused by interactions with the currents generating the static $\boldsymbol{B_0}$ field. These currents are only flowing in the superconductive main coils. By assuming the main coils to be fixed to their initial position, $\boldsymbol{Q_1}$ can be neglected.
- $\boldsymbol{Q_2}$ contains only forces that depend on an interaction of two or more time dependent variables. As these forces result from products of small quantities their contribution to the total forces will be very small and can thus be ignored.
- $\boldsymbol{Q_3}$ stands for currents that are induced by movement of conductive parts within the alternating field only. Therefore a similar argument as for $\boldsymbol{Q_2}$ applies, for the term does not significantly change the coupling behavior.

A first confirmation of the presented approach has been reported in [35, 36], demonstrating that the influence of these $\boldsymbol{Q}$-terms in case of high $\boldsymbol{B_0}$ is negligible. This was also validated, for an axial symmetric problem using a fully nonlinear approach as developed in [4]. So, in case of $\boldsymbol{B_0}$ fields, dominating the magnetomechanical coupling, the system can be approximately described by two reduced equations

$$\hat{\boldsymbol{\mathcal{B}}}^\mathsf{T} \hat{\boldsymbol{c}} \hat{\boldsymbol{\mathcal{B}}} \boldsymbol{u} + \boldsymbol{R} \dot{\boldsymbol{u}} + \gamma(\dot{\boldsymbol{u}} \times \boldsymbol{B_0}) \times \boldsymbol{B_0} - \rho_m \ddot{\boldsymbol{u}} - \gamma \dot{\boldsymbol{A}}_\sim \times \boldsymbol{B_0} = -\boldsymbol{J}_\sim \times \boldsymbol{B_0} \tag{2.66}$$

$$\nabla \times \nu \nabla \times \boldsymbol{A}_\sim + \gamma \dot{\boldsymbol{A}}_\sim - \gamma \dot{\boldsymbol{u}} \times \boldsymbol{B_0} = \boldsymbol{J}_\sim \tag{2.67}$$

Thereby all time dependent terms with an order higher than 1 are neglected, resulting in a linearization of the equations. This reduction of complexity allows the usage

of a faster solving algorithm, which directly calculates the results without the time consuming iterative procedure.

For the numerical calculation, the weak formulation of each term is formed. This time, however, explicit magnetomechanical coupling terms ($\hat{\boldsymbol{\mathcal{C}}}_{uu}$, $\hat{\boldsymbol{\mathcal{C}}}_{uA}$ and $\hat{\boldsymbol{\mathcal{C}}}_{Au}$) occur. As a result the system can be described with a linear matrix equation.

$$\begin{pmatrix} \hat{\boldsymbol{\mathcal{K}}}_u & 0 \\ 0 & \hat{\boldsymbol{\mathcal{K}}}_A \end{pmatrix} \begin{pmatrix} \boldsymbol{u} \\ \boldsymbol{A}_\sim \end{pmatrix} + \begin{pmatrix} \hat{\boldsymbol{R}}_{uu} + \hat{\boldsymbol{\mathcal{C}}}_{uu} & \hat{\boldsymbol{\mathcal{C}}}_{uA} \\ \hat{\boldsymbol{\mathcal{C}}}_{Au} & \hat{\gamma}_{AA} \end{pmatrix} \begin{pmatrix} \dot{\boldsymbol{u}} \\ \dot{\boldsymbol{A}}_\sim \end{pmatrix} + \\ + \begin{pmatrix} \hat{\boldsymbol{M}} & 0 \\ 0 & 0 \end{pmatrix} \begin{pmatrix} \ddot{\boldsymbol{u}} \\ \ddot{\boldsymbol{A}}_\sim \end{pmatrix} = \begin{pmatrix} \boldsymbol{F}_\sim \\ \boldsymbol{\mathcal{J}}_\sim \end{pmatrix} \tag{2.68}$$

The novel $\hat{\boldsymbol{\mathcal{C}}}$-matrices cover certain coupling effects within the system, which can be described as follows:

$\hat{\boldsymbol{\mathcal{C}}}_{uu}$ is an additional damping due to Lorentz forces, that aims to constrain any movement within the spatial inhomogeneities of the static $\boldsymbol{B_0}$ field (Lenz's rule)

$\hat{\boldsymbol{\mathcal{C}}}_{uA}$ characterizes forces generated by time varying magnetic fields

$\hat{\boldsymbol{\mathcal{C}}}_{Au}$ represents the motional eddy currents, which cause the additional damping $\hat{\boldsymbol{\mathcal{C}}}_{uu}$

For the calculation of the energy deposition within the MRI cryostat, the relevant state of the system is a steady state oscillation. Thus, one can assume the time behavior of $\boldsymbol{u}$ and $\boldsymbol{A}_\sim$ to be solely described by $\exp(i\omega t)$. Applying this harmonic ansatz allows transferring the equation 2.68 from the time domain into the frequency domain. After evaluating the time derivatives, the factor $\exp(i\omega t)$ cancels out and a dependency on ω remains. Note, that phase information between the oscillating quantities is maintained as the terms remain complex valued.

$$\begin{pmatrix} \hat{\boldsymbol{\mathcal{K}}}_u + i\omega(\hat{\boldsymbol{R}}_{uu} + \hat{\boldsymbol{\mathcal{C}}}_{uu}) - \omega^2 \hat{\boldsymbol{M}} & i\omega\hat{\boldsymbol{\mathcal{C}}}_{uA} \\ i\omega\hat{\boldsymbol{\mathcal{C}}}_{Au} & \hat{\boldsymbol{\mathcal{K}}}_A + i\omega\hat{\boldsymbol{\gamma}}_{\boldsymbol{AA}} \end{pmatrix} \begin{pmatrix} \boldsymbol{u} \\ \boldsymbol{A}_\sim \end{pmatrix} = \begin{pmatrix} \boldsymbol{F}_\sim \\ \boldsymbol{J}_\sim \end{pmatrix} \tag{2.69}$$

Applying this scheme allows a simplified calculation of the steady state behavior of the harmonically excited magnetomechanically coupled system at the given frequency ω.

3 Investigations on magnetomechanically induced eddy current losses

The first part of the following section will cover how the FE analysis can aid in understanding, describing and predicting the magnetomechanical coupling within the MRI cryostat, dealing with eddy current losses (ECL). Therefore, a few examples combining measurements on prototype setups and FE simulations will be presented. These examples are gradually increasing in complexity regarding the demands for the underlying FE model. It starts with the relatively simple axial symmetric problem of an experimental setup describable with the linearized harmonic (Sec. 2.6.3) simulation approach.

The axial symmetric simulations are used to demonstrate the basic properties of measured and simulated ECL spectra. A clear correspondence between the numerical and experimental results will be demonstrated by applying it to improve the ECL behavior of a Z-gradient coil prototype.

Before the 2D model is expanded to 3D, to also cover non axial symmetric gradient coils, the most crucial aspects for the successful transition and the expected achievable accuracy of the simulations are addressed. Several experiments and simulations are presented supporting the optimization of a Y-gradient coil in terms of ECL performance.

3.1 Simulation of eddy current losses for axial symmetric field gradients

3.1.1 Frequency spectrum of gradient coil fields

A main aspect of the following simulations and measurements is the excitation of eigenmodes within the cryostat. To excite a mode, the exciting force must be applied at a frequency close (with respect to the quality factor of the mode) to the eigenfrequency of the mode. The origin of the excitation discussed in this work is the current flowing in the gradient coil. It generates the electromagnetic fields driving the investigated magnetomechanical interactions.

To estimate which modes an MRI sequence can excite, it is thus necessary to know which frequency components are contained in the temporal switching of the gradients. The frequency spectrum $\mathcal{I}(\omega)$ of a temporal function $I(t)$ can be calculated by using the Fourier transform in the time domain.

$$\mathcal{I}(\omega) = \int_{-\infty}^{\infty} I(t) \exp(-i\omega t)\, dt \tag{3.1}$$

For sums of infinitely long, purely sinusoidal functions the frequency spectrum only contains the frequencies of the given sine waves. For all other functions and sinusoidal terms that are of finite length, a combination of different frequencies is contained in the spectrum. Real gradient currents are never infinitely long and also never perfectly sinusoidal. The fields produces by the GC during an MRI sequence are consequently containing a variety of frequencies.

To give a short example, an estimation of the dominant frequencies of a blipped EPI, as explained in section 2.2.4, is calculated in the following. The most active gradient in this sequence is the alternating read-out gradient (compare Fig. 2.5). The overall power put into the read-out gradient is clearly surpassing the remaining GC activity. Thus, the frequency spectrum of the generated magnetic fields is also mainly defined by the waveform of this oscillating gradient. The waveform typically utilized is formed trapezoidal, consisting of time intervals when the gradient current is either linearly

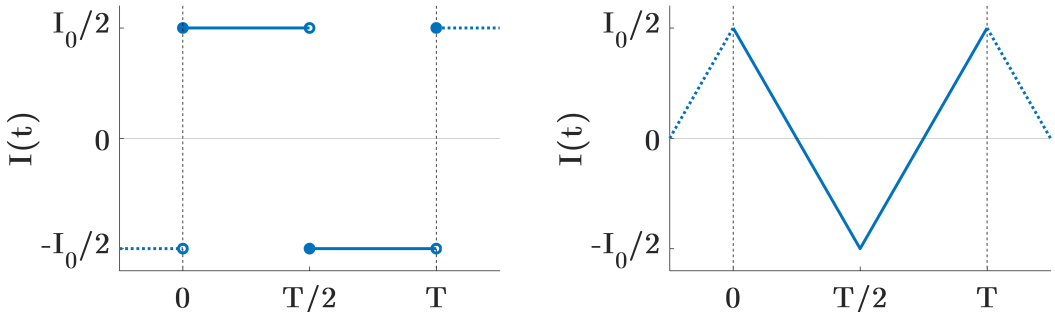

Figure 3.1 – Illustration of a periodic boxcar (left) and a triangle (right) waveform used to estimate the frequency spectrum of a trapezoidal waveform.

changing or staying constant. The proportions of this intervals can vary, depending for example on the chosen echo spacing $T_{E_{\mathsf{EPI}}}$. Making a statement concerning a general trapezoidal waveform is possible by considering the two borderline cases for the relation of linearly changing and constant gradient intervals. These cases are described by a boxcar and a triangle waveform (see Fig. 3.1).

To calculate the frequency spectrum of the boxcar waveform it is assumed, that the function repeats infinitely often with frequency $\omega_{\mathsf{EPI}} = \frac{2\pi}{T}$, allowing to limit the complete description to the time interval $[0,\, T[$.
The boxcar function (left plot in Fig. 3.1) is given as

$$I(t) = \begin{cases} \frac{1}{2} I_0 & \text{for } t \in \left[0,\, \frac{T}{2}\right[\\ -\frac{1}{2} I_0 & \text{for } t \in \left[\frac{T}{2}, T\right[\end{cases} \tag{3.2}$$

Since $I(t)$ is a real periodic function the general Fourier Transfromation can be reduced to a calculation of Fourier coefficients a_n and b_n, as only frequencies $\omega_n = n\,\omega_{\mathsf{EPI}}$ with $n \in \mathbb{N}_0$ possess non-vanishing contributions [37].

$$I(t) = \frac{a_0}{2} + \sum_{n=1}^{\infty} a_n \mathsf{cos}(\omega_n t) + b_n \mathsf{sin}(\omega_n t) \tag{3.3}$$

$$a_n = \frac{1}{T} \int_0^T I(t) \cos(\omega_n t)\, dt \quad | \quad n \in \mathbb{N}_0 \tag{3.4}$$

$$b_n = \frac{1}{T} \int_0^T I(t) \sin(\omega_n t)\, dt \quad | \quad n \in \mathbb{N} \tag{3.5}$$

For the given example function 3.2 a_n vanishes, since $I(t)$ is symmetric and $\cos(\omega_n t)$ is anti-symmetric to $t = \frac{T}{2}$. Thus, the sepctrum of $I(t)$ is described by

$$b_n = \frac{I_0}{2T} \int_0^{T/2} \sin(\omega_n t)\, dt - \frac{I_0}{2T} \int_{T/2}^{T} \sin(\omega_n t)\, dt = \frac{1}{n} \frac{I_0}{2\pi} (1 - \cos(\pi n)) \tag{3.6}$$

As consequence, for even n the coefficients become zero, so that $I(t)$ only contains odd multiples of ω_{EPI}. The contribution of these higher order frequencies thereby reduces with $\frac{1}{n}$.

Analogously, one can calculate the Fourier coefficients for the function plotted on the right of figure 3.1 (see App. A.1). In contrast to the boxcar function it represents the borderline case of a trapezoidal waveform switching with no constant gradient interval. Due to symmetry b_n is 0 and a_n yields

$$a_0 = 0 \quad \text{and} \quad a_n = \frac{1}{n^2} \frac{I_0}{\pi^2} (1 - \cos(n\pi)) \mid n \in \mathbb{N} \tag{3.7}$$

Here also all even orders vanish and the remaining odd higher harmonic frequencies only contribute to the signal with a factor of $\frac{1}{n^2}$.
Consequently, the boxcar function is the less favorable waveform for the blipped EPI read-out concerning additional frequency components. It yields the limit for the largest contribution of the n-th higher harmonic to the spectrum of an EPI read-out waveform besides the fundamental frequency as $\frac{1}{n}$ of the driving frequency amplitude. Since the gradient slew rate is limited in reality, an increase of the EPI frequency (reducing $T_{E_{\mathrm{EPI}}}$), can demand the shape of the EPI waveform to gradually turn from trapezoidal to triangular. The slope of the rising current can not be infinitely steep, requiring shorter constant plateaus in the trapezoidal shape for high frequency applications. In practice, this leads to less contributions (converging to $\frac{1}{n^2}$) of higher harmonics for high driving frequencies.

3.1.2 Eddy current loss measurements

The first magnetomechanical problem to be addressed here, are the eddy current losses (ECL) produced by a prototype setup of a Z-GC in a 1.5 T MR magnet. This specific prototype design shows an insufficient performance in preventing ECL on the HeV, demanding significantly increased active cooling compared to similar systems, which is undesirable. In general, each gradient activity produces ECL according to its frequency content. The following considerations concentrate on the EPI sequence, to allow an easier transition to the later addressed EPI ghosting investigations.

The ECL is generated via the ohmic resistance of the material times I_{ECL}^2. For a steady state oscillation triggered by the GC current, I_{ECL} induced by movement in the $\boldsymbol{B_0}$ field has the same frequency as the driving current. Thus, the dominant ECL produced by a blipped EPI contains contributions of odd higher n-th order harmonics going with $1/n^2$ in the worst case (boxcar waveform), due to the I_{ECL}^2 dependency.
To estimate the ECL for EPI it is hence important to check higher harmonic frequencies for ECL that might significantly contribute. For the Z-gradient the main contribution to ECL typically occurs at frequencies in the range between $1500\,\mathrm{Hz}$ and $3000\,\mathrm{Hz}$. The ECL at these frequencies is potentially more than ten times higher than in the frequency range of the typical EPI read-out gradient oscillation (roughly $300\,\mathrm{Hz}$ to $1300\,\mathrm{Hz}$; see Sec. 2.2.4). This outweighs the $1/n^2$ factor for third order harmonics, which consequently are essential to consider for the correct estimation of ECL produced by EPI.

For measuring the ECL a sinusoidal GC current is sweeped over the frequency range of interest. A direct measurement of the ECL is, however, not possible for systems that are in operation. In order to preserve the superconducting state of the main magnet, heat sensors or other measurement devices can not be placed easily within the cryostat, since the HeV has to be isolated from the outside by the other cryostat shields. Such links to the 'hot' environment spoil the quality of the shielding. Furthermore, not a single spot on the vessel is of interest for the ECL, but the vessel structure as a whole. Thus, direct measurements would need numerous sensors to cover the relevant area, making it even less feasible.

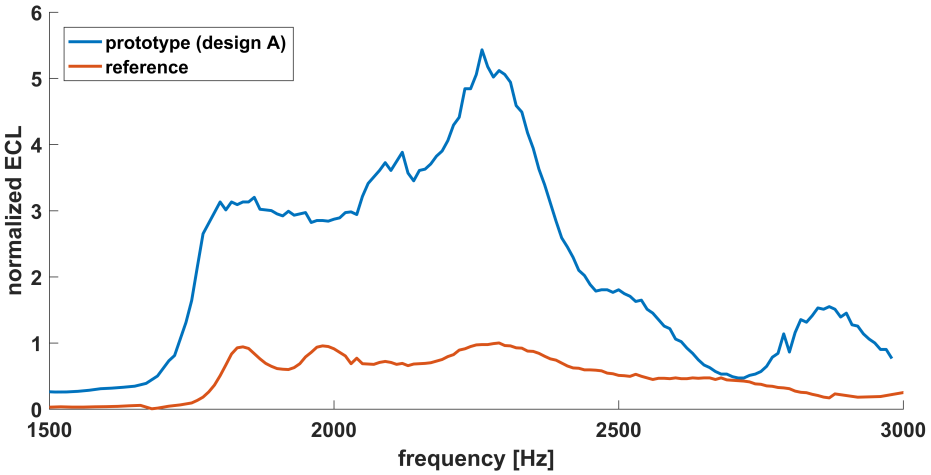

Figure 3.2 – ECL measurements for an already commercially available system (reference) and the investigated prototype setup. For this and all further ECL plots, the losses are normalized to the maximal value of this reference ECL spectrum.

Consequently, the measurement results are achieved via an indirect measurement, which represents the change in power consumed by the cooling system. From this it is clear, that the ECL, as it is measured, is not directly comparable to the calculated values. In addition the measurement is continuously sweeping over frequencies (making it less time-consuming). However, this implies an influence of neighboring frequencies onto each other (depending on the frequency sweep direction), resulting in a 'blurring' of the spectrum.
Yet, strong resonances occur clearly in the measurement and should be reproducible by the simulation. But it is also expected, that the quality factor of the measured peaks is smaller compared to the simulated ones.

In figure 3.2 the ECL spectrum for the mentioned prototype is plotted together with a representative spectrum of a commercially available MRI system (production year 2010). All ECL values presented in this works are normalized with the maximal value of this reference spectrum. This comparison visualizes how problematic the prototype design is in the context of cooling demands. Note that the plots are limited to the interesting frequency range for Z-gradient application above 1500 Hz, since below that frequency no significant ECL is observed.

The first goal of the applied FE simulations has been to reproduce the measured data. In the following sections a few more general considerations will be described, which have been used to simplify the simulation approach.

3.1.3 General simulation setup

The key to an efficient FE-model is to make it detailed enough to be accurate but also as coarse as possible to minimize computational costs (like CPU time and memory demands). It needs to be assessed which effects are important to describe the processes of interest correctly and which are of minor importance or even irrelevant. This section will cover such considerations for the magnetomechanical simulations performed in this thesis.

To cover the magnetomechanical processes within the MRI cryostat, the FE-model needs to contain the spatial distribution of the magnetic fields generated by the main magnet coils as well as by the GC. Typically the conductors of these coils are made of several wires which are closely packed. To keep the model simple, these packages are described as structures with rectangular cross-sections and a representative current density of the involved wires (compare Fig. 3.4). For the superconductors in the main coils, made of hundreds of single wires, this even translates to packages of a few centimeters side length. The meshing criteria for the conductors are relatively loose compared to the demands coming from the mesh needed on the cryostat. Due to the small distance between the coils and the cryostat, the element size used on the cryostat more or less dictates the mesh size in the conductors. An abrupt transition between large and small element sizes can become numerically unreliable.

This simplification of combining wires has to be considered in the assignment of the material parameters of the conductors. Using the actual conductivity of the wire material does not reproduce the correct behavior in the simulation, as the region where eddy currents flow is falsely represented. The composition of several closely arranged wires is much less prone to the induction of eddy currents than a solid structure. Hence, the conductivity of the conductors has to be drastically reduced, compared to the actual material used, to compensate for the simplified geometric modeling.
In general, the mesh of an object has to be adapted to the function and properties

it has in the simulation. For instance the number of elements used to cover the thickness of a shield is dependent on the penetration depth of the eddy currents. For the simulations conducted here it is not necessary to use more than one element in the outer bores of the cryostat, since the gradient stray field at that point is negligible. Dominant interactions happen mainly on the inner bores.

Still the modeling of the outer bores can not be omitted, although most magnetomechanic interactions happen at the inner bores. For the correct description of the mechanical behavior of the inner bores the remaining cryostat defines a non-trivial mechanic boundary condition, which introduces additional eigenmodes and allows a more accurate reproduction of the vessel movements.

Inside the cryostat a helium bath is cooling the superconductors. For the simulations the helium is treated identically to the air surrounding and in between the shields. With the modeling of the surrounding air of the MRI system the question arises at which distance the model can be truncated without artificially introducing errors in the magnetic fields due to inaccurate boundary conditions. Since the fringe field of the main magnet is several orders of magnitude greater than the GC stray field, it is commonly the relevant quantity to be considered here. For special cases one can calculate the vector potential of the main magnetic field analytically for every element at the borders of the simulation model and use it as boundary condition. This allows a spatially restricted model, but is laborious to implement. Thus, usually a boundary condition at approximately one meter from the OVC, setting the magnetic flux to be parallel to the outer surfaces, is used and has proven to give reasonable results for the investigated setups.

3.1.4 Axial symmetric mesh

To reduce the complexity of the models utilized for the simulations, some simplifications concerning the GC geometry are made. Each loop of the gradients and main coils is assumed to be individually driven by current, so that there are no connections between them (see Fig. 3.3). This measure yields gradient coil geometries that are symmetric to the x-y-plane. It should, however, be considered, that the current directions of the Z-gradient and the main coils possess different symmetries. Consequently, the x-y-plane symmetry can not be exploited, when Z-gradient and main magnet fields are calculated

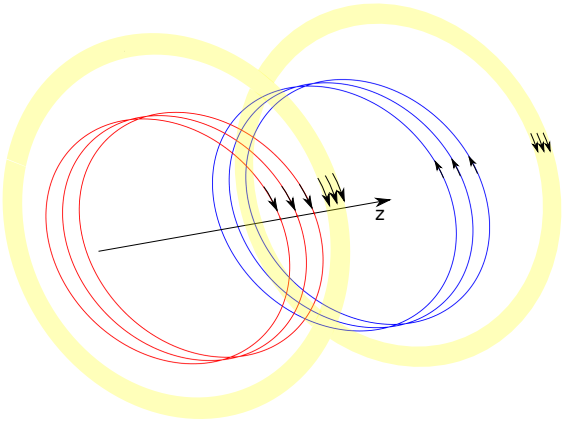

Figure 3.3 – Schematic illustration of a Z-GC. The main magnet coils are represented by the yellow circles. Arrows indicate the direction of current flowing in the conductors. Due to the axial symmetry of the Z-GC a reduction of the FE model to 2D is possible.

simultaneously. Yet, a significant reduction of complexity is achieved with the above mentioned simplification, since the Z-gradient and the main magnet conductor paths become perfectly circular, allowing a reduction of the model dimensions from 3D to 2D due to axial symmetry. The corresponding cylindrical coordinate system is described with r_c, φ_c and z, being the radial, circumferencial and axial component (see App. A.2).

Theses symmetries, deduced from considerations of the magnetic setup of the FE-Model, can only be applied in magnetomechanical simulations, if the mechanical parts share them. Due to this reason, the cryostat is also strongly simplified compared to the real assembly. Each vessel is reduced to two concentric hollow cylinders, an inner and an outer bore that are connected on both axial sides via the so-called 'shield ends'. Small parts like bolts, screws or mountings are neglected, facilitating the model complexity and thus reducing modeling efforts drastically. With this setup it is feasible to adopt to all possible symmetries given by the magnetic setup. Furthermore, the simple cylindrical geometry allows the usage of regular FE grids, an advantage in terms of modeling time, mesh control and thus numerical stability. The CPU time for meshing with a regular mesh is short compared to free meshing. Thereby, element sizes can easily be adjusted, so that elements with large aspect ratios and too fast transitions in neighboring element sizes, which potentially lead to numerical problems or inaccuracies, can be avoided.

Yet, the simplification of the model for complying with symmetries comes on the cost of possible deviations from reality. This means that every result calculated with these models has to be assessed with regards to whether the idealization has led to a negligence of important effects.

An additional measure to save computation time is to minimize the number of elements carrying magnetomechanical interactions. The GC and main magnet coils as well as the air and helium elements are not supposed to move and can be excluded from the mechanical formulation. However, the elements in direct contact with the cryostat vessels should be included in the mechanical description. Due to the moving mesh ansatz utilized to describe the vessel movements, these elements need to be 'motile', so they do not prohibit the movement of the nodes which are part of the vessels boundary surfaces.

Figure 3.4 shows an exemplary 2D model of a simulation model used for the ECL calculations of z-gradients. The geometries of the main magnet coils, the cryostat and the GC conductors obviously have to be adapted for the different magnet and GC setups. The principal mesh properties (axial element length or the number of elements along the thickness of a vessel), however, were kept identical for the following simulations. With the reduction of the model to a 2D setup, the saving of computation power is so massive, that the meshing parameters have been willingly defined generously. Moreover, all axial symmetric simulations were setup with second order elements. Although these meshes were unnecessarily fine meshed, the simulation time remained in the order of minutes to cover the frequency range of interest. Thus, an optimization was not considered necessary here.

3.1.5 Damping calibration

As mentioned in section 2.5.1, a structural damping term is generally considered in the mechanical equations. A strict treatment of this damping term is not easy to establish due to a lack of material parameters. There are, however, different approaches to approximate the damping behavior. In this work so-called Rayleigh damping has been used. This method utilizes a mass proportional parameter R_α and a stiffness proportional

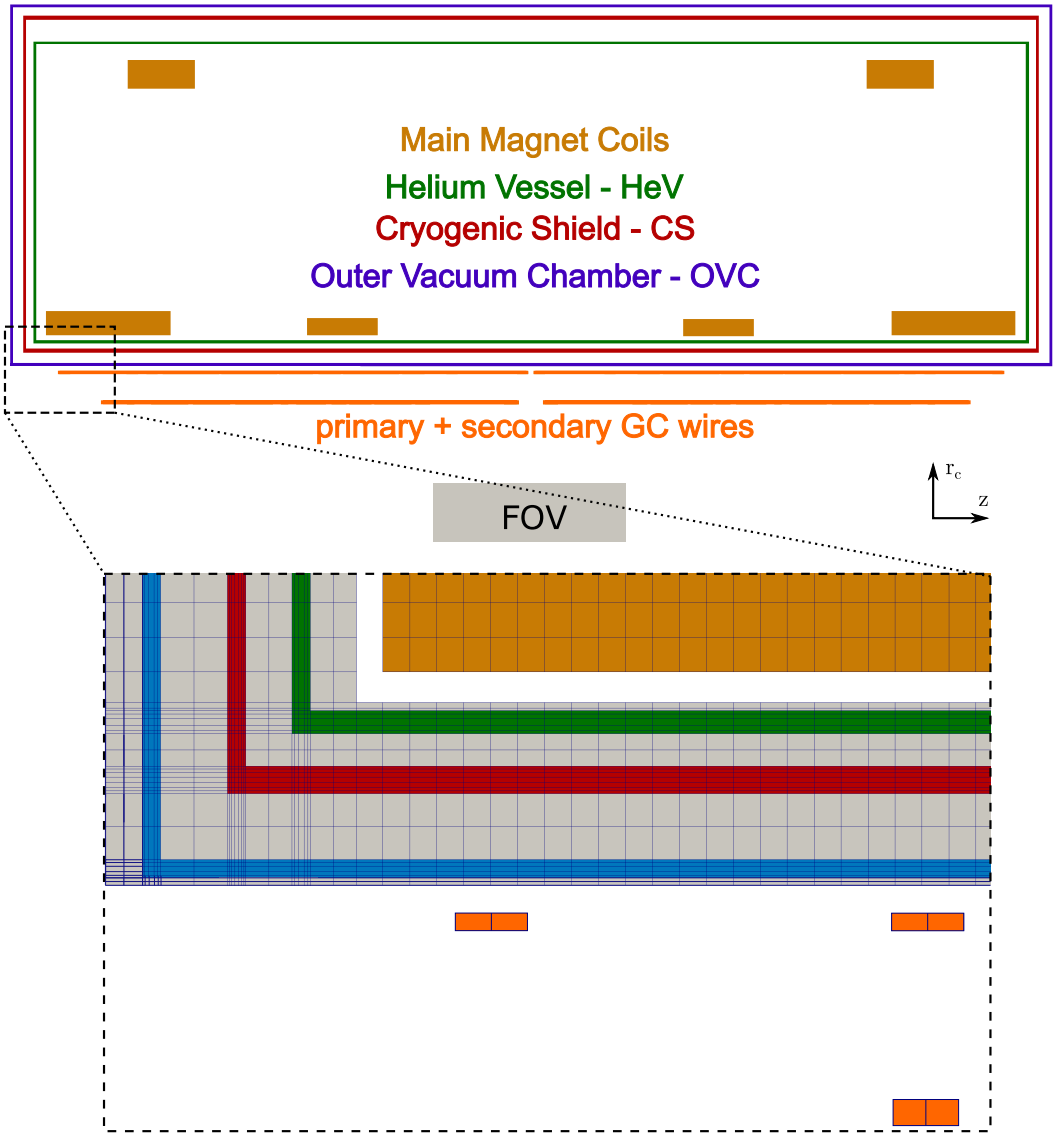

Figure 3.4 – Drawing of a representative 2D axial symmetric model containing a close-up of the corner connections between the inner bores and the ends of the modeled cryostat vessels. The close-up visualizes the meshing approach employed for the magnetic active and magnetomechanical interacting components. To avoid irregularities in the mesh a strict focus is placed upon compatibility to a quadrilateral mesh. Therefore the vessels were subdivided in several rectangles to support and easier control the meshing software. Along the thickness of the vessels several elements are defined to resolve skin effects of eddy currents. The gray regions shown in the image are representing air or respectively vacuum. In contrast to other regions representing air or vacuum, the elements also consider the mechanical equations. This is necessary to enable the application of a moving mesh ansatz to describe the movement of the vessels in the simulation.

parameter R_β to define the damping matrix by

$$\hat{\boldsymbol{R}} = R_\alpha \hat{\boldsymbol{M}} + R_\beta \hat{\boldsymbol{K}}_{\boldsymbol{u}} \tag{3.8}$$

This relation can be used on the element level, accounting for damping parameters of different materials. With this ansatz a frequency dependency of the damping is obtained, which is described by

$$\tan \delta_q = \frac{R_\alpha + R_\beta \omega_q^2}{\omega_q} \tag{3.9}$$

$\tan \delta_q$ represents the loss factor for the q-th eigenfrequency ω_q. The resulting equation of motion for this ansatz is an exponentially damped sine curve possessing a logarithmic decrement

$$\Lambda_q = \frac{2\pi \tan \delta_q}{\sqrt{4 - \tan^2 \delta_q}} \tag{3.10}$$

For further details it is referred to [28].

Finding appropriate values for the coefficients R_α and R_β was performed by reproducing the reference ECL spectrum already considered in section 3.1.2. For this calibration several combinations of R_α and R_β have been tested for the simulation of the ECL spectrum. The usual approach for calibration, using an analysis of the modal response to broadband mechanical excitations ('hammering test') on the cryostat structures, is not reliable, since these tests are hardly feasible at the actual cold temperatures. A successful transfer of the calibration using room temperature results would be very unlikely. Figure 3.5 shows a selection of the simulated spectra together with the measured data.

For all plotted simulation results a good agreement with the measurement is visible concerning the resonance frequencies. The eigenfrequencies are not influenced significantly by the damping. Comparing the simulations and the measurement also reveals, that the measurement is not resolving all the peaks observable in the simulations. In the simulations two peaks appear above 2500 Hz which can hardly be accounted for in the measurement. Also the measured single peak at 2300 Hz is probably due to the overlap of two closely adjacent resonances. Assuming the simulation reproduces occurring resonances correctly, these two examples give an idea of how much inaccuracy ('blur-

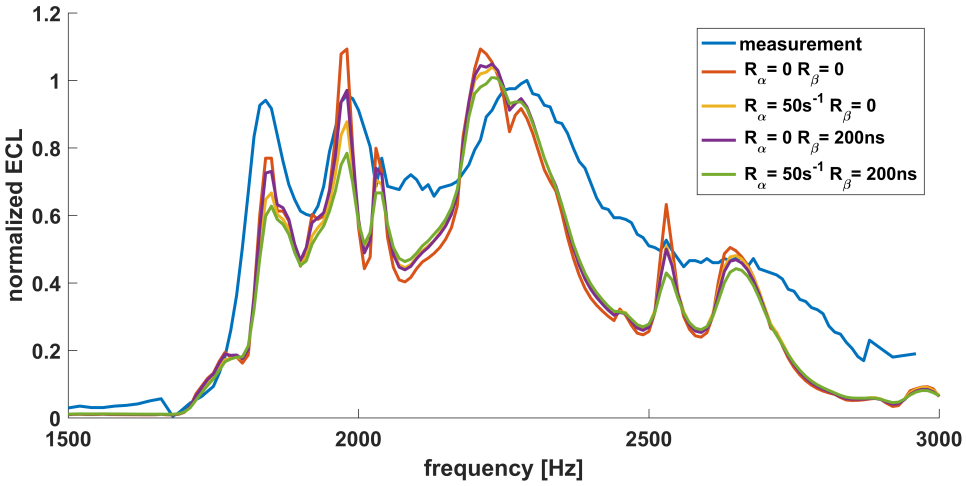

Figure 3.5 – ECL simulation results for various Rayleigh damping coefficient combinations in comparison to a measurement. $R_\alpha = 0$, $R_\beta = 200$ ns (purple) shows the best agreement in terms of maximal peak amplitudes within the studied frequency range.

ring') concerning the frequency is introduced by the sweeping done in the measurement. The aim of this damping study has been to find the Rayleigh parameter combination which is best suited for reproducing the real mechanical damping. The criterion to assess the damping values has been defined as the average deviation of measured and simulated peak amplitudes at their main resonance frequencies.

The combination of $R_\alpha = 0$ and $R_\beta = 200$ ns yields the least deviation of the investigated damping values. But in general, the damping approximation appears to be too simplified to reproduce the reality adequately, using only two variable parameters. The calibration of the damping approach could not provide a clear improvement of the solution accuracy for a wide frequency range.

In other words, the mechanical damping appears not to be a crucial property for correctly predicting occurring resonances, so further damping investigations were omitted and the $R_\alpha = 0$, $R_\beta = 200$ ns parameter combination was chosen for following simulations.

3.1.6 Simulation-based reduction of eddy current losses induced by axial symmetric gradient fields

For the reduction of the ECL spectrum several GC geometries have been investigated. Since the GC is designed to generate MR images, several other parameters besides the ECL need to be considered in the coil layout (e.g. field linearity, inductance, force compensation, conductor radii). According constraints have to be met additionally, when rearranging the wire pattern for ECL optimization, as the functionality for imaging has to be maintained. Consequently, only designs with the necessary GC properties have been evaluated.

Changes in the geometrical setup of the GC wires are seen by the cryostat as a modified stray field. Hence, it is reasonable to evaluate the stray field distribution in relation to the ECL losses. Figure 3.6 shows a plot of three different stray fields at the radius of CS. Design A corresponds to the initial prototype, whereas designs B and C are investigated alternative modifications. The modifications include variations in the number of conductors for both GC layers as well as adaptions of the axial conductor positions.

Considering the potential ohmic losses, going with J^2 and J itself going linear with B (Ampère's Law), the difference of the ECL between design A and B should be around a factor of 9 looking at the maximal amplitudes and roughly a factor of 5 comparing the overall value squared and integrated. Design B and C should, following this argumentation, produce similar ECL results, whereas the integral value for design C is a bit less than the value of design B.

In figure 3.7 the results of the according ECL simulations are presented. As expected the design A produces the highest ECL, but the relation between the maximal values is clearly different from the expectation. The factor separating designs A and C is approximately 25 and also between B and C a factor of 3 is observable at the maximum peaks. This clearly indicates a nonlinear resonant behavior of the system, demanding to consider more factors than just the overall amount of stray field to estimate the ECL.

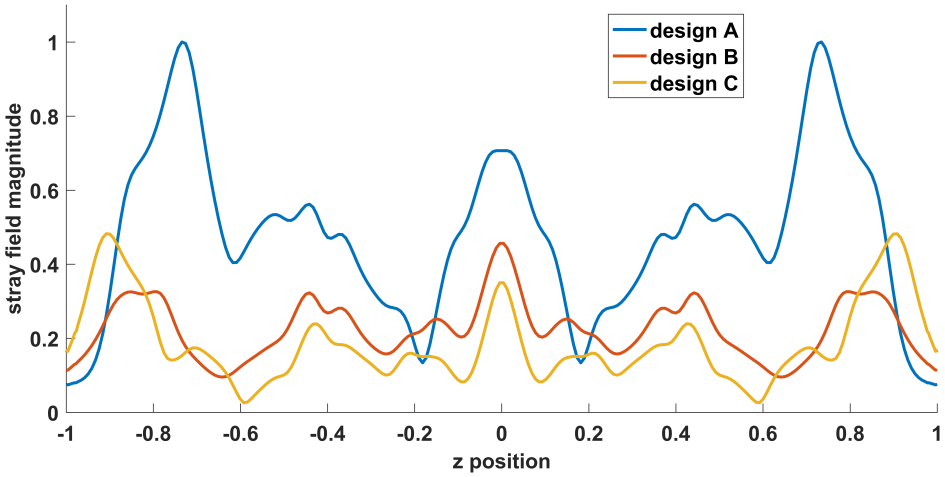

Figure 3.6 – The stray field magnitude for three different z-GCs at the radius of CS. The values are normalized to the maximal amplitude of design A which was the initial design of the prototype. Integrating and squaring the stray field gives a rough estimate of the energy which can be deposited in the cryostat. This estimate is about a factor 5 less for design B and C compared to A.

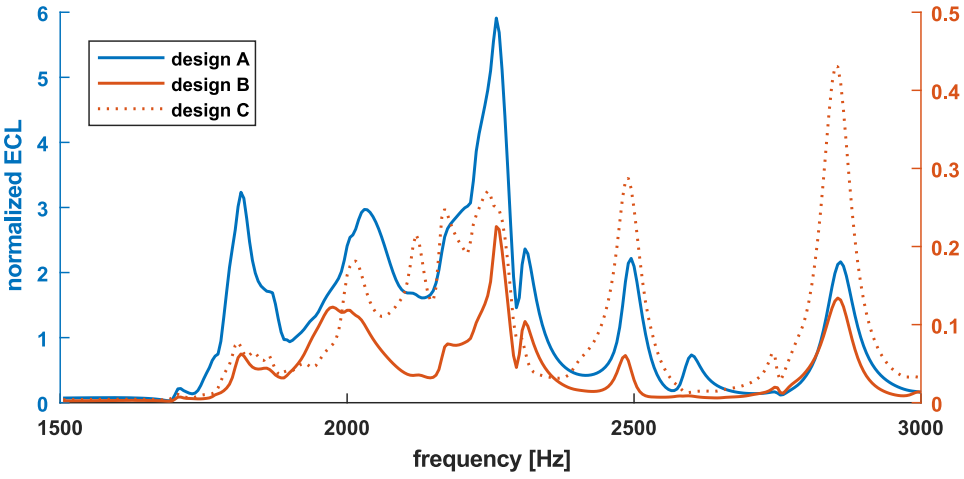

Figure 3.7 – ECL simulations for the three different stray field designs in figure 3.6. Note that designs B and C are plotted on the secondary axis.

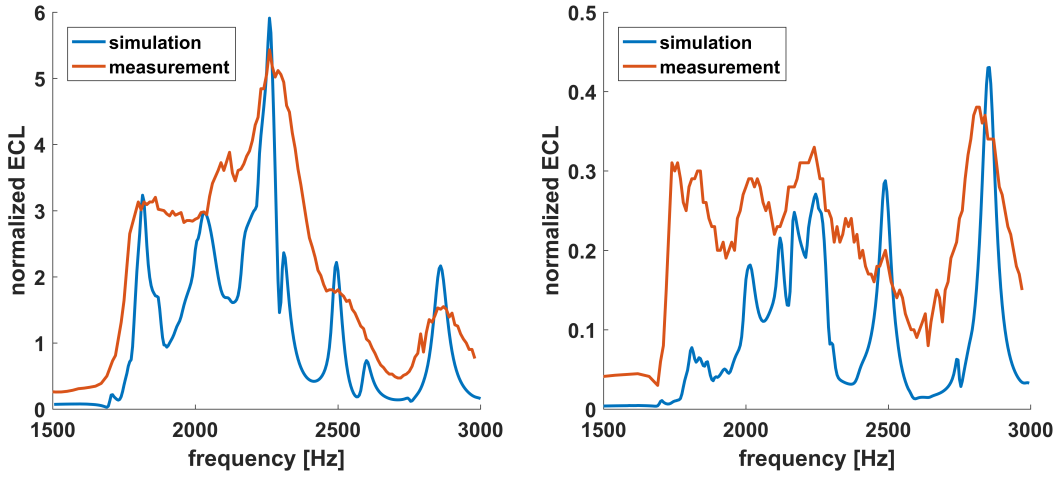

Figure 3.8 – Comparison of the simulated and measured ECL spectra for the initial (left) and the reworked prototype (right).

Concerning ECL simulation only, design B is the best choice out of the three regarding the ECL spectra. However, due to other performance specifications and mechanical production constraints, design C was chosen as reworked setup for the GC, since it is still producing sufficiently small ECL to fall under the limit set by the reference system (compare Fig. 3.2).

As a validation of the calculation, the ECL spectrum of the new prototype design was also measured. The comparisons of the two prototype measurements and the simulations are illustrated in figure 3.8. A more detailed discussion, regarding the reason of the strong ECL differences of the designs is given in section 4.2.2 (see Fig. 4.9 and Fig. 4.10).

As predicted the ECL was reduced significantly with the new GC design. In addition, the resonance frequencies as well as most peak amplitudes are in very good agreement between measurements and simulations. Since design C is already strongly optimized for reduced ECL, the differences due to the actual construction tolerances probably exert larger relative influences on the spectrum. The evident difference in measurement and calculation for design C between 1700 and $2100\,\mathrm{Hz}$ is ascribed to this circumstance.

3.2 Transition from 2D to 3D simulations

As shown in the previous section, the simulation of the ECL has proven to be very helpful for optimizing the GC design of an axial symmetric Z-gradient. This successful application motivated the utilization of this method for transversal gradient coils, as these coils generate eddy current losses as well, which need to be kept under a certain limit to avoid high cooling demands. Transversal coils, however, can not be treated with two-dimensional models, since no axial symmetry is present. Therefore, a 3D model had to be developed. In order to validate the 3D approach, a 3D setup for a Z-gradient has been constructed and compared to the axial symmetric equivalent simulation. Due to the increasing computational demands of 3D calculations, investigations concerning the necessary accuracy of the model and the discretization of the mesh have been conducted. The model is subsequently adapted for Y/X-GC demands. Parts of this transition from 2D to 3D and preliminary results related to transient simulations in section 4.2.4 have already been published [38].

3.2.1 Expanding the FE-model from 2D to 3D for an axial symmetric gradient field

Going from 2D to 3D simulations, the formulation for the finite elements used in the model has to be considered. Due to the smaller complexity in 2D simulations, it is sufficient to utilize so-called 'nodal' or Lagrangian elements. Nodal elements associate field quantities with the vertexes of the elements. This is potentially problematic, if the field is represented by a vector. According to [39] fulfillment of continuity requirements for approximated vector fields and application of boundary conditions can be troublesome using nodal elements. These problems can be overcome by utilizing so-called 'edge' or Nédélec elements. This type of element was first described in [40]. The advantages of edge elements for the description of Maxwells equations, however, were first recognized by Nédélec 23 years later [41]. These elements ascribe the field quantities to their edges instead of the vortexes. Since then, numerous FE applications dealing with eddy currents and electromagnetic fields made use of the edge element formulation, for example [42–45] to mention only a few.
According to [46] edge elements are an indispensable tool for FE-models containing interfaces between sub-domains with different material properties, as such elements,

for example, allow normal field components to jump across those interfaces. Yet, if such problems are overcome or avoided nodal elements are preferable due to the higher efficiency.

The step from 2D to 3D is connected with a large raise of complexity and thus computing demand, since at least one additional degree of freedom (depending on the quantity) is introduced and the number of elements is also increased. To see whether the transition to edge elements is necessary for the investigated 3D setup, a simple representative problem has been tested beforehand with a transient magnetic simulation.

A metallic hollow cylinder was modeled in 3D with a concentric coil inside, once with nodal and once with edge elements. As for the 3D simulations no higher order magnetic edge elements have been available, the 2D experiment has also been restricted to first order elements. The concentric coil was then driven with a constant current, followed by a rapid switch-off. This leads to eddy currents in the hollow cylinder, which try to maintain the magnetic flux. Due to the perfect axial symmetric coil geometry the magnetic field also possesses this perfect symmetry and accordingly the field produced by the eddy currents needs to show the same property.

An illustration of the eddy current distribution calculated with nodal and edge elements after a switch-off of the coil is shown in figure 3.9. The eddy currents are clearly not axial symmetric in the nodal case and consequently wrong. With the nodal formulation the simulation seems to converge to an additional spurious solution of the problem that is not resembling reality. Utilizing edge elements results in an axial symmetric solution as expected. Hence, the transition from nodal to edge elements is necessary for the 3D simulations applied in this work. But note that this problem of spurious solutions is not generally solved by using edge elements without a proper finite element formulation, as has been shown by Mur [47].

According to the shown results, the edge element formulation has been used for the further 3D simulations. In order to evaluate the consistency of 2D and 3D results in a more complex model, the simple setup shown above has been expanded to a complete 3D MRI model of a Z-gradient. For obtaining a quantitative statement the field has

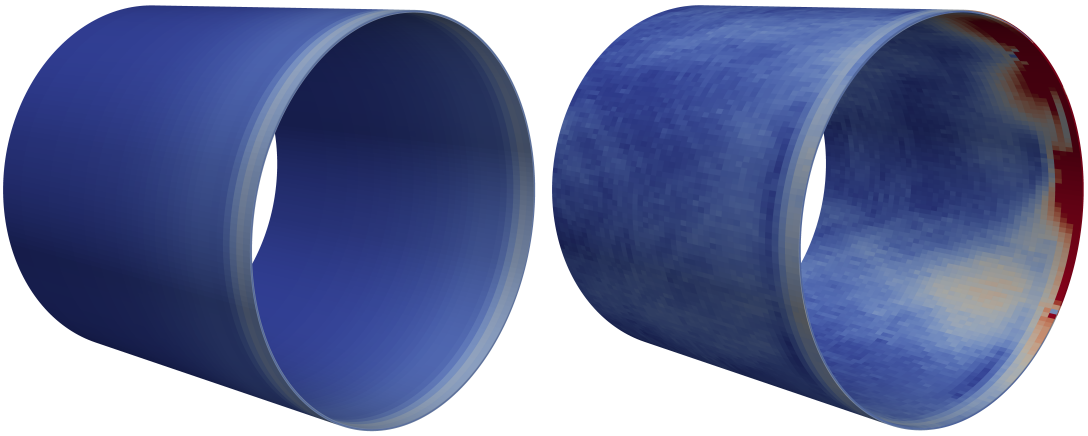

Figure 3.9 – Illustrations of the obtained eddy current distribution on a hollow metallic cylinder after a switch-off simulation of a concentric loop coil within the cylinder. On the left the result with edge elements is shown, on the right with nodal elements. The scale for the color coding is identical for both solutions, demonstrating the incorrectness of the nodal approach.

been evaluated at two points within the FOV of the magnet for both the 3D and the 2D case. The positions of the points are chosen symmetric to $z = 0$, allowing to estimate the field effects (in first-order approximation) of the eddy currents flowing within the cryostat, by

- subtracting the axial field values, providing information about the Z-gradient like field.
- averaging both values, giving the homogeneous field offset (B_0-offset).

In the setup investigated here no B_0-offset is observable, as only perfect symmetric Z-GCs with respect to $z = 0$ have been investigated. In section 3.2.2 asymmetric setups generating fields with B_0-offset will also be considered. In practice, B_0-offsets are occurring in real setups due to construction tolerances or connection wires between coil loops.

Two 3D models were constructed from the basic 2D setup (Fig. 3.4). One was generated by a rotation operation of the entire 2D mesh for 90° around the z-axis, while every 3° define an element slice. This typically leads to disadvantageous element shapes close to the axis of rotation with large aspect ratios. To avoid this, a second 3D model has been constructed similarly, with the difference that the inner 20 cm closest to the z-axis

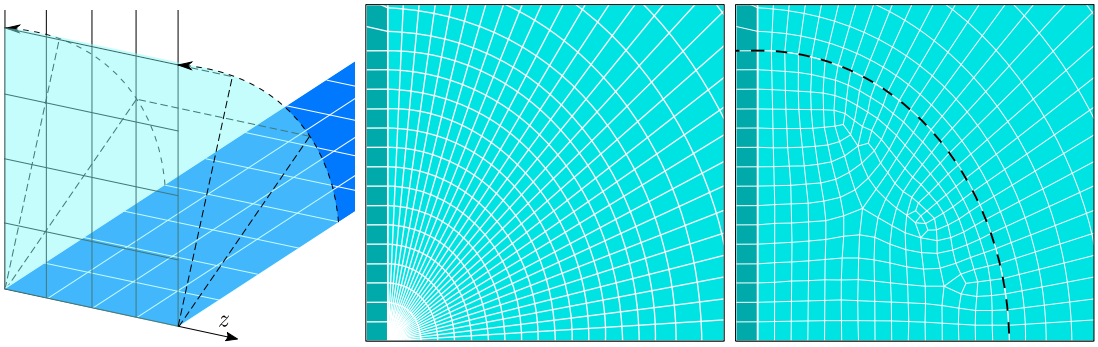

Figure 3.10 – Left) Scheme of the transition from a 2D mesh to a 3D mesh by rotation. Middle) Exemplary illustration of a completely axial symmetric 3D mesh with unfavorable element shapes close to the axis of rotation. Right) Image of a mesh where the region close to the axis of rotation (marked by the dashed line) was meshed without rotational sweep. The number of necessary elements is reduced and the element shapes look more advantageous concerning numerical accuracy. In this case the symmetry of the mesh is not reproducing the symmetry of the physics, which can degrade the approximation of the solution.

were not rotated alongside the rest of the model. This inner part is meshed separately, providing a well defined structure for the elements touching the axis of rotation. Figure 3.10 shows the different concepts.

The physical situation investigated is again the switch-off process of the coil, this time, however, for a complete MRI Z-gradient. Looking at the switch-off is preferable to the switch-on process, since the fields of the eddy currents are not superimposed to fields generated by the GC.

The comparison of the results of the two 3D meshes and the 2D mesh (see Fig. 3.11) yields an unexpected finding. A break of the symmetry of the mesh appears to introduce a greater error than disadvantageous aspect ratios close to $r_c = 0$. The agreement of the 2D results with the axial symmetric 3D results is remarkably good[1], proving that the step from 2D to 3D simulations was successfully accomplished. The disagreement with the non symmetric mesh motivates further considerations of geometrical irregularities, concerning the simulation results of magnetic fields in the FOV. In practice the GC

[1] In appendix A.3 it is demonstrated, that the rotated 3D mesh also shows a very good agreement for the harmonic matrix coupled solution.

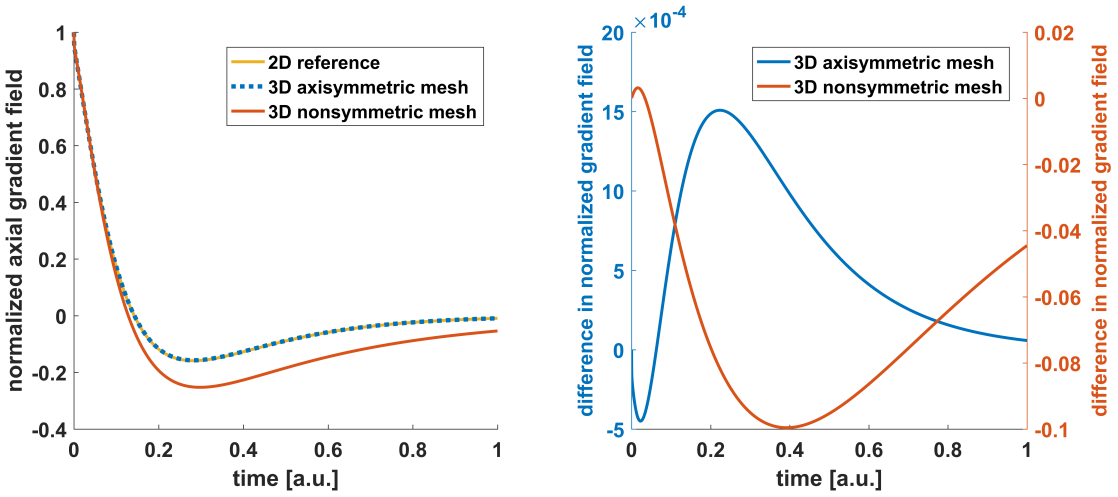

Figure 3.11 – Two plots showing the performance of the two 3D mesh approaches compared to the initial 2D mesh. Left) Evolution in time of the magnetic field gradient after a GC switch off calculated for the three meshes. The field is evaluated at the identical point in the FOV. Right) The corresponding deviation of the 3D meshes compared to the 2D mesh. For better visualization the non symmetric mesh results are relating the secondary y-axis of the plot.

setup is also not symmetric (i.e. due to construction tolerances covered in the next section) and it needs to be considered how this influences the comparability of field simulations and measurements.

Another interesting observation is that the sign of the magnetic field is changing during the investigated time. Since no more field is reaching the cryostat after the switch-off process, the eddy currents were expected to decay exponentially to 0, dissipating energy via the material resistance. If this change of sign is not an numerical error, it must be due to different decay time constants of currents that generate positive and negative field amplitudes respectively.

The time constant of eddy currents is proportional to their inductance and inversely proportional to the resistance of the carrying conductor. Due to the axial symmetry of the problem, all eddy currents form closed circles around the axis of rotation (they only possess a φ_c component). This allows to regard the eddy current distribution as a superposition of many, in axial direction narrow, 'elementary' neighboring circular eddy currents along the length of the inner bore. For these currents all resistances

and self-inductances are identical, since the CS is defined perfectly isotropic in the simulation. Contributions by the HeV and the OVC are not considered relevant, as only the CS vessel possesses a conductivity high enough to carry currents for the time span observed here. This leaves two possible explanations, if the simulation is trusted. Either the currents flowing on the CS ends are of significance here or an inductive coupling of the 'elementary' eddy currents provokes this behavior. The former could easily be excluded by simulating the process, while setting the conductivity of the ends to 0. The resulting signal showed only minor changes, so that the only potential explanation is to assume a coupling between the eddy currents influencing their decay.

The two preceding paragraphs raised two questions: To what extent can dynamic eddy current field simulations in the FOV be expected to be comparable to measurements and is the sign change of the field ascribable to coupling effects between the eddy currents? Both can be answered with the investigations on construction tolerances presented in the next section.

3.2.2 Influence of construction tolerances

In this section the decay behavior generated by slightly modified GC stray fields is investigated. Selections of conductor positions of a GC design were systematically modified to analyze the effects on the field decay. To facilitate the comparison of the results, this set of simulation experiments is conducted with another GC prototype, showing a field decay without sign change.

As mentioned in section 2.3 and illustrated in figure 3.4 the gradient coil contains two layers of conductors. The setup with a primary layer on smaller radius and a secondary layer on a larger radius is necessary to actively reduce the stray field of the GC. In the following the relative positions of these two layers are modified for a Z-GC setup. The modeling of the different conductor positions was realized using the Biôt-Savart approach described in section 2.6.1. Therewith the use of a single mesh for all GC variants was sufficient, as the coil conductors needed not be moddeled in the underlying mesh. In the appendix A.4 it is shown, that the Biôt-Savart currents yield a sufficiently precise approximations for the actual GC conductors.

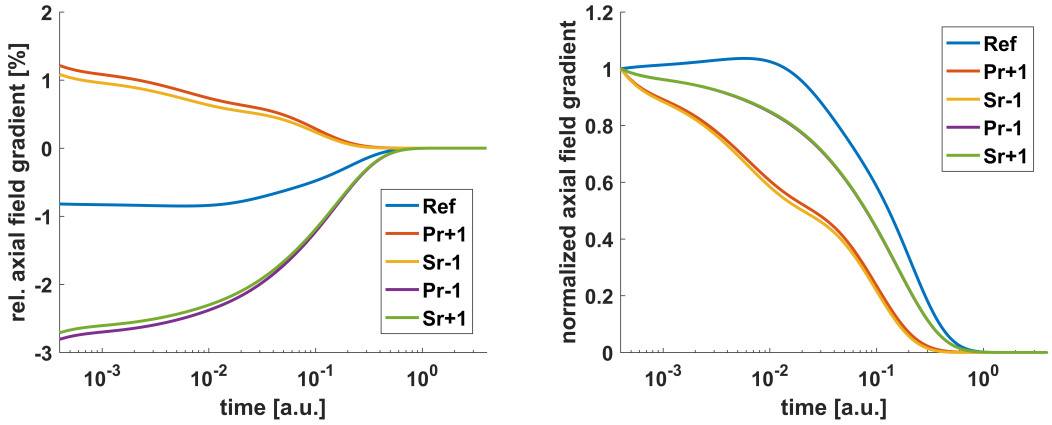

Figure 3.12 – Semi-logarithmic plots of the switch-off behavior produced by various GC modifications. Left) The z-gradient generated by the eddy currents relative to the initial gradient strength applied before the switch-off. Right) Plot for visualizing the decay time constants, by rescaling all initial values to one.

The investigated setups are listed in the following.

Ref : reference GC design
Pr+1 : the radius of the primary layer is increased by 1 mm
Pr−1 : the radius of the primary layer is reduced by 1 mm
Sr+1 : the radius of the secondary layer is increased by 1 mm
Sr−1 : the radius of the secondary layer is reduced by 1 mm
Pz+1 : the primary layer is shifted in axial direction by 1 mm
Sz+1 : the secondary layer is shifted in axial direction by 1 mm
conicS : the secondary layer is conic, changing the radii of all coil windings linearly with distance to $z = 0$ and the most outer windings being varied by ± 1 mm respectively

The last three modifications break the symmetry of the GC regarding $z = 0$, leading to a B_0-offset in the field produced by the GC and also by the eddy currents. A considerable deviation from the 'gradient-like' term has not been observed for these cases. Consequently, they are not considered in figure 3.12, which covers only the eddy current induced gradient-like terms. Since the other variations do not yield any such field contributions, figure 3.15 only describes the B_0-offset behavior of these z-symmetry breaking modifications.

Looking at figure 3.12 one observes that Pr−1 and Sr+1 as well as Pr+1 and Sr−1 show a very similar behavior. Both GC modifications result in the same relative

positions of the primary and secondary conductors, which explains the similar behavior. Only their distance to the cryostat bores is slightly different, leading to a different field amplitude before the switch-off. On the left plot, the gradient-like term amplitudes are given as percentage of the initial gradient, present before switching off the coil. The eddy current gradient-like field of 'Ref' possesses the smallest absolute amplitude, which is reasonable since GCs are optimized to minimize their stray field and changes in the design should lead to an increase.

Also the different signs of the curves can be explained. The field in the FOV is by design dominated by the primary GC layer, so positive values in this graph resemble gradient-like fields with the same orientation, as it is produced by the primary GC layer. Negative values consequently represent the inverted gradient orientation, which is produced by the secondary layer. Otherwise the secondary layer would not have a shielding effect.
If the influence on the stray field from the primary layer is increased compared to the secondary layer (Pr+1 or Sr−1), the gradient orientation of the eddy current fields will reproduce the original GC gradient orientation to a greater extent. Vice versa the eddy current fields will be more inversely orientated, if the influence of the secondary layer on the stray field is increased (Pr−1 or Sr+1). But, this does not explain how a change in the sign over time is possible, since eddy currents of the primary and the secondary layer still would experience the same decay time constants as before.
Considering the right plot of figure 3.12, showing the graphs of the left side individually normalized for their first value, also indicates a strongly irregular decay behavior. The four modified designs decay faster than the reference design and the reference is even increasing in the beginning. To understand this behavior it is necessary to consider the time evolution of the eddy current distribution on the CS. The initial eddy current distributions can be obtained from the stray field distributions (radail and axial). They are plotted for the reference GC, Pr+1 and Pr−1 in figure 3.13.

It is directly obvious, that the differences between the stray fields are marginal and so are the differences in the eddy current distributions directly after the switch-off. Yet, already a significant difference in the field effect of this currents was observable. For example, the inversion of the gradient-like amplitude after the switch off (Pr+1) is a consequence of these minor differences in the stray field. Due to the strong profiled

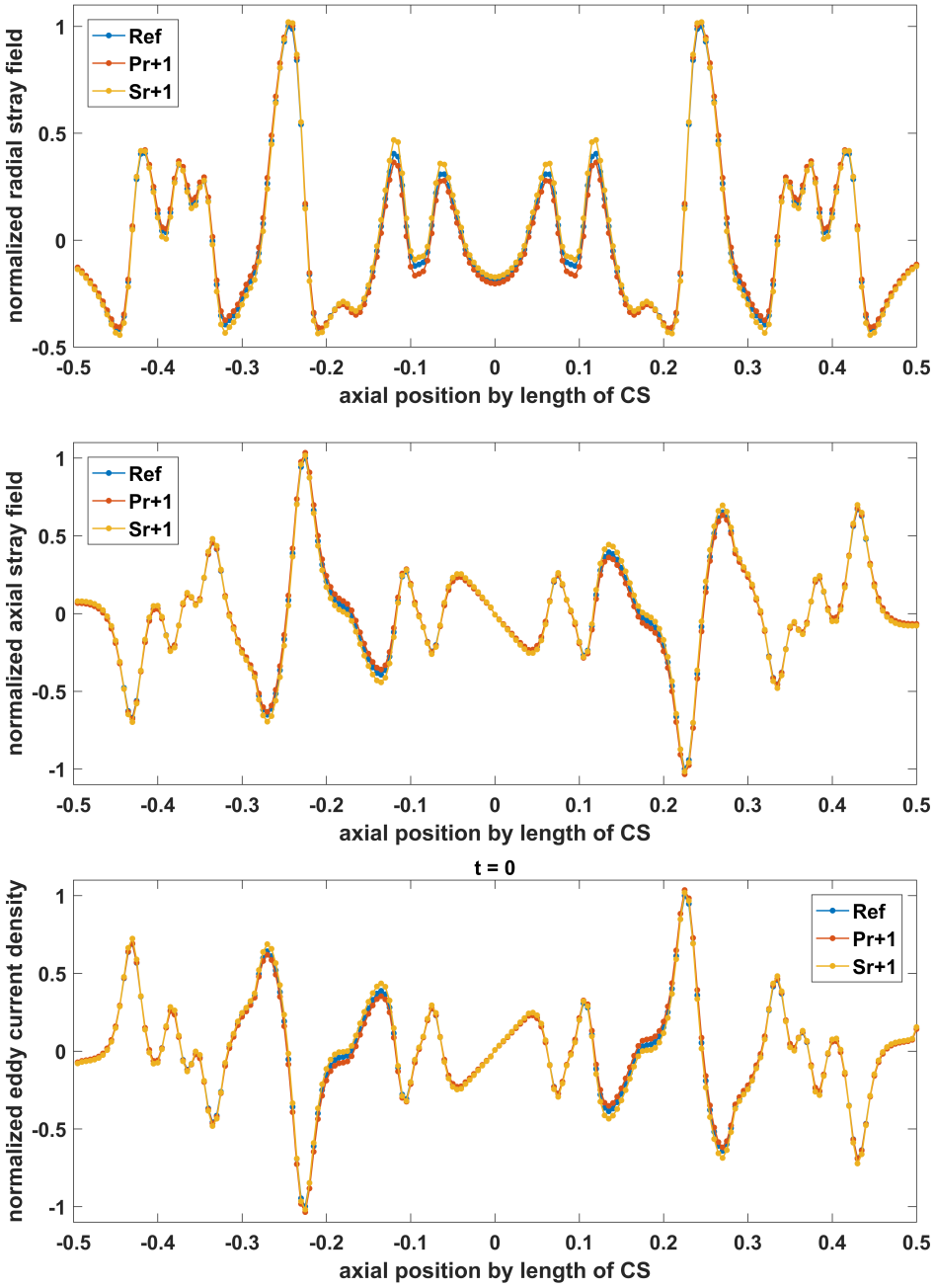

Figure 3.13 – The radial (Top) and axial (Mid) stray field are plotted on the CS radius along the z-direction for three different Z-GC designs. The bottom plot shows the according eddy current distributions at the beginning of the switch-off procedure. For each plot the graphs are normalized to the maximal value of the 'Ref' graph.

distribution (with positive and negative contributions) the fields of the eddy currents cancel each other out to a great extent, so those marginal differences play an important role for the remaining field reaching the FOV.

A side note to mention is that the axial stray field and the eddy current distribution are also highly similar, when evaluated at the CS radius.

$$J_{\varphi_c}(z) \propto -B_z(z) \tag{3.11}$$

This is observable by comparing the middle and bottom plot of figure 3.13. This relation is utilized in section 4.2.2 for the calculation of so-called 'participation factors'.

Figure 3.14 illustrates how the eddy current distributions develop in time. Additionally to the decay, due to the ohmic losses, there is a 'diffusive' process influencing the decay behavior. When considering a coupled inductance between two points A and B, an 'elementary' current decaying at point A, implies a flux change at point B, generating an eddy current trying to prevent that change. With increasing distance between point A and B this influence decreases. Overall, this process leads to a diffusive broadening of the spatial eddy current peaks over time. As a consequence, a positive and a negative eddy current peak decay faster when they are closer together, since they superimpose with elapsing time and cancel each other out. With this thought in mind, it is comprehensible that for example a sign change in the gradient-like field is possible. For $t=0$ the influence of eddy currents generating a positive gradient-like field could be dominant, because they are flowing at a point closer to the FOV, but in total there could be significantly more currents generating a negative gradient-like field. In this case the gradient-like field will be inverted with time as the 'negative' currents will spread and finally cover the 'positive' ones.

Now the three GC design modifications breaking the symmetry along the z- axis are considered more closely. As already mentioned the gradient-like part of these variations is highly similar to the reference design. For Pz+1 and Sz+1 this is apparent, when the gradient is separated into two counter wise oriented ones, originating respectively from the primary or secondary GC layer. Since the gradient field produces a linear variation of B_z along the z-axis (Eq. 2.26), $B_z(z + \Delta z)$ has the same slope as $B_z(z)$. Similarly,

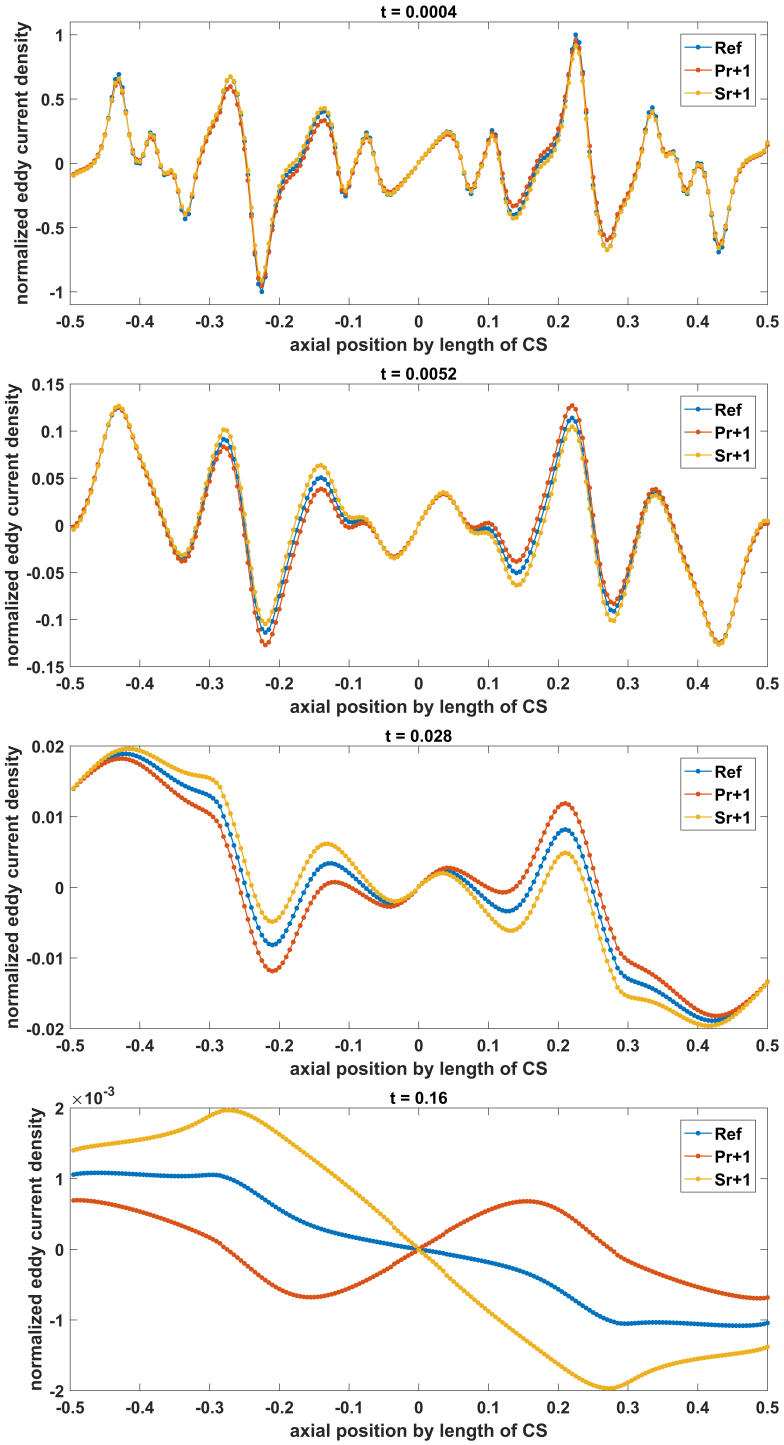

Figure 3.14 – Four plots illustrating the decay of an axial symmetric eddy current distribution on the CS. All graphs are normalized to the maximal value of the reference distribution ('Ref') at $t = 0.0004$, when the switch off procedure is finished.

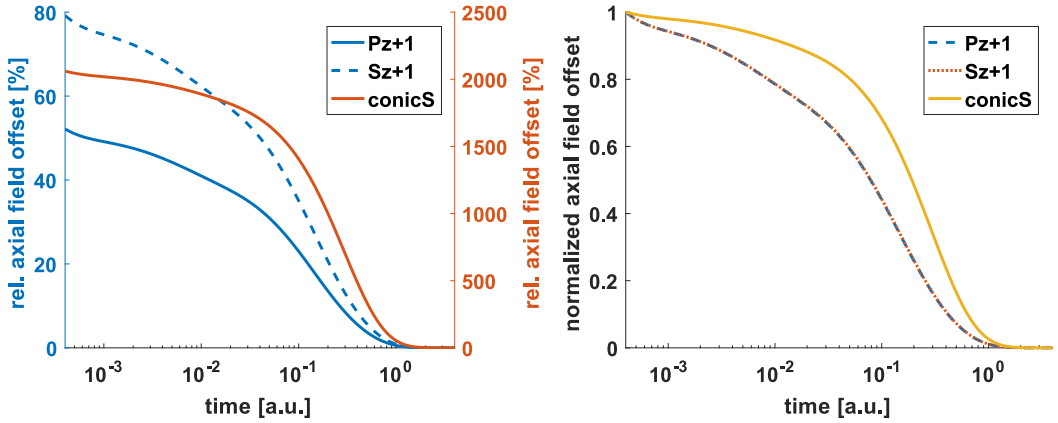

Figure 3.15 – Semi-logarithmic plots of the switch-off behavior produced by GC modifications without z-symmetry. Left) The B_0-offset generated by the eddy currents relative to the initial offset produced by the asymmetric GC before the switch-off. Note that the graph for conicS is plotted on the secondary y axis. Right) Plot for visualizing the decay time constants, by rescaling all initial values to one.

the slope of the superposition of two gradients does not change, if one or both of them are moved, which basically happens when the conductor positions are displaced by a constant axial value. The spatial shifting of the gradient does, however, introduce a constant offset, as seen in figure 3.15. With the setup of the GC being z-symmetric, the axial displacement of one layer in positive or negative direction generates a similar stray field. Moving one layer in positive z-direction, but looking at the field with an inverted z-axis provides the same field as a movement of this layer in negative z direction.
Moreover, when taking a relative perspective, it is also irrelevant for the stray field distribution, if the secondary or primary layer is displaced. Thus, considering all symmetries Pz+1 and Sz+1 produce an identical stray field distribution, so that after a normalization the field terms must also decay identically over time.

The conicS variant represents a GC, which possesses a linear increasing radius with the axial position for the secondary layer conductors. For $z = 0$ the displacement is zero, so that for negative z-positions the radius is reduced and for positive z-positions the radius is increased. Due to the anti-symmetry of the relatively small radial displacement concerning $z = 0$ and the generated gradient-like term of the field is basically unchanged.

The simulations in this section demonstrate how sensitive the field in the FOV is to minor variations of the eddy current distribution on the CS. Consequently, it is very unlikely that a real system with construction tolerances will show the identical behavior as the idealized simulations. On the one hand, a precise reproduction of fields in the FOV can not be expected from the simulation without knowledge of the exact conductor positions of the individual coil. But it implies on the other hand, that effects observable over many systems must also be reproducible with the simulations, as they have to be insensitive to such tolerances. Therewith, the impact of mesh irregularities or asymmetries in the simulation should not prevent predictive and relative statements.

3.2.3 Cryostat mesh resolution

For three-dimensional simulations, considerations regarding mesh optimization become more important. Compared to the 2D axial symmetric case, where the mesh has been willingly over-specified, due to the absence of long computation times, 3D calculations also demand to keep the number of elements reasonably small. This has to be done without reducing the accuracy of the approximated results significantly. Since such an optimization would be very time consuming for an entire 3D MR model, a simplified 2D setup is analyzed.

For the transport mechanism of the magnetic field through a conductive material, it is important to model the skin depth of the eddy currents accurately. Therefore, the resolution of FE-mesh must be capable of properly approximating the skin depth. This capability depends on the order and the number of elements used to mesh the thickness of the material. To test how large this number has to be for first order elements a simulation setup with one conductor loop enclosed by a conductive hollow cylinder is modeled in 2D. The measure for comparison is the magnetic field at a point directly outside of the cylinder. For the study the number of elements n_d along the thickness was varied between 1 and 11 with two different conductivities for a $5\,\mathrm{mm}$ thick cylinder structure. For more than two elements, the thickness of the elements has been varied. Towards the center of the material the element thickness has been increased, to achieve an efficient spatial sampling of the exponential eddy current decay. The conductivities were chosen similar to the materials of the CS and the OVC or the HeV respectively. As reference, simulations with $n_d = 11$ elements have been used. The investigation

was performed with a frequency of 3000 Hz. This is the upper frequency limit analyzed with the ECL simulations, covering the worst case scenario, with the highest demands concerning the skin depth resolution. The evaluation was done over one periodic cycle after a steady state oscillation has been reached.

From the left plots in figure 3.16 it can be concluded that using less than 7 elements yields erroneous fields for CS material concerning the amplitude and more importantly also concerning the phase of the oscillation. The time window, shown in all plots in figure 3.16, is identical, illustrating that a different phase shift is effectuated by the transmission through the respective materials. Phase differences are critical, because it can cause a qualitatively different system behavior, as resonances have a strict phase relationship between excitation and consequence. Moreover, a phase shift spoils the way the fields interfere. In contrast, the difference in amplitude should prominently have a quantitative influence on the results. The remaining amplitude difference with $n_d = 7$ is, of minor importance. The error is expected to be less for magnetic fields with lower frequencies, possessing larger skin depths.

For the less conductive material even less elements are necessary to simulate a converged behavior. The results of the transmitted fields are shown on the right plots of figure 3.16. With the reduced connectivity the skin depth of the material increases and less sample points are needed for an acceptable linear interpolation. Consequently, the resolution along the thickness was chosen to be 3 for the OVC and HeV material.

It is possible to find the correct choice for the in plane resolution of the vessels by considering modal analysis results of the components. For up to 3000 Hz the inner bore modes of the investigated systems show up to 20 extrema in axial direction. To cover these modes with a high enough resolution of ten elements per extrema, the inner bores where subdivided in approximately 200 elements, yielding element lengths between 5 mm and 7 mm. In circumferential direction about 18 extrema are expected, resulting in a 2° angular resolution.

For a detailed explanation of the errors introduced by the FE discretization it is referred to [48].

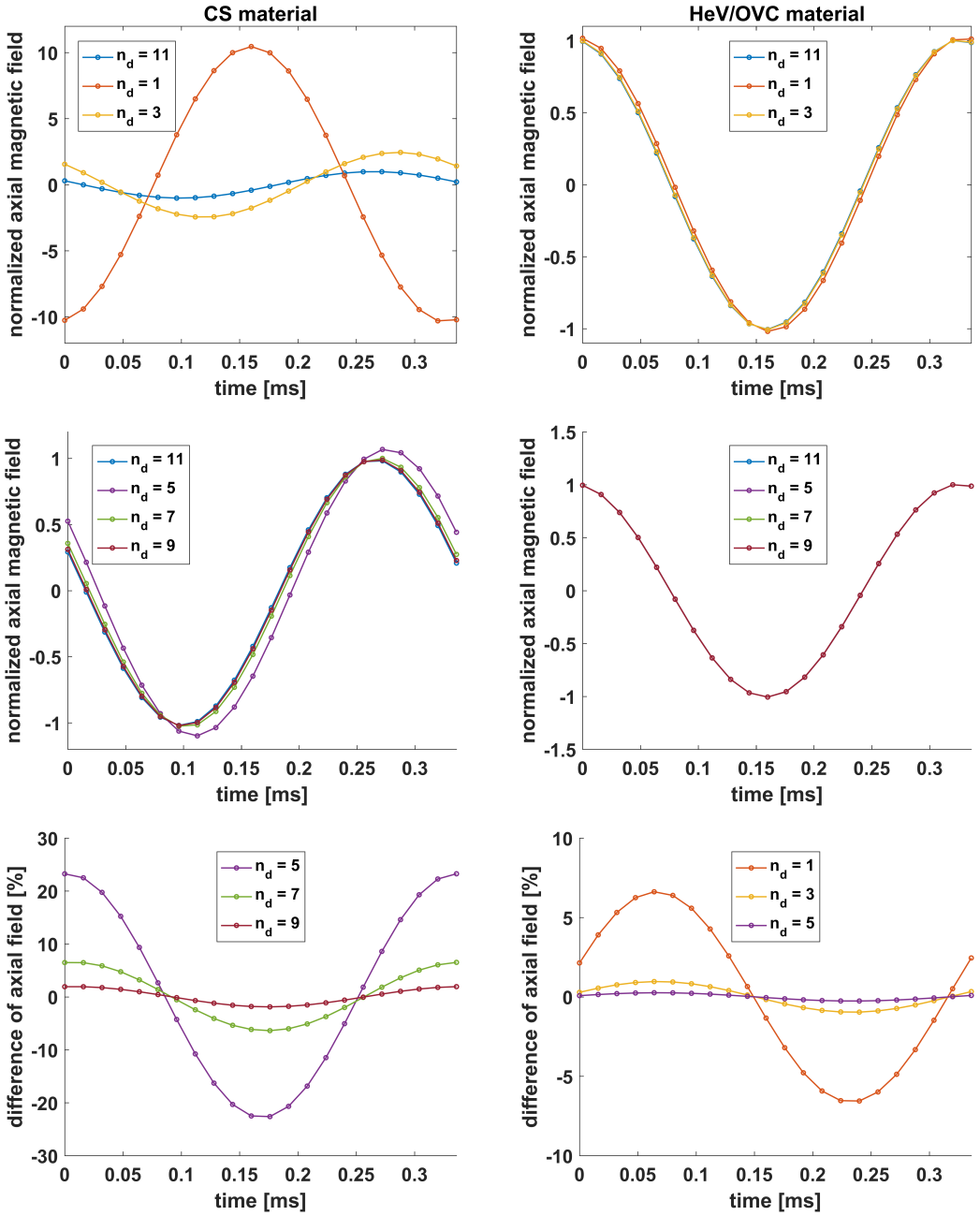

Figure 3.16 – Six plots illustrating how the magnetic field transmitted through a conductive layer is dependent on the number of elements used to discretize the layer. The graphs on the left show the behavior for material used for CS and the right graphs for HeV and OVC material. The curves in the top and middle plots are normalized to the amplitudes of the $n_d = 11$ calculations and the bottom plots display the difference of selected setups as ratio to these amplitudes, respectively.

3.2.4 Symmetry considerations

Besides the optimization in terms of element usage, the consideration of the possible symmetries of the system helps to reduce the computational effort. Similar as for the Z-gradient, the loops of the X- and Y-gradients are assumed to be individually driven by current, so that there are no connections between them (see Fig. 3.17). Doing so, the transversal gradient coil geometries are symmetric to each cartesian coordinate plane. Thus, it is possible to reduce the model to an octant, when only GC symmetries need to be taken into account.

When the field of the main coils needs to be calculated simultaneously, less simplification by means of symmetry are possible. The current direction for a Y-GC needs to be inverted for the x-z-plane symmetry in contrast to the current in the main coils. Analogously the same argument holds for an X-GC considering the y-z-plane.

Table 3.1 summarizes the boundary conditions, which need to be applied on the coordinate planes for the different coil types. The boundary conditions for the mechanical movements of the cryostat are defined by the combination of the magnetic boundary conditions of $\boldsymbol{B_0}$ and the gradient field, since they define the symmetry of the Lorentz forces which excite the cryostat movement (given by Eq. 4.18).

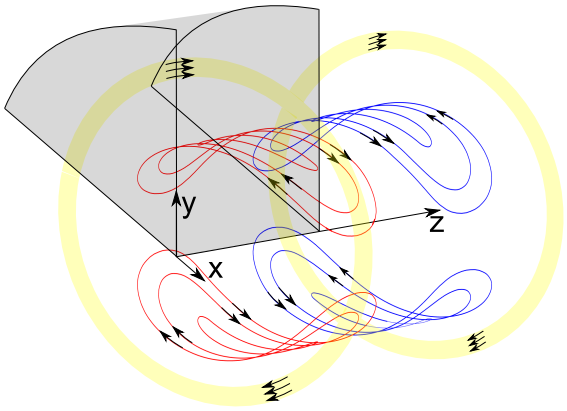

Figure 3.17 – Schematic illustration of a Y-GC. The main magnet coils are represented by the yellow circles. Arrows indicate the direction of current flowing in the conductors. Modeling a Y-GC and main coils demands a 3D model of at least a quarter of the system. For the matrix coupled case (see Sec. 2.6.3) or static simulations a further reduction to an octant model (shaded region) is possible.

Table 3.1 – Boundary conditions considering the magnetic flux and the mechanical displacement on the three coordinate system planes for the three gradient types and the main magnet

Boundary plane	X-gradient	Y-gradient	Z-gradient	$\boldsymbol{B_0}$
magnetic flux				
x-y-plane	normal	normal	parallel	normal
x-z-plane	parallel	normal	parallel	parallel
y-z-plane	normal	parallel	parallel	parallel
mechanic fixation				
x-y-plane	z	z	x , y	-
x-z-plane	y	x , z	y	-
y-z-plane	y , z	x	x	-

3.2.5 3D modeling of transversal magnetic field gradient coils

Having set the basic mesh and symmetry properties needed for a reliable simulation in 3D, the peculiarities of the incorporation of the transversal GC conductors are discussed in the following.
In contrast to the Z-GC the X- and Y-GCs do not share the axial symmetry of the main coils and cryostat. The GC geometry has to be modeled with finite elements, to be able to make use of the speed up offered by the linearization of the harmonic matrix solution. For the transient 3D simulations, described in section 4.2.4, the Biôt-Savart formulation is employed and allows entirely rotated meshes.

For the ECL computations the FE-mesh can not be constructed entirely by a rotation operation of the 2D mesh as it was possible for the 3D Z-GC in section 3.2.1. To maintain the correspondence of the axial symmetry of the cryostat and main coils, it is advisable to employ the mesh rotation method for these components. The air region surrounding a transversal GC has to be freely meshed to connect the GC model with the rotated mesh.

To provide a successful and qualitatively good meshing process for the transversal GCs, some modifications of the gradient coil conductors have been necessary. First, the conductors have been subdivided into short straight segments to approximate

the wire pattern, enabling a regular hexahedron mesh for the wires. For an efficient approximation of the spatial stray field distribution it is recommended to use a variable segment size for the conductors which adapts to the curvature of the conductor path. This reduces the number of elements used for straight conductor parts, while curved sections are modeled with more elements. Employing large elements where conductors are strongly bent leads to sharp kinks. In addition to the resulting inaccurate model of the geometry, this may also lead to deformed elements with disadvantageous aspect ratios, corrupting the solution.

Since the conductors are often arranged in a spatially dense way, the width and height of the conductors have been furthermore reduced to avoid tiny gaps due to the small distances between the gradient coil wires as well as towards the cryostat. This simplifies the meshing procedure, as it gives more space to the mesher to smoothly adapt elements to the surrounding. A significant loss of accuracy is not expected, since the replacement of FE conductors by Biôt-Savart filaments, not possessing any cross-section, still shows a reasonable agreement in the field computation (see App. A.4).

3.3 Reduction of eddy current losses induced by a transversal field gradient

Similar to the Z-gradient investigations, this section analyzes the ECL performance of a prototype coil for generating a transversal magnetic field gradient (in this case a Y-gradient) via simulations. The quality and predictive power of the calculations are assessed and measures for the reduction of the ECL are concluded. The predictions are confirmed with measurements performed on a modified prototype setup.

Since the characteristics of the ECL spectrum appear to change significantly above and below $1500\,\mathrm{Hz}$, the considerations are subdivided into two frequency regimes. In the high frequency range above $1500\,\mathrm{Hz}$ the inner bores of the cryostat shields dominate the processes. Below $1500\,\mathrm{Hz}$ the other parts of the cryostat also contribute to the behavior. Both simulations utilized the linearized solution algorithm and an identical FE-model.

In the process of these investigations, mismatches between the simulation results are observed and possible reasons are discussed. Despite these discrepancies the simulations provide successful instructions to improve the system design.

3.3.1 Measurement and simulation results

The left plot of figure 3.18 illustrates the measured ECL for the investigated Y-GC in a 1.5 T magnet. The values are again normalized to the maximum value of the reference ECL spectrum measured for the Z-GC (see Fig. 3.2). Consequently, the entire high frequency range of the Y-prototype is generating significantly more ECL than the aspired reference. Regarding the low frequency range, the focus is set upon the peak at 240 Hz and the equally high values around 1000 Hz. Although the ECL values are smaller in the low frequency range than in the high frequency range, they can become relevant for the cooling demands of the system. As mentioned in section 2.2.4 the utilized frequencies for fast imaging usually remain below 1300 Hz, so that these frequencies are possibly directly driven by the GC fields in clinical usage. The high frequency ECL is in contrast important because of the excitation of higher (n-th order) harmonics with non-sinusoidal currents, as was shown in section 3.1.1.
EPI often uses trapezoidal read-out gradient waveforms, which are in the worst case assumable as periodic boxcar functions with an infinitesimally steep slope. Since, the clinical usage of EPI read-out frequencies lies below 1500 Hz (see Sec. 2.2.4), ECL above 1500 Hz mainly contribute as 3rd harmonics in this case. Contributions by 5th or higher harmonics can typically be neglected due to the $(1/n)^2$ dependency. This participation of higher harmonic excitations adapts both frequency ranges to similar importance for the ECL considerations, although the pure high frequency values are typically on a higher level.

Evaluating the simulated ECL for the high frequency range in comparison to the measured spectrum (Fig. 3.18 left), shows that the simulation is overall underestimating the generated heat load about a factor of roughly 2. Yet, taking the uncertainty regarding the frequency (due to the sweeping measurement method) into account, the occurring resonance frequencies agree very well. In addition, the relations between the resonance amplitudes are also described correctly. Overall, the simulation is convincingly reproducing the measurement despite the underestimated absolute amplitude. Relative

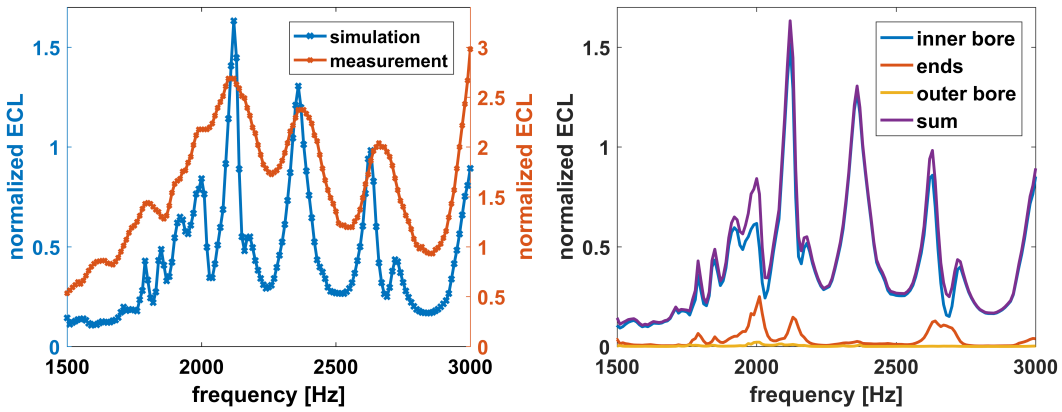

Figure 3.18 – Left: Measurement and simulation for the Y-GC prototype in the high frequency regime. The measurement values are plotted relating to the secondary y-axis. Right: The simulated ECL values of the different HeV components plotted individually.

statements derived from the simulation results promise to give reasonable estimations concerning the real system.

An explanation for the amplitude differences could be the construction tolerances of the more complex GC-Magnet system, allowing more modes to be excited than in the idealized perfect symmetric simulation. The simulation results are scaled via a factor that was derived by the axial symmetric Z-gradient simulations, which possesses less degrees of freedom than the Y-gradient simulation. These additional degrees of freedom increase the mode density (number of modes per frequency interval) significantly. This potentially offers more excitable modes and could also cause stronger mode coupling, leading to more broadband vibrations. Another explanation for the differences could be that the simplifications made by the linearization have a greater influence for transversal coils.

The right plot of figure 3.18 introduces a new illustration scheme, separating the simulated ECL according to their location. Blue indicates the contribution to the ECL originating from the inner bore, red from the ends and yellow from the outer bore of the HeV hollow cylinder. The sum of all the contributions is drawn in purple and equals the simulation values on the left plot. It is obvious that the simulation states that the ECL is

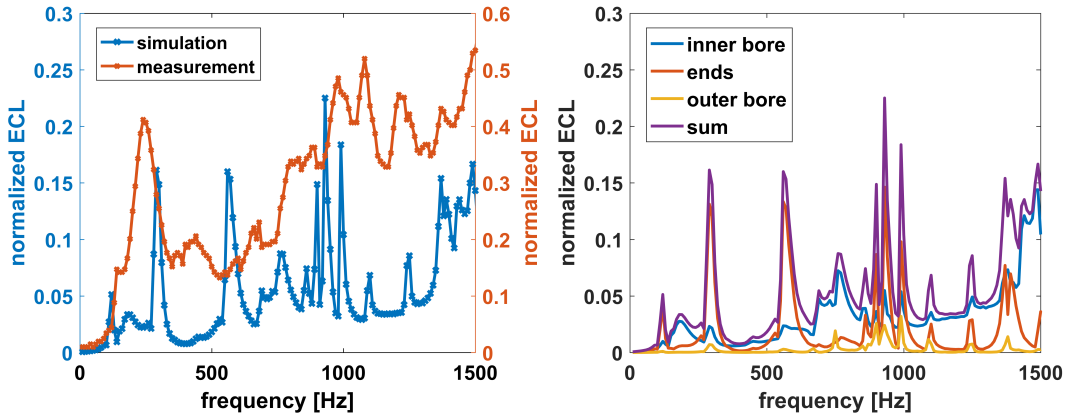

Figure 3.19 – Left: Measurement and simulation for the Y-GC prototype in the low frequency regime. The measurement values are plotted relating to the secondary y-axis. Right: The simulated ECL values of the different HeV components plotted individually.

dominantly produced on the inner bore, while the ends contribute slightly and the outer bore is hardly noticeable. This information is of high value, because it already indicates that the main magnetomechanical interactions needing consideration take place on the inner bores within that frequency range.

For the low frequency range the situation is different. As the left plot in figure 3.19 shows, there is hardly any agreement visible between the measurement and the simulation. Neither the frequencies nor the amplitudes of the resonances are reproduced adequately, even if the additional factor 2 deduced from the high frequency range is multiplied to the values. No clear assignment of peaks between measurement and simulation is possible. There appears to be at least one essential difference in the description between the two frequency regimes. One candidate for such a difference is illustrated in the right plot of figure 3.19, which separates the contribution of the HeV parts to the overall ECL. In contrast to the high frequency range, here the ends of the hollow cylinder play a significant role.

This argument is reasonable, since the ends of the cryostat have not been modeled in great detail within the simulation setup. As presented in figure 3.4 the ends are assumed to be flat and seamlessly connected to the inner bore. Both of these assumptions do

not reflect reality correctly. The ends of the three shields possess different inclinations, bends and surface profiles, modifying the mechanical resonances. Thus, a mismatch between measurement and simulation involving the cryostat ends in the spectrum is comprehensible. Simple attempts of including bends in the FE model were investigated and showed considerable influence on the spectrum, but could not improve the agreement sufficiently to justify the additional complexity in the construction of the model.

Regarding the above mentioned connection of the inner bore and the ends at the corner, a realistic description of the joint is even more complex and lies beyond the scope of the presented work. The properties of this connection, strongly modify the mechanical boundary conditions for both shield components (ends and inner bore) and thereby essentially influence the eigenfrequencies. Moreover, this link acts like a mechanical filter for the propagation of movement and energy between the components, affecting the 'communication' of the components and the way resonances can occur. Further development concerning the modeling approach for this corner is continuously undertaken to improve the solution accuracy.

In total, the comparison of simulation and measurement shows that the simulation of transversal coils produces reliable results in the high frequency regime, where the interactions on the inner bore appear to dominate the ECL generation. The following section will show, that relative predictions for design improvements utilizing the calculation are feasible, although the absolute values of the resonance amplitudes are estimated incorrectly. For the low frequency range the predictive power of the used models is currently strongly limited. Yet, the clearly higher accessibility of simulation data compared to the real measurement data allows the identification of system properties, which can be used to reduce the ECL.

3.3.2 Applied measures for eddy current loss reduction

The Y-GC prototype presented in the section above produces a relatively high ECL over the entire high frequency range (Fig. 3.18). In section 3.1.6 the ECL for a Z-gradient could be reduced by testing several wire pattern modifications of the coil. Due to the higher complexity of coil geometries, that generate transversal linear field gradients,

the optimization of the wire pattern is more difficult for the Y-gradient discussed here. The available degrees of freedom for repositioning the conductors is limited more strongly and these restricted possibilities for modifications in the wire pattern were not expected to globally reduce the ECL for the entire frequency range.
Instead of optimizing the GC stray field in terms of ECL, the energy transported to the HeV was reduced by modifying the cryostat. The thickness of the OVC inner bore was increased about $1\,\mathrm{mm}$. Supposing the OVC mainly acts as absorbing filter in the magnetomechanical process, this measure should lead to a reduction of ECL on the HeV over the entire frequency range. Due to the decreasing skin depth for increasing frequencies the thickened OVC should especially affect the ECL in the high frequency range.

As the construction of a new magnet system with a modified cryostat is very time consuming, this mitigation was tested beforehand. The development process of MRI systems includes a strict adjustment of the properties and characteristics of the GC and MR magnet system. Only for ECL test purposes the prototype GC was installed in a commercially available magnet system, possessing a comparable geometric setup as the prototype cryostat besides a $1\,\mathrm{mm}$ thicker OVC inner bore. This exceptional combination will be referred to as 'hybrid system' in the following.
The high frequency ECL measured in this hybrid system together with the according simulation is presented in the left plot of figure 3.20. Due to the different magnet geometry the eigenfrequencies of the resonances change. Still, the clear broadband reduction of the ECL in comparison to the GC prototype in the initial magnet (Fig. 3.18) indicates the positive influence of the thickened OVC inner bore. The peak values are diminished to less than half of their former values, bringing them down to same level as the reference spectrum (Fig. 3.2).
The performance of the simulation is of similar accuracy as in the first 3D example, reproducing the qualitatively behavior with good agreement. Also a comparable amplitude difference between simulation and measurement of roughly a factor 2 can be observed.

The assumption of the mainly absorbing character of the OVC for the magnetomechanical transport mechanism is observed to be reasonable. This is

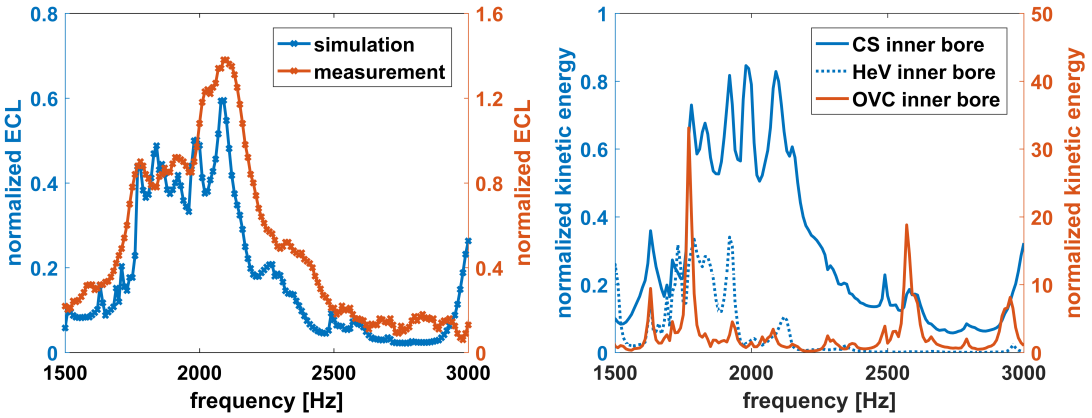

Figure 3.20 – Left: Measurement and simulation results for ECL in the high frequency range for the hybrid system. The measurement values are plotted relating to the right axis. Right: The simulated kinetic energies of the shield inner bores corresponding to the ECL simulation on the left.

confirmed in the kinetic energies of the three cryostat shields. In the right plot of figure 3.20 the corresponding kinetic energy spectra for the hybrid system are shown (OVC plotted on the right axis). The values are normalized to the maximal kinetic energy of the CS. There occur strong couplings, for example at $1750\,\mathrm{Hz}$, where all shields show a kinetic energy peak and it is unclear which component is driving the movement. But comparing the spectrum of the CS with the ECL values on the right shows a high correlation, indicating that the movement of the CS is primarily responsible for the ECL on the HeV. Thus, the secondary eddy currents (compare Fig. 2.9) generated on the CS emit fields that are converted to ECL on the HeV.

The movements of the HeV and the OVC play a minor role. For the HeV this can be explained by its higher density and smaller kinetic energy. This leads to a relatively small velocity, which is the trigger for the generation of secondary eddy currents. In combination with the poor conductivity, this smaller velocity makes the CS, having less density and significantly higher conductivity, the dominant component in the process. Due to the high kinetic energy of the OVC it can, however, not be excluded, that significant secondary eddy currents are generated there. But like the GC stray field, these secondary fields would practically be entirely absorbed by the CS, generating additional movement (consider peaks at $2600\,\mathrm{Hz}$ in the right plot). It has to be noted, that all these

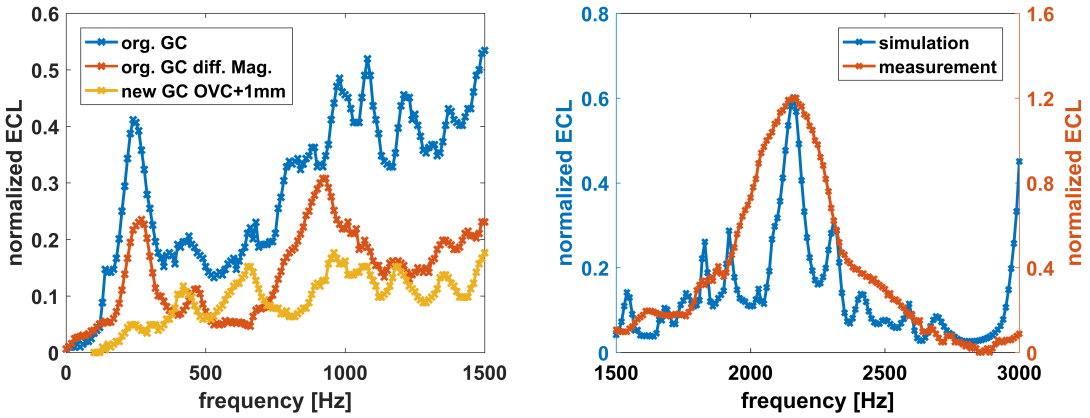

Figure 3.21 – Left: Measurement results in the low frequency range for the three different GC-magnet combinations. Right: Measurement and simulation results for the high frequency ECL of the redesigned Y-GC in a magnet with a thicker OVC inner bore.

conclusions are drawn for a 1.5 T system. For higher field strengths different behaviors might be observed, since the coupling between the shields should be increased.

The low frequency range of the ECL spectra shall be discussed at this point. The left plot in figure 3.21 compares the measurement results for the initial prototype in the initial magnet (blue) and the same GC in the different ('hybrid') magnet with thicker OVC inner bore (red). Apparently the combination of increased OVC thickness and different magnet geometry lead to a reduction of ECL. It is, however, also observable that the resonances around 250 Hz and 1000 Hz are still prominent. It could have been the case, that the ECL reduction seen here was mainly due to the different resonances and not due to the thickened OVC. Hence, additional measures were applied to ensure a successful mitigation of ECL in the low frequency range.

The simulations for the low frequency range, propose a strong contribution of resonances at the ends of the shields. Transferring the conclusion from the high frequency range, stating that the CS movement is dominantly causing the ECL, keeping the stray field contributions on the CS away from the ends should reduce the occurring movement of the cryostat ends.

Consequently, the GC wire pattern was modified to avoid strong stray field extrema and thus primary eddy currents near the ends. The low frequency result of this adapted GC design combined with the original magnet, possessing a thicker OVC bore, is presented in yellow in the left plot of figure 3.21. It shows that the two measures for the reduction of the ECL were successful for the frequencies below 1500 Hz.

The right graph of figure 3.21 shows the achieved reduction for the high frequency region with the modified GC in the initial magnet with thicker OVC. Comparable to the hybrid system the maximal ECL values were reduced about a similar factor. Additionally, the resonances above 2300 Hz (see Fig. 3.18) also diminished with the redesigned of the GC wire pattern. Both mitigation effects are described by the simulation.

In this section it has been demonstrated that the 3D FE framework is capable of making relative statements in the frequency range above 1500 Hz. Both influences, the GC stray field modification, as well as changes in the magnet geometries, have been correctly estimated. For the low frequency regime the predictive power of the simulation models is still strongly limited, probably due to erroneous boundary conditions at the connection of the inner bores and the ends. Yet, the identification of the contributing components via the simulation was helpful to achieve the reduction of the ECL.
Moreover, the insight into the system, provided by the simulations, revealed the dominant role the CS plays concerning magnetomechanical interactions for 1.5 T MRI systems.

The following section will utilize the conclusions obtained from the presented ECL simulations to reduce EPI ghosting artifacts associated with mechanical vibrations of the cryostat.

4 Investigations on EPI ghosting due to cryostat vibrations

This chapter will establish a transition from ECL considerations to actual image artifacts in EPI. The insights gathered into the magnetomechanical interactions, will be applied to derive means for mitigating EPI ghosting artifacts. A hypothesis will be introduced on how EPI ghosting is generated by secondary eddy currents. It describes which movements (radial, axial or circumferential) are expected to be dominantly responsible for secondary eddy currents and what properties (time behavior and phasing) the according secondary field should have.
The analysis of the generated results for the ECL investigations in the previous chapter identified the CS as major component for strong magnetomechanical interactions. This information will be used in the subsequent sections to derive an approach to reduce related magnetomechanically induced ghosting. Therefore mechanical modes of the cryostat are derived, which are potentially responsible for a concrete ghosting artifact. A reduction of this artifact is achieved by utilizing a modified GC prototype which excites these mechanical modes less. In addition, a three dimensional transient simulation applying the iterative algorithm (Sec. 2.6.2) is presented, approving the mitigation the redesigned GC prototype has on secondary eddy current fields in the FOV.

Finally, the problem will be addressed whether or not the modifications, leading to a reduction of the ghosting artifact, are directly connected to the secondary eddy currents. The experimental prove that fields, generated by magnetomechanical interactions, actually are detectable in the FOV is achieved with a combination of MR measurements and direct field measurements using a pickup coil. These measurements allow to reconstruct the shape of mechanical cryostat vibrations to a certain extent, clearly indicating the connection of mechanical movement and emitted magnetic fields.

4.1 Properties of magnetomechanical EPI ghosting

4.1.1 Analytical investigation of resonant field disturbances considering their spatial distribution

As described in section 2.2.5 one of the motivations for investigating the magnetomechanical coupled processes in MRI systems is to improve the understanding of the origins of EPI ghosting. Therefore, it is necessary to establish a connection between the eddy currents generated by mechanical vibrations and the field disturbances producing ghosting. The calculation presented with the equations 2.32 to 2.35 already predicts the appearance of ghosting due to a simplified approach of a multiplicative signal variation, occurring every other k-space line. This approach is now generalized and adapted to a more realistic scenario.

Let x be the direction of the read-out gradient using a trapezoidal encoding scheme with the frequency ω_{EPI}. The phase encoding direction is set as the y direction. In the undisturbed case, the MR signal of a body $\rho(\boldsymbol{r})$ is given by equation 2.27

$$S(t') = \iiint \rho(\boldsymbol{r})\mathsf{exp}(i\Phi_G(\boldsymbol{r}, t'))\, dx\, dy\, dz$$

where relaxation processes as described by the Bloch equations are neglected for clarity. Consider the presence of secondary eddy currents $\boldsymbol{I_S}$ within the MRI cryostat (see Sec. 2.4), which possess a time dependent spatial distribution. This spatial distribution can directly be translated into a distinct magnetic field distribution in the FOV $\boldsymbol{B_e}(r,t) = B_e(\boldsymbol{r},t)\boldsymbol{e_z}$ (only the z-component is relevant here). Similar to the gradient phase introduced in equation 2.21, this magnetic field leads to an additional phase

$$\Phi_e(\boldsymbol{r}, t') = -\gamma \int_0^{t'} B_e(\boldsymbol{r}, t)dt \tag{4.1}$$

Here, again $t = 0$ is determined by the timing of the EPI RF excitation. Thus, the disturbed signal reads as

$$S_e(t') = \iiint \rho(\boldsymbol{r})\mathsf{exp}(i\Phi_G(\boldsymbol{r}, t')) \cdot \mathsf{exp}(i\Phi_e(\boldsymbol{r}, t'))\, dx\, dy\, dz \tag{4.2}$$

To calculate how the disturbing field $B_e(\boldsymbol{r}, t)$ would manipulate a given EPI image,

$S(t')$ needs to be joint with the additional phase accumulated through the disturbance. So equation 4.2 must be computed for every time point the signal was sampled and then ascribed to a k-space point according to the EPI k-space trajectory, which is implied in the time-dependency of $\Phi_G(\boldsymbol{r}, t')$. The Fourier transform of the modified k-space data yields the disturbed image.

This method allows to calculate how the MR image is manipulated by a given time and space dependent disturbance field $B_e(\boldsymbol{r}, t)$. If mechanical vibrations are the main cause, the strongest disturbances are expected when the mechanical eigenfrequencies and the EPI read-out are resonant. Hence, for the further considerations the time dependency is supposed to be harmonic with the EPI read-out frequency.

$$B_e(\boldsymbol{r}, t) = B_e(\boldsymbol{r}) \sin(\omega_{\mathsf{EPI}}\, t + \vartheta) \tag{4.3}$$

ϑ thereby defines the temporal phase shift between the read-out gradient and the occurring field disturbance.

Any $B_e(\boldsymbol{r})$ can be expressed as a superposition of orthogonal spatial functions. For the 2D pictures considered in the following, polynomials in x and y direction were chosen, with $x{=}y{=}0$ describing the center of the picture.

$$B_e(\boldsymbol{r}) = B_e \sum_{n=0} c_{x_n} x^n \boldsymbol{e_x} + c_{y_n} y^n \boldsymbol{e_y} \tag{4.4}$$

By analyzing the influence of simple polynomial terms, the effect of more complex distributions can be estimated. Three examples will be further investigated here. In the first one, all summands for $n{\neq}0$ are set to zero, describing a constant offset, which is changing B_0 for the whole 2D plane (relevant for Fig. 4.1 and 4.15 `II-IV`).

$$B_e(\boldsymbol{r}) = B_e\, c \quad | \quad c \neq 0 \tag{4.5}$$

In the second polynomnal, all prefactors besides c_{x_1} are zero, yielding a perfect x-gradient (compare Fig. 4.5) described by

$$B_e(\boldsymbol{r}) = B_e\, c_{x_1}\, x \quad | \quad c_{x_1} \neq 0 \tag{4.6}$$

The third example is a combination of the two polynomials above (Fig. 4.6 and 4.15 I) reading as

$$B_e(\boldsymbol{r}) = B_e(\, c_{x_1}\, x + c) \quad | \quad c, c_{x_1} \neq 0 \tag{4.7}$$

4.1.2 Homogeneous field disturbance at resonance

Figure 4.1 presents the influence of a change of ϑ (Eq. 4.3) using the described reconstruction method and a B_0 like disturbance (Eq. 4.5), when applied to an image of a sphere. If ϑ is 0 the maximal amount of accumulated phase Φ_e coincides with the sampling of the outer regions of the k-space lines due to the integral in equation 4.1. Consequently, the resulting ghost mainly shows the contours of the sphere, since the outer k-space codes spatial waves with short periodicity. $\vartheta = \pm\pi/2$ in contrast leads to a so-called 'solid' ghost, because the maximal values of Φ_e occur at the k-line centers. This leads to the question, which phase relationship is expected between the read-out gradient fields and secondary eddy current fields, induced by resonant vibrations.
The primary eddy currents $\boldsymbol{I_P}$ are a consequence of the voltage induced by the changes of the magnetic field $\boldsymbol{B_G}$ caused by the gradient coil (Faraday's law)

$$U_P \propto \frac{dB_G}{dt} \tag{4.8}$$

Due to the highly conductive materials, the decay time constants of eddy currents are longer than the periodicity of the oscillations ($< 5\,\text{ms}$) at the resonance frequencies. Hence, the eddy current behavior is dominated by the inductance L of the eddy current path, yielding

$$U_P = -L\frac{dI_P(t)}{dt} \tag{4.9}$$

which results in a dependency of the eddy currents on B_G

$$I_P(t) \propto \int \frac{dB_G(t)}{dt} dt \tag{4.10}$$

Now the main Lorentz forces $\boldsymbol{F_P}$ caused by these eddy currents are given as vector product with the dominant main magnetic field $\boldsymbol{F_P} \propto \boldsymbol{I_P} \times \boldsymbol{B_0}$. From resonance theory it is known, that in the case of a resonance the exciting force and the velocity of the movement $\dot{\boldsymbol{u}}$ are in phase [49].

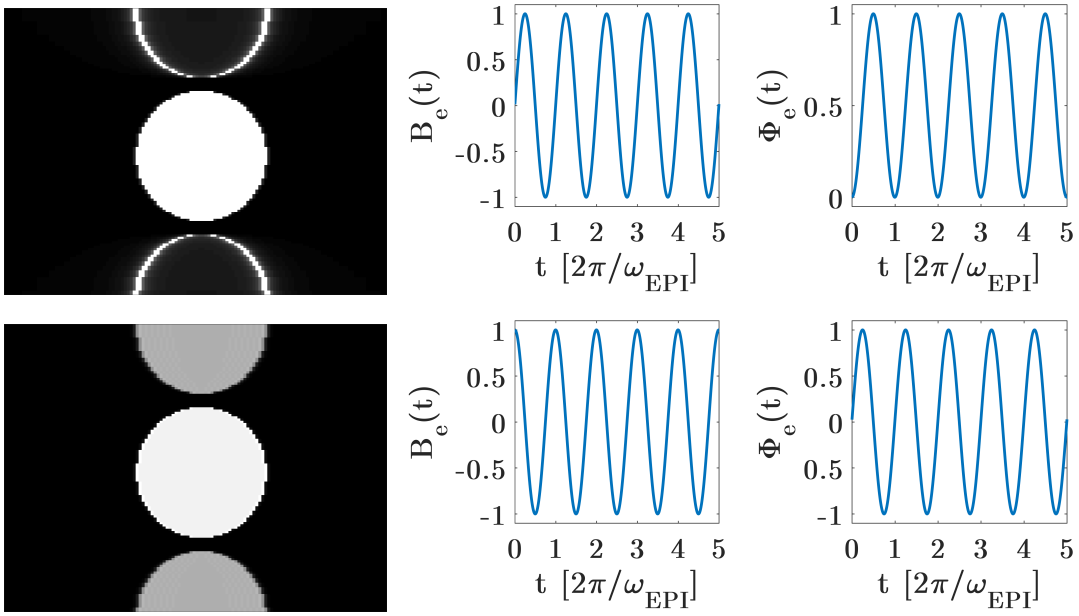

Figure 4.1 – Illustration of the simulated ghosting artifacts for a homogeneous background disturbance (Eq. 4.5) with different phase relationships between the read out gradient and the occurring field disturbance. Also the resulting additional phase of the magnetization is plotted. The top row displays the effect of $\vartheta = 0$, an in-phase disturbance generating so-called 'contour' ghosting, and the bottom row of $\vartheta = \pi/2$, generating 'solid' ghosting.

Applying Faraday's law for the movement provoked by the primary eddy currents is more complex, since the movement can change the penetrated area as well as the magnetic field seen by this area. Furthermore, $\boldsymbol{B_0}$ can not be assumed to be homogeneous and directed purely in z-direction at the position of the cryostat. In the cylindrical coordinate system (see App. A.2) $\boldsymbol{B_0}$ also possesses a radial component and $d\boldsymbol{B_0}/dr_c, d\boldsymbol{B_0}/dz \neq 0$. Due to the cylindric symmetry $\boldsymbol{B_0}\,\boldsymbol{e}_{\varphi_c}$ and $d\boldsymbol{B_0}/d\varphi_c$ remain 0, so any potential cryostat movement in φ_c-direction can be ignored.

This leaves four potential processes (or combinations of them) for changes in the magnetic flux related to $\boldsymbol{B_0}$. Local displacements in r_c or z can either lead to local changes in the ratio of surface exposed to $\boldsymbol{B_0}$ components or the local $\boldsymbol{B_0}$ strength penetrating the vessels varies, as the surface moves within the field gradient of $\boldsymbol{B_0}$.

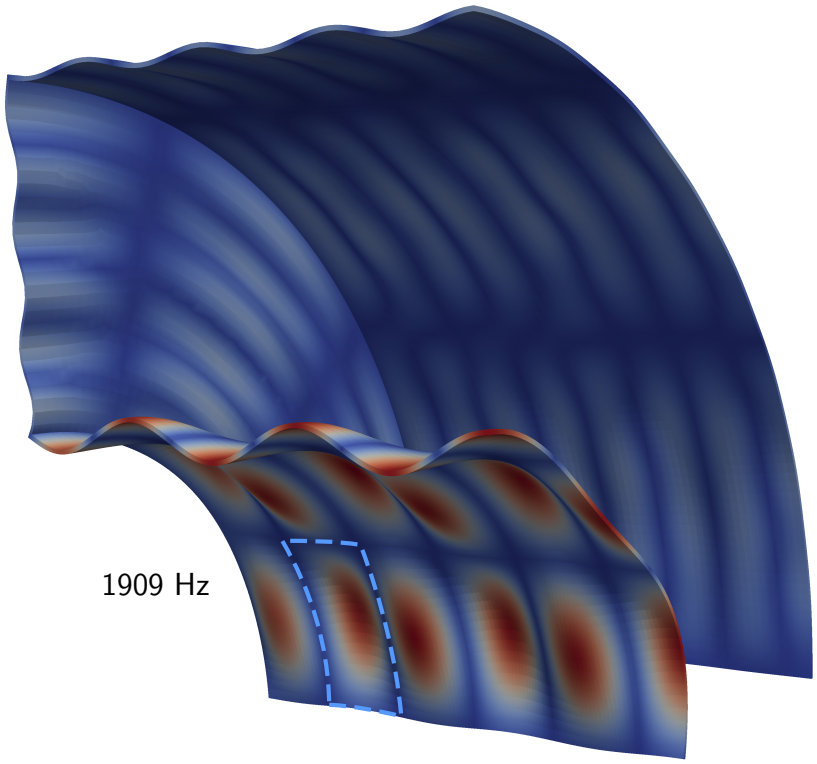

Figure 4.2 – Exaggerated illustration of a representative shape of an relatively high order eigenmode at $1909\,\mathrm{Hz}$ for an octant of a cryogenic vessel. The blue doted line indicates one extremum of the mode.

Considering the inner bore tubes of the vessels, the displacements in z remains relatively small compared to the according movement in r_c. This can be demonstrated by analyzing typical mode shapes (see Fig. 4.2).

In the frequency range of interest, approximately 0 to $3000\,\mathrm{Hz}$, the displacement of the modes shows clearly less than 50 extrema along one direction. The axial lengths of clinical MRI cryostats lie somewhere between $1\,\mathrm{m}$ and $3\,\mathrm{m}$. So in the worst case scenario one extremum of a mode would still have a length of more than $2\,\mathrm{cm}$.

The amplitude of the according radial displacement is maximal of the order of $1\,\mathrm{mm}$ and probably even clearly below. Otherwise movements in low order modes would cause collisions of the cryostat shields, which have never been observed, yet.

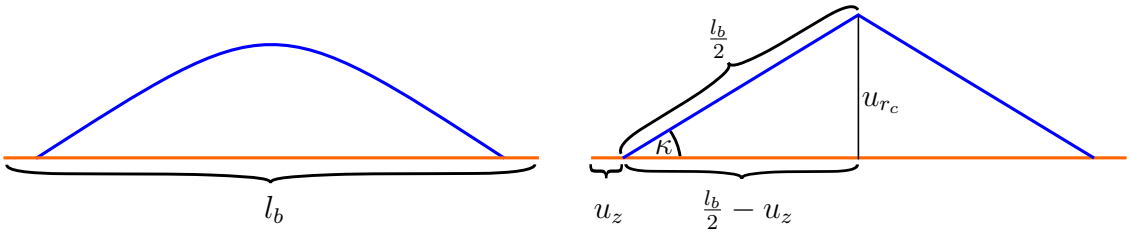

Figure 4.3 – Two illustrations of a cross-section through a mode extremum as indicated in Fig. 4.2. Orange represents the ground state and blue the mode shape. On the right, the mode shape is approximates as an isosceles triangle. The length l_b and the displacement u_r define the tilting angle $\kappa = \text{asin}(\frac{2u_{r_c}}{l_b})$. For typical l_b and u_{r_c} the angle is very small, resulting in significantly larger radial than axial displacement u_z.

Approximating the extremum as an isosceles triangle with a basic side of length $l_b = 2\,\text{cm}$ and a height of $u_{r_c} = 1\,\text{mm}$ (see Fig. 4.3), allows to estimate the maximal displacement possible in z-direction as

$$u_z^{(1)} = \frac{l_b\left(1 - \cos\left(\text{asin}\left(\frac{2u_{r_c}}{l_b}\right)\right)\right)}{2} = \frac{l_b\left(1 - \cos\left(\kappa\right)\right)}{2} \approx 0.005\,\text{mm} \tag{4.11}$$

introducing the displacement or tilting angle $\kappa = \text{asin}\left(\frac{2u_{r_c}}{l_b}\right)$. This even overestimating approximation clearly demonstrates that $u_z^{(1)}$ is less relevant than the radial displacement for movement induced changes of the magnetic flux. In this estimation, using a triangle, only a single isolated extremum was considered. For neighboring extrema the u_z work against each other, so that basically no axial displacement occurs (except at the most outer extrema), that would modify the surface penetrated by $\boldsymbol{B_0}$. The material is mostly stretched, as can be seen when supposing a perfectly rigid fixation at the boundaries for the bore. In this case the bore is still able to vibrate, clearly demanding a stretching of the material.

Thus, more important for magnetic flux changes, but still negligible, is the axial movement due to the tilting moment at the knots of the mode in combination with the thickness δ of the plate (Fig. 4.4). Typical values for δ are about $5\,\text{mm}$. Applying the displacement angel κ as used in equation 4.11 gives

$$u_z^{(2)} = \frac{\delta}{2}\text{sin}\,\kappa = \frac{\delta\,u_{r_c}}{l_b} = 0.025\,\text{mm} \tag{4.12}$$

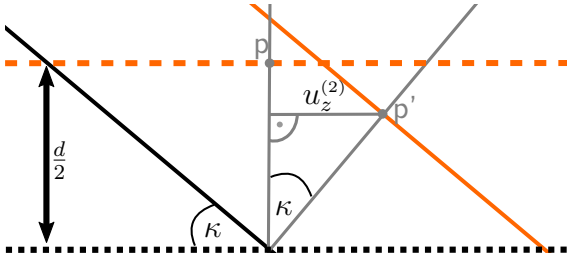

Figure 4.4 – Drawing of an exaggerated tilting movement at a knot of a mode oscillation. The black dotted line indicates the mid surface and the orange dashed line represents an outer surface of the layer at rest. By tilting the layer about κ the point p is moved to p' with an axial displacement of $u_z^{(2)}$.

for the axial displacement of point p to p'. Both $u_z^{(1)}$ and $u_z^{(2)}$ are about a factor of 200 or $\frac{d}{l_b}$ smaller than the u_{r_c} (maximal radial displacement). This demonstrates that the majority of secondary eddy currents are invoked by radial displacements of the cryostat vessels, being magnitudes larger for such small tilting angles. For the ends of the vessels, the roles of u_z and u_{r_c} have to be exchanged, since the main surface normal is rotated, but the estimation works analogously.

Following this argument, two main processes of interest remain on the inner bores that produce secondary eddy currents $\boldsymbol{I_S}$, which are responsible for field disturbances. The tilting modifies the amount of area penetrated by B_{0_z} and the displacement moves the conductive parts to different values of $\boldsymbol{B_0}(\boldsymbol{r})$.
The first case can as well be estimatedly described by Fig. 4.3. The area of the extremum exposed to axial $\boldsymbol{B_0}$ field is in first approximation directly proportional to u_{r_c}. Thus, the area change over time is proportional to $\dot{\boldsymbol{u}}$, yielding

$$I_{S1}(t) \propto \int \frac{du_{r_c}(t)}{dt}\, dt \tag{4.13}$$

The second cause for a magnetic flux change is a variation of $\boldsymbol{B_0}(\boldsymbol{r})$ seen by the surface due to movement, generating secondary eddy currents

$$I_{S2}(t) \propto \int \frac{dB_0(\boldsymbol{r})}{dt} dt \approx \frac{dB_0(r_c)}{du_{r_c}} \int \frac{du_{r_c}(t)}{dt}\, dt \tag{4.14}$$

Note that the terms can be expressed in this simplified way, as only radial displacement

is considered and $\boldsymbol{r}$ can be described as a constant value plus the variable displacement u_{r_c}. Moreover, for small displacements $\boldsymbol{B_0}$ varies in good approximation linearly in r_c for all time steps, so that the time dependency is also dominated by $\int (du_{r_c}(t)/dt)\ dt$. Using the resonance property of $\dot{\boldsymbol{u}}$ and $\boldsymbol{F_P}$ being in phase and combining the relationship 4.10 with 4.13 and 4.14 gives

$$I_S(t) = I_{S1}(t) + I_{S2}(t) \propto \int F_P(t)\ dt \propto \iint \frac{dB_G(t)}{dt} dt\ dt \tag{4.15}$$

Even if $\boldsymbol{B_G}(t)$ is not purely sinusoidal, it is still periodic in time and can thus be expressed as a sum of sinus and cosine terms, as already used in section 3.1.1. Consequently, the mathematical operation of two integrations and one derivation introduces a phase shift of $-\pi/2$ between the read-out gradient and the movement induced disturbing field. Since the sign of $\boldsymbol{F_P}$ is given by $\boldsymbol{I_P} \times \boldsymbol{B_0}$ it is dependent on the local direction of these quantities. Thus, the phase relation can also occur with an additional phase shift of π and the general phase relations is given by $\pm\pi/2$.
Both of these solutions should appear as solid ghosts (compare Fig. 4.1), since off resonant cryostat movements, having a phase shift significantly different from $\pm\pi/2$, have small amplitudes and do not produce strong disturbances. Accordingly, the following considerations will only consider solid ghosting with $\vartheta = \pm\pi/2$ (Eq. 4.3). The actual presence of this phase difference will be experimentally measured in section 4.3.4.

4.1.3 Gradient-like field disturbance at resonance

When considering an additional disturbing field distribution $B_e(\boldsymbol{r}, t)$ corresponding to an x-gradient (Eq. 4.6), the resulting ghost artifact possesses no amplitude at $x = 0$ (see Fig. 4.5), since there is no phase variation at that image position with reference to the undisturbed case. The disturbance and therewith the ghost amplitude increases with the distance to $x = 0$ (pixel 65 in the image).
In the followings theoretical example the onset behavior of the mechanical vibration is recreated in the calculation by multiplying the right hand side of equation 4.3 with an exponential term

$$B_e(\boldsymbol{r}, t) = B_e\, c_{x_1}\, x\ \sin\left(\omega_{\mathsf{EPI}}\, t + \frac{\pi}{2}\right) \cdot \left(1 - \exp\left(-\frac{t\ \omega_{\mathsf{EPI}}}{\tau\ 2\pi}\right)\right) \tag{4.16}$$

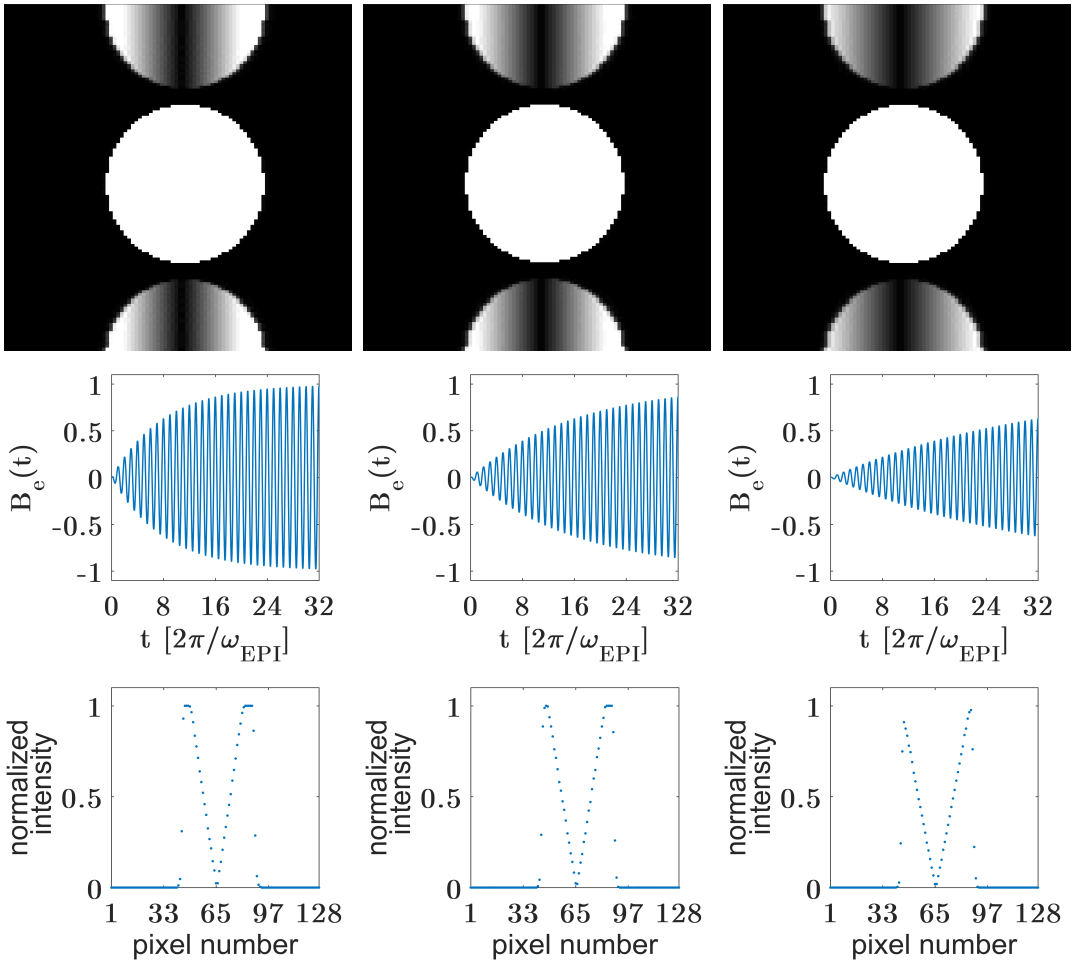

Figure 4.5 – Top row: Simulated ghosting artifacts for an x-gradient disturbance possessing an onset time constant τ of 8 on the left, of 16 in the middle and of 32 on the right. Middle row: The corresponding disturbance amplitude over time. $B_e c_{x_1}$ (from Eq. 4.16) is set identical for all oscillations. Bottom row: Profile plots showing the gray scale values of the first row of pixels in the above images. The amplitude is normalized to the maximal value of the weakest ghost, leading to a steeper profile for the images with shorter time constants.

The time constant τ is without unit herein and is indicating the number of periods with frequency ω_{EPI} needed by the mechanical oscillation to reach approximately 63% ($\approx 1 - 1/e$) of the steady state amplitude.

Figure 4.5 also demonstrates the influence of a growing time constant for a 128×128 pixel image, needing 64 cycles of the read-out gradient oscillation to acquire the complete image information. The general shape of the ghosting is hardly affected by the varying time constants, since the disturbing signal already is on a relatively high level, when the sampling reaches the k-space center. In the given examples merely the amplitude of the artifact is reduced, which can be observed best with the profile plots in the bottom row of the figure. The plots show the 8 bit gray scale values of the pixels in the top row (left to right) of the according image. As the contrasts of the images were adjusted so that the weakest ghost reaches the maximal gray scale value, the wedges in the profile plots for shorter time constants are more narrow and the plateaus at maximal intensity are broader.

In general, the spatial distribution of the distortion can not be expected to have a pure gradient-like or homogeneous form, but is a superposition of various terms. As a simple example one can consider a combination of just the two terms as given by equation 4.7. Since the Fourier transformation is linear, the effects of the resulting field disturbance are the sum of the effects obtained by the pure fields given in equations 4.5 and 4.6. Consequently, the superposition of a resonating homogeneous and a gradient field disturbance produces ghost artifacts that have no amplitude at the position where

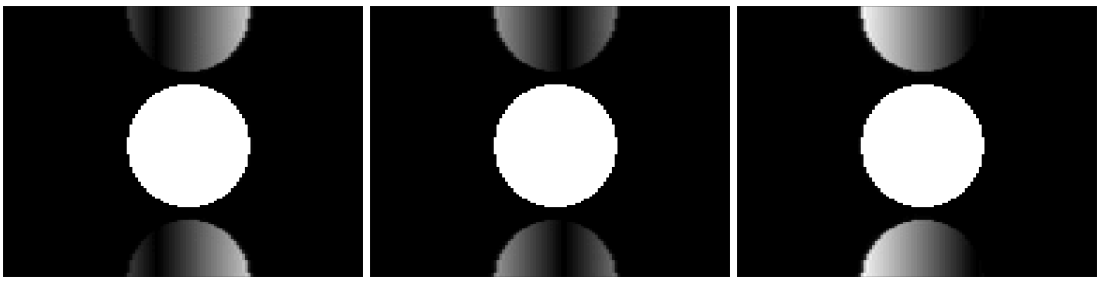

Figure 4.6 – Ghosting artifacts simulated for combinations of resonant homogeneous and gradient like distortions with $\tau = 8$ and $\vartheta = \pi/2$. The relation of c/c_{x_1} (see Eq. 4.7) defines the position in the image where the field disturbance is 0 (visible as black vertical line in the ghosting artifact).

gradient and offset field cancel each other out ($x = -c/c_{x_1}$). Figure 4.6 illustrates this property for different values of c/c_{x_1}. A measured ghosting artifact similar to the right image will be presented (Fig. 4.15 I) and further investigated in section 4.3.1.

4.2 Identification of cryostat modes responsible for resonant EPI ghosting

The initial motivation for this work was to identify the origin of particular EPI ghosting artifacts, which show a resonant frequency dependency, and potentially mitigate them. It is assumed, that both effects, the ECL and the ghosting artifacts in EPI have a common root cause, namely secondary eddy currents. Ghosting appears due to periodic distortions in the k-space of MR images. These distortions can be caused by oscillating magnetic fields emitted by eddy currents, which was described in more detail in section 4.1.3. The ECL investigation proved that the secondary eddy currents generated by magnetomechanical excitation produce such kind of oscillating currents. Otherwise the kinetic energy of CS would not correlate so strongly with the ECL measured on the HeV. Unfortunately, the simulations are not yet capable of reproducing the magnetomechanical resonances correctly for gradient switching frequencies (below $1500\,\mathrm{Hz}$) typically used in EPI (compare Fig. 3.19). It is, however, reasonable to assume that the same physics apply in both frequency ranges and are described adequately, but the problems met with the simulations arise due to an inexact description of the model or the boundary conditions. Such details can have a great influence on eigenfrequencies and on the coupling of modes. But the modes themselves must be present and their interactions and resulting effects can be estimated without being able to reproduce the detailed processes.

The following section will identify a pattern separating the high and low frequency modes of the CS inner bore, allowing an assignment of potentially ghosting relevant modes. This information is used to investigate the excitability of these mode shapes with the GC stray field. Therefore so-called 'modal participation factors' (PFs) are introduced. The PFs will be utilized to reduce the ghosting artifacts generated by an X-gradient coil prototype through modifying the GC wire pattern.

4.2.1 Mechanical modes of the cryostat inner bores

Before evaluating the relevant mode shapes of the cryostat inner bores, it is helpful to introduce a nomenclature for these modes. Since the bores are basically thin hollow cylinders with negligible thickness, it is sufficient to characterize the modes with the remaining degrees of freedom in axial (z) and circumferential (φ_c) direction. For a homogeneous cylinder with clamped ends all modes can be characterized by the number of extrema that are equally distributed along each direction. In z-direction each extremum is counted (N_z), while in φ_c-direction pairs of extrema are counted (N_φ). An odd number of extrema is not possible for modes along a periodic coordinate. Thus, a mode can be named using the tuple (N_z, N_φ). As an example figure 4.7 illustrates an $(1, 3)$ and a $(3, 5)$ mode.

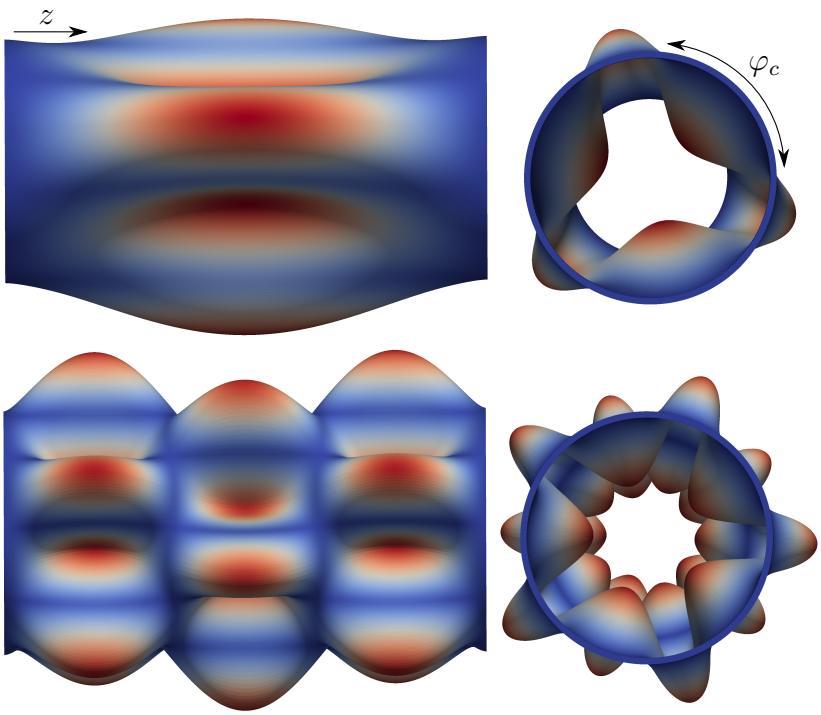

Figure 4.7 – Exaggerated illustration of two cylinder modes that occur on the inner bores of the MRI cryostat to explain the nomenclature of the modes. The pictures on the top show two perspectives on a mode with one extremum in axial (z) direction and six extrema in circumference (φ_c). As φ_c is periodic, only even numbers of extrema are possible. Thus, there are three pairs of extrema in circumference and the mode is well defined being named '$(1, 3)$ cylinder mode'. The pictures on the bottom accordingly show a $(3, 5)$ mode shape.

The results of the ECL simulations allow a clear assignment between mechanical modes of the CS and strong secondary eddy currents in the high frequency range. Analyzing those dominant mode shapes for a Y- or X-gradient reveals that all of them possess the same circumferential order of $N_\varphi = 1$. Due to the symmetries of the Y- and X-GC excitations (compare Tab. 3.1) N_z needs to be odd, as there must be an extremum at $z = 0$.

For Z-gradients, per definition, N_φ has to be 0 for axial symmetric simulations. Symmetry reasons determine N_z to be even, leading to no displacement at $z = 0$. As a characteristic for both gradient types in the high frequency range, N_z lies between 10 and 20 while N_φ is 0 or respectively 1 for strong resonances.

In the low frequency range no modes with N_φ being 0 or 1 can be found on the inner bore, explaining why only minor ECL can be measured there for Z-gradients. With $N_\varphi > 1$ many combinations with various N_z are present. For the transversal gradients, however, N_φ can only be odd, again due to symmetry reasons of the GC stray field.

The conclusion drawn from these observations is, that N_z is unproblematic for the simulation. Complex modes with high N_z appear to be reproduced correctly, as long as the circumferential variation is of low order. The modes with $N_\varphi > 2$ or respectively their interactions, which potentially are relevant in the low frequency range, are probably inaccurately described by the FE calculations.
To investigate this hypothesis further, a participation factor analysis was employed, an alternative method for estimating the excitability of modes.

4.2.2 Magnetomechanical modal participation factors

The principal idea behind modal participation factors (PFs) is the analysis of the agreement between a potential exciting force distribution and the mode shapes of a body. The eigenmodes correspond to eigenvectors that span the whole space of possible movements of the body. Accordingly, every force distribution acting on the body can be expressed as a superposition of these eigenvectors. The pre-factors of the eigenvectors in this expansion are thus a measure of how much each mode shape participates in the described force distribution and are called modal participation factors.

Physically this means, if an instantaneous excitation (containing all frequencies equally) with a given spatial distribution is applied to a body, the body would react according to the PFs, performing a vibration assembled of the eigenmodes oscillating at their eigenfrequencies. How much each mode is participating in that movement is given by the PFs. An alternative perspective is that PFs directly give information about where strong resonances can be expected, when using a certain force distribution. Driving the force at a frequency of an eigenmode with a large PF results in a more effective excitation than at a frequency of a mode with a small PF.
The concept of PFs will be applied to the magnetomechanical simulations of the MRI scanner. Therefore, it will be explained how the force distribution acting on the cryostat is approximated. Then, the method will be applied on the Z-gradient designs from section 3.1.6 to validate the principal functionality of the approach.

The analysis of the PFs is limited to the CS as it plays the dominant role in the coupling behavior within the cryostat. The combination of possessing the highest conductivity and also the lowest density makes it the most sensitive structure concerning movement excitations due to Lorentz forces. Secondary fields by movements of the OVC are assumed to be significantly less than the transmitting GC stray field. Simulations in section 4.2.4 will validate this assumption. Thus, for being able to predict the behavior of the system correctly it is essential to describe the GC-$\boldsymbol{B_0}$-CS interaction precisely.
As a consequence, a modal analysis of the CS alone is sufficient for the PF calculation. It yields the relevant eigenmodes (numbered by q) and the corresponding displacements $\boldsymbol{u_q}$. For obtaining the force distribution on CS, additional approximations are adopted to facilitate and speed up the PF approach.

Primary excitation forces within the MRI system occur due to the interaction of currents and magnetic fields (Lorentz forces). The strongest Lorentz forces acting on the cryostat will always be related to the $\boldsymbol{B_0}$ field, as it is at least three orders larger than other present fields (a property already applied for simplifications in the harmonic matrix solver in Sec. 2.6.3). Hence, the considerations for the PFs are limited to those forces

$$\boldsymbol{f}_{\mathrm{PF}}(\boldsymbol{r}) \propto \boldsymbol{J}(\boldsymbol{r}) \times \boldsymbol{B_0}(\boldsymbol{r}) \tag{4.17}$$

The computation of $\boldsymbol{B_0}(\boldsymbol{r})$ is done analytically via a Biôt-Savart formulation for

homogeneous current density distributions as it is described by [50]. $\boldsymbol{J}(\boldsymbol{r})$ is subject to further assumptions to simplify the calculation of the magnetomechanical PFs.
It is assumed, that the radial static stray field of the GC is entirely translated into eddy currents at the surface of the CS vessel. This implies that the field distribution coming from the GC is considered only insignificantly altered by dynamic processes. Due to the small thickness of the bore in radial direction the magnetic flux change related to the axial field is negligible.

Thus, only the radial stray field $\boldsymbol{B}_{\boldsymbol{r_c}} = B_{r_c}\boldsymbol{e}_{\boldsymbol{r_c}}$ is considered. Therewith the force distribution is solely estimated by the following combination of magnetic field distributions

$$\boldsymbol{f}_{\mathsf{PF}}(\boldsymbol{r}) \propto \boldsymbol{J}(\boldsymbol{r}) \times \boldsymbol{B_0}(\boldsymbol{r}) \propto (\nabla \times \boldsymbol{B}_{\boldsymbol{r_c}}(\boldsymbol{r})) \times \boldsymbol{B_0}(\boldsymbol{r}) \tag{4.18}$$

B_{r_c} is calculated with the Biôt-Savart formulation presented in section 2.6.1. Using analytical computation schemes for the magnetic field allows a reduction of the FE model to CS alone without GC or surrounding air, saving a vast number of elements.
Knowing $\boldsymbol{f}_{\mathsf{PF}}(\boldsymbol{r})$ and $\boldsymbol{u_q}(\boldsymbol{r})$ allows to calculate the PF of the mode q

$$\mathsf{PF}_q = \frac{|\sum_{\mathsf{el}}\ \xi_{\mathsf{el}}\ \boldsymbol{f}_{\mathsf{PF}}(\boldsymbol{r}_{\mathsf{el}}) \cdot \boldsymbol{u}_q(\boldsymbol{r}_{\mathsf{el}})|}{\sum_{\mathsf{el}} \xi_{\mathsf{el}} |\boldsymbol{u}_q(\boldsymbol{r}_{\mathsf{el}})|} \tag{4.19}$$

The index 'el' is used for numbering the FEM elements and ξ stands for the volume of the element. The weighing with the element volume is important for meshes using elements of different sizes. Otherwise small elements would be considered equivalent to large elements, although their contribution to the movement is less important. Also for the comparability of meshes with different numbers of elements this weighing is necessary. The application of PFs for mesh comparisons can be helpful to optimize the mesh resolution. Addressing this purpose the principal considerations for magnetomechanical PFs have already been published [51].

Typical displacement results of modal analysis are normalized via the underlying mass matrix. This normalization puts a bias on the displacement amplitude and can thereby spoil the informative value of the PFs. Therefore the PF calculation contains its own normalization via the division by the sum over all element displacement amplitudes, making the overall displacement per mode comparable.

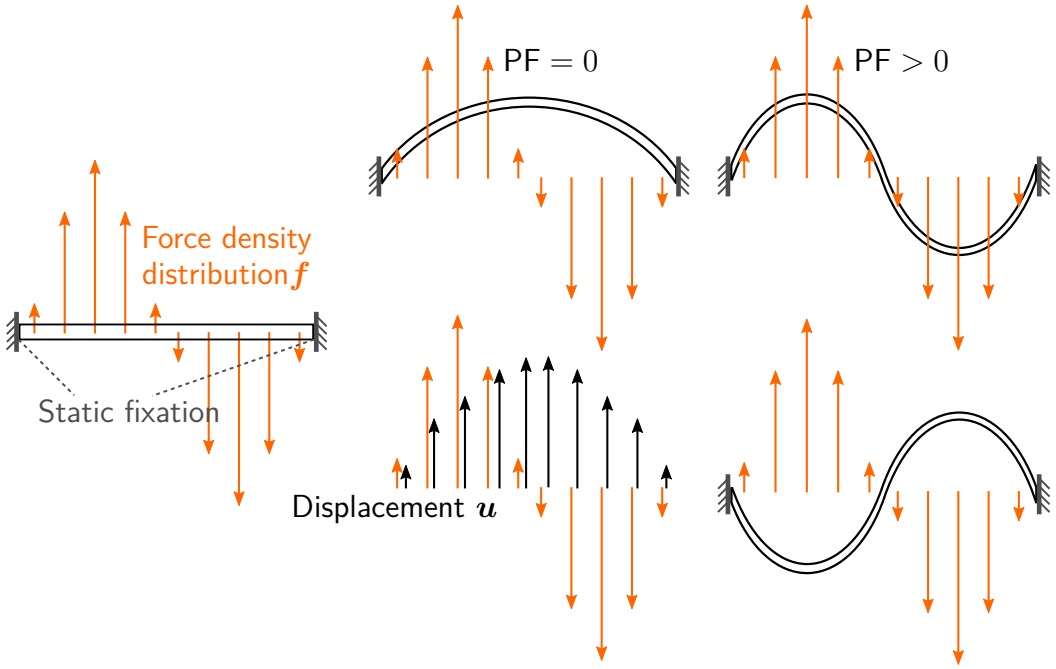

Figure 4.8 – Properties of the PFs demonstrated on a one dimensional bar that is clamped on both ends. On the left the position of rest is shown with a force density distribution $\boldsymbol{f}$. The PF of the first mode of the bar for this force distribution is 0, since the displacement $\boldsymbol{u}$ is symmetric to the middle of the bar, while the force is anti-symmetric. The scalar products of the $\boldsymbol{f}$ and $\boldsymbol{u}$ vectors along the bar compensate each other. On the right the second mode of the bar with a large PF is illustrated in two equivalent representations exemplifying why the absolute value in the enumerator of equation 4.19 is needed.

Basically the PF is a measure for the parallelism of the mode and the force distribution, since the scalar product between $\boldsymbol{f}_{\mathrm{PF}}(\boldsymbol{r}_{\mathrm{el}})$ and $\boldsymbol{u}_q(\boldsymbol{r}_{\mathrm{el}})$ only adds a significant contribution in that case. It is important to mention that the absolute value is computed after the sum of all scalar products has been evaluated. This way positive and negative, respectively parallel and anti-parallel, contributions can compensate each other. A simplified illustration of these properties is shown in figure 4.8.

Taking the absolute value of the sum is reasonable, since the modal results represent harmonic movements and the displacement solely represent the maximal amplitude in one of two possible temporal phases. The phase can either be 0 or π, thus the sign for all displacements in a mode can as well be inverted altogether and represent the

same mode. This inversion would also change the sign of each scalar product and consequently of the sum as well. Accordingly, the absolute value is considered to treat positive and negative results equally.

In the following, the magnetomechanical PFs are applied on the Z-gradient designs of section 3.1.6 as a proof of concept. Since Z-gradient ECL only appears in the high frequency range, where ECL simulations have shown that the inner bore is the dominant magnetomechanically interacting component for 1.5 T MRI systems, the PF computation was limited to the CS inner bore.

Both, the radial and axial component of the stray fields are plotted in figure 4.9. Note that the radial field is symmetric with regard to $z = 0$, while the axial stray field is anti-symmetric. The field components are visualized separately, because the radial field is responsible for the generation of the primary eddy currents, since it is the component orthogonal to the inner bore vessels. Yet, the axial field is a good estimate for the qualitative distribution of the eddy currents, as has been shown with figure 3.13. The dependency $J_{\varphi_c}(z) \propto -B_z(z)$ is hence used to calculate an estimate for $\boldsymbol{f}_{\mathrm{PF}}$.

The PF analysis investigates the agreement between the generated forces of the radial GC stray field and the mode shapes. Note that the axial stray field (right plot in Fig. 4.9), indicating the primary eddy current distribution, of design C has two additional zero crossings between z position 0.4 and 0.8 compared to design A, besides the general smaller amplitude. This stray field modification is assumed to be the main reason for the disproportionately (concerning field amplitude) strong ECL reduction, since it leads to a force distribution exciting higher order mode shapes as found at frequencies above 3000 Hz, which are not relevant for common MRI. Figure 4.10 shows how the PFs calculation resembles this statement. By comparing them to the according ECL spectra (Sec. 3.1.6), it is also clearly demonstrated how well the PFs reproduce the global trend of the ECL behavior despite some frequency shifts.

The occurring discrepancy of the PFs and the eddy current loss simulations has various reasons. Concerning the frequency shift of the resonances it has to be considered, that $\boldsymbol{B_0}$ leads to an effective stiffening of the mechanics (as included in Eq. 2.68),

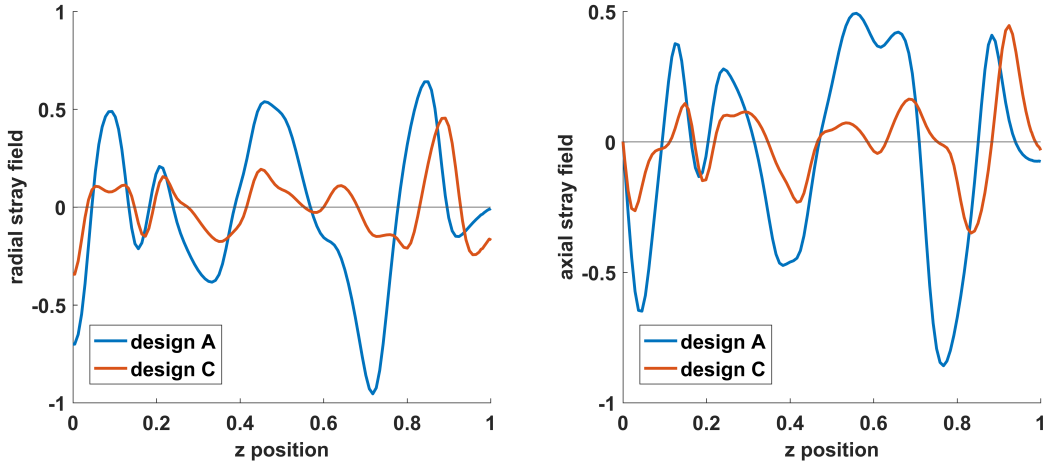

Figure 4.9 – The radial and axial stray field distribution for the two Z-GCs at the radius of CS. The values are normalized to the maximal amplitude of design A as seen in figure 3.6. Due to the (anti-)symmetry concerning $z = 0$ only half of the GC length is plotted.

increasing eigenfrequencies. Every eigenmode is thereby affected differently, since the modes generate different secondary eddy current distributions. This depends on the relative movement in relation to $\boldsymbol{B_0}$. The PF calculation neglects these secondary effects, leaving the purely mechanical eigenfrequencies unaffected.

For the amplitudes this also has to be considered. As shown earlier (in section 3.3.2) the fields emitted by the secondary eddy currents on the CS are mainly responsible for the eddy currents that are induced on the HeV. While the PFs only calculate how much a mode is partizipating, the ECL simulation also takes into account where it is moving within $\boldsymbol{B_0}$, which additionally scales the value.

Consequently, the PFs can be employed to make qualitative statements on resonance changes for various GC designs within the same magnet. However, to obtain absolute values for the loss, a direct coupled simulation is necessary.

The adavantage of the PF method is its speed and easy applicability. Predicting the eddy current losses via a coupled harmonic simulation requires a complete FE model. Although Z-gradients can be treated with axial symmetric models, requiring only a few

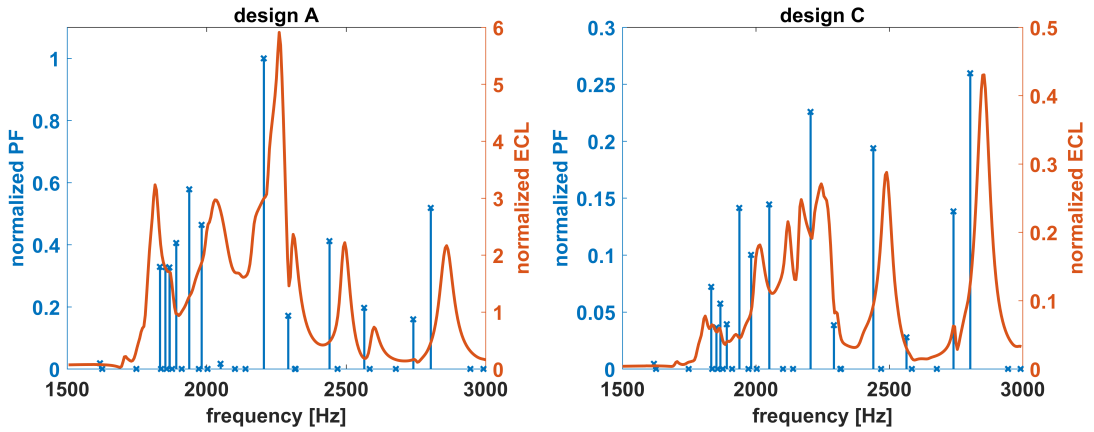

Figure 4.10 – Illustration of the applicability of the PFs for Z-gradient GCs. Both plots show the calculated PF values (normalized to the maximum for design A) together with the coupled simulation results of the ECL. Although there are discrepancies like frequency shifts for resonances, the PFs resemble the behavior very well. The PFs also clearly indicate that design C is preferable when the eddy current losses should be minimized.

minutes to solve, the preparation of the models demands additional effort for every GC modification. When changing the GC design, the model has to be remeshed and checked for inconsistencies.

The calculation of the PFs, in contrast, can be done with the Biôt-Savart formulation, so that no extra FE models are necessary for the computation. Furthermore, since the mesh on the CS is not varied, the eigenmodes only need to be calculated once for all GC designs. For one GC design the PF algorithm is thereby reduced to the recomputing of the stray field, followed by simple matrix multiplications and basic algebra operations, everything being executable in a couple of seconds on ordinary computers. This allows an interactive design process including magnetomechanical interactions of the MR magnet and the Z-GC coil. Introducing an additional design constraint based on crucial PFs might therewith provide a valuable extension to the current GC optimization processes to avoid undesired secondary magnetomechanical effects. This approach can also be expanded to X- and Y-gradients (see the following section), but due to the greater number of elements and the higher mode density in 3D, the CPU time and memory demands are currently too high for interactive computation.

Although the PF analysis is not capable of predicting the whole complex interaction

mechanisms within the magnetomechanical FE-model of the MRI system, it can serve as indicator of how the cryostat will react to the gradient stray field. Thereby the computation of the PFs is fundamentally faster, as it works with indirect coupling of mechanics and magnetics. It replaces pure numerical efforts with an understanding of the underlying physics. The next section will cover how the PF method supported the redesign of an X-gradient to reduce an EPI-ghosting artifact.

4.2.3 Mitigation of an EPI ghosting artifact considering modal participation factors

It was already demonstrated that the CS is the dominant source for strong secondary eddy currents. When accepting the hypothesis, that EPI ghosting can be caused by secondary eddy currents, it is reasonable to also consider the movement of the CS responsible for the secondary fields generating ghosting. The secondary magnetic fields causing the ghosting disturbances in EPI should in particular originate from the inner bore since the distance is the smallest to the FOV. Consequently, the minimization of the excitation of mechanical resonances of the CS inner bore in the low frequency range (were EPI sequences are driven) should reduce those disturbances. Although the simulations in the low frequency range are not reliable, it is possible to achieve such a minimization.

From section 4.2.1 it is known that the basic cylinder modes with an order higher than 2 in circumferential direction are located in this frequency range. Even without knowing the exact eigenfrequencies and interaction mechanisms, the PFs should still be able to predict how much a variation in GC stray field changes the excitation potential of these CS inner bore modes.

The underlying modal analysis is done on an octant model of the CS with the mechanical boundary conditions appropriate for an X-GC excitation (Tab. 3.1). This already limits the considered number of modes to the ones with the correct symmetries. The ends and the outer bore are included in the computation to evaluate how important the modes are, which these components add to the ones of the hollow-cylindrical inner bore. The resolution of the mesh is chosen identical to the ECL simulations and for the

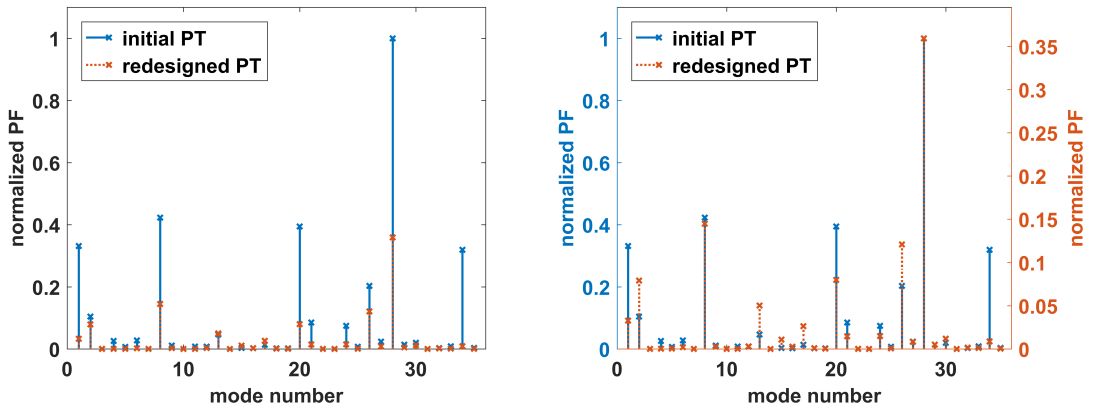

Figure 4.11 – Plots of the PFs for the initial prototype (PT) design and the design built after the optimization of the stray field. All values are normalized to the maximum value obtained with the initial prototype. The right plot rescaled the redesign PFs to visualize the relative changes as if the maximal value were the same for both designs.

calculation of B_{r_c} the same line segment length for the Biôt-Savart filaments is used. To evaluate $\boldsymbol{J} \propto \nabla \times \boldsymbol{B}_{r_c}$ the stray field is interpolated[1] on the cylinder surface between the positions were B_{r_c} is determined to allow the calculation of the spatial derivatives.

The left plot of figure 4.11 presents the resulting PFs for a frequency range of $\pm 300\,\mathrm{Hz}$ of the measured ghosting frequency in blue. The five highest values can be identified as the $(1,3)$, $(1,5)$, $(1,7)$, $(3,3)$ and $(3,7)$ cylinder modes. Thus, for the optimization it was tried to create a stray field that excites these modes less. The PF achieved with the best performing variation, that could also be built and tested, is shown in red in figure 4.11. A clear reduction of the PFs is observable.

When scaling the two designs to the same maximal value, one can see how the relative participation between the modes changes (right plot). In principle such scaling is comparable to changing the current driving the GC. This means that the new design should lead to a smaller transfer of magnetic energy into kinetic energy within the considered frequency range. Balancing this difference shows that the five highest values were not only reduced absolutely but also in relation to the other modes.

[1] A third order interpolation was performed, using the internal 'Interpolation' command of Mathematica (in version 10.4).

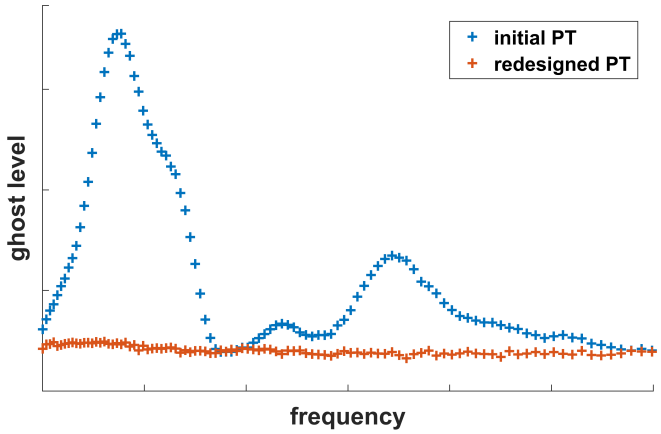

Figure 4.12 – Plots of the ghosting spectra in the investigated frequency range for the initial and redesigned gradient coil prototype. It is evident that the optimization using participation factors leads to an improved situation, mitigating the ghosting artifacts successfully as they get covered by background noise.

The initial high ghosting artifact level (Fig. 4.12), which motivated the redesign, was reduced to the background noise level of the image with the new GC design. In conclusion, the optimization via participation factors achieved a significant decrease of interfering distortions in the imaging process.

Although this method successfully reduced the ghosting it is not yet entirely proving the assumption, that the secondary eddy currents on the CS are responsible for the ghosting. The modification of the wire pattern has numerous other effects that might serve as potential explanations for the improved situation. More evidence will be presented in the next section, showing that simulations, which calculate secondary fields in the FOV, also predict a reduction of ghosting with the redesigned prototype. In section 4.3 measurement data will be presented, demonstrating that the fields emitted by the secondary eddy currents are also measurable in the FOV and that these fields can be associated with cryostat mode shapes.

4.2.4 Transient FE field computation

As a further test for the capabilities of the FE framework, this section tries to calculate the effect the redesign of the X-GC prototype has on the secondary fields in the

FOV. Therefore the iterative solver presented in section 2.6.2 is used. This decision is based on the following considerations. First of all, the iterative solving algorithm does not include simplifications as the harmonic linearized solution ($\boldsymbol{Q}$-terms; Eqs. 2.62 to 2.64). Without any simplifications, all the physics which is incorporated in the basic equations is taken into account. Thus, depending on the accuracy of the simulations, all fluctuating fields are modeled. The transient approach allows the application of the Biôt-Savart currents for the GC conductors, which simplifies the FE-modeling drastically, but still gives an exact description of the occurring physics. It allows a fast mesh generation by entirely rotating a 2D setup, providing an ideal symmetry for computing $\boldsymbol{B_0}$.

In the transient case it is necessary to expand the simulation model form an octant (used for the ECL calculations) to a quarter model, since the main coils and the X-GC are calculated simultaneously. The two coil types possess different boundary conditions on the x-y-plane (see Tab. 3.1). The quarter model covers half the z-axis, half the y-axis and the entire x-axis. Despite the increasing model size, the according supplemental unknowns and eventually extra computation time, this expansion of the model therefore also adds the possibility to reproduce field distortions not possessing the symmetry of the gradient fields, which could be introduced via the $\boldsymbol{Q}$-terms.

Since it is unknown at which frequency the ghosting-relevant resonances occur in the simulation, a wide frequency range has to be covered by the calculation. This is achieved by simulating a steep switch-off procedure, as already known from section 3.2.1, but this time including magnetomechanical coupling. The rapid switch-off of the GC current comes closest to a Dirac function, containing all frequencies equally. A pure Dirac function is not applicable, since it cannot be sampled reasonable with the transient time stepping, making it numerically hard to handle in the simulation. Similar to the investigations of the construction tolerances (Sec. 3.2.2), it is investigated what fields are present in the FOV after the GC current vanished. A Fourier analysis of the field variation in the FOV over time yields the frequency response of the magnetomechanical system to the switch-off process. On top of the already seen primary eddy current fields, which mainly decay exponentially in time (yielding a Cauchy-Lorentz-distribution in the frequency domain) additional fields of oscillating

secondary eddy currents should be present.

To ensure that the secondary effects are not buried below the numerical noise of the background field, it can become necessary to specify an unrealistic high amplitude for the GC current. The energy transferred in the mechanical vibration for a singular switch-off event can otherwise be too small to generate enough movement for the induction of strong enough secondary eddy currents.

According to the hypothesis of this work, the secondary oscillating fields are responsible of the ghosting artifacts. These fields are, however, superimposed with the primary fields, demanding a measure to separate the contributions. The static $\boldsymbol{B_0}$ background field is therein no problem as the Fourier analysis clearly assigns it to $0\,\mathrm{Hz}$. To achieve the separation of the primary and secondary fields, there were two methods investigated.

One possible approach is performing a purely magnetic simulation with an identical excitation as in the coupled case. This simulation should then deliver all primary eddy current fields and their decay. Subtracting the results of the magnetic simulation from the coupled one then yields the secondary fields plus the field variations generated by the movement of the primary currents. In the coupled simulation the vibrations of the cryostat also lead to a variation of the position of the eddy currents, which is altering the distance to the points of evaluation and therewith the fields present there. Such variations are not compensated by this 'subtraction method'.
A separation of primary and secondary fields can also be achieved, when reusing the results obtained by the coupled switch-off simulation for an additional coupled simulation. Explicitly, this method reenters the mechanical displacement results of the initial simulation as excitation into the second one without any GC activity. Thereby no primary eddy currents are generated, while the same mechanical behavior takes place. Thus, the same secondary eddy currents and fields are induced and can be analyzed without interfering primary dynamics. The drawback of this separating method is the extra time necessary to implement and run the second simulation. For each node ($\approx 10^5$-10^6) of the moving parts an individual function over time, defining its movement, has to be created and inserted in the new simulation. Furthermore, the additional simulation itself roughly takes the same time as the initial one.

In the investigated setup the differences between both methods were marginal and therewith particularly irrelevant for the assessment of the design modifications. This implies that the field changes in the FOV caused by oscillating positions of primary eddy currents due to the movement of the cryostat are negligible compared to the field effects produced by the alternating secondary eddy currents. The 'subtraction' method only removes the contributions of primary eddy currents as if they would not move. When these results are basically identical to ones obtained without any primary eddy currents, their movement can not be of high relevance for the given accuracy. Concerning this matter, equivalent results have been obtained with reliable 2D simulations in the frequency range above $1500\,\mathrm{Hz}$.

As has been claimed in the previous section, the movement of the cryostat in modes with 'high' circumferential order is suggested responsible for the appearance of disturbing fields generating ghosting. If that is the case, these fields need to have a similar spatial symmetry and even periodicity as the cryostat modes. For the evaluation of the spatial distribution of the magnetic field disturbances in the FOV, the imaging relevant axial field is described in spherical harmonics at a 10 cm radius.

Spherical harmonics span a complete set of orthogonal functions covering the surface of a sphere, hence every distribution of values on a sphere surface can be described as a combination of these functions. In spherical coordinates (see App. A.2) the spherical harmonic functions read as

$$Y_{l,m}(\varphi_s,\theta_s) = (-1)^{(m+|m|)/2}\; i^l \left(\frac{2l+1}{4\pi}\frac{(l-|m|)!}{(l+|m|)!}\right)^{1/2} \mathcal{P}_l^{|m|}(\cos\theta_s)\exp(im\varphi_s) \quad (4.20)$$

with $l \in \mathbb{N}$, m being integer satisfying $-l \leq m \leq l$ and

$$\mathcal{P}_l^m(\cos\theta_s) = (-1)^m \frac{(l+m)!}{(l-m)!2^l l!}\sin^{-m}\theta_s \frac{d^{l-m}}{(d\,\cos\theta_s)^{l-m}}(\cos^2\theta_s - 1)^l \quad (4.21)$$

describing the associated Legendre functions [52]. The following considerations are limited to the example of the mechanical $(1,3)$ cylinder mode (with X-gradient symmetry), which was identified by the participation factors as relevant for the generation of artificial object ghosts in the image. It is the mode with the lowest circumferential order,

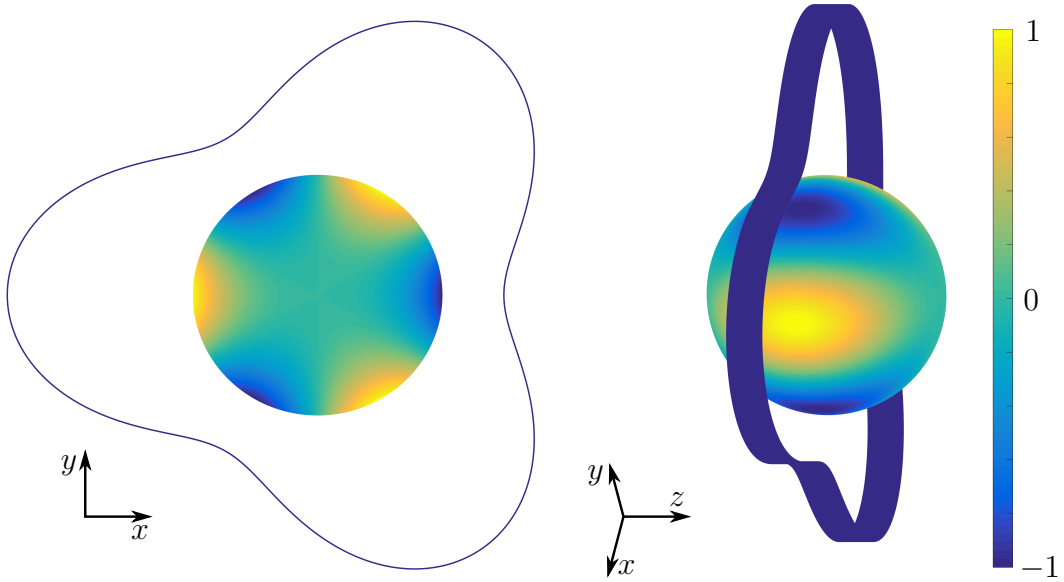

Figure 4.13 – Illustration of the real $\mathcal{A}(3,3)$ spherical harmonic distribution surrounded by a $(1,3)$ cylinder mode in two different perspectives. The proportions of the sphere and the hollow cylinder were adjusted for better visualization.

allowing the simplest demonstration of a correlation between the disturbing fields and the modal cryostat shapes.

The same circumferential periodicity and symmetry of the structural $(1,3)$ mode can be found in the spherical harmonic terms $Y_{3,3}$ and $Y_{3,-3}$. These terms can be combined to form a pure real function, which is appropriate for the description of the real valued magnetic field disturbance.

$$\mathcal{A}(3,3) = \frac{1}{2}\left(Y_{3,3} + Y_{3,-3}\right) \propto \sin^3\theta_s \cos 3\varphi_s \tag{4.22}$$

To illustrate an example for the commonality of cylinder modes and spherical harmonics the $(1,3)$ cylinder mode and $\mathcal{A}(3,3)$ are sketched in figure 4.13. The displacement of the mode and the distribution of the harmonic function show the same periodicity in circumferential direction around the z-axis.

Analyzing the frequency spectrum of the secondary fields on the 10 cm sphere centered in the FOV before and after the redesign for the $\mathcal{A}(3,3)$ term yields results for the switch-off response as plotted in figure 4.14. The original design shows clear resonant

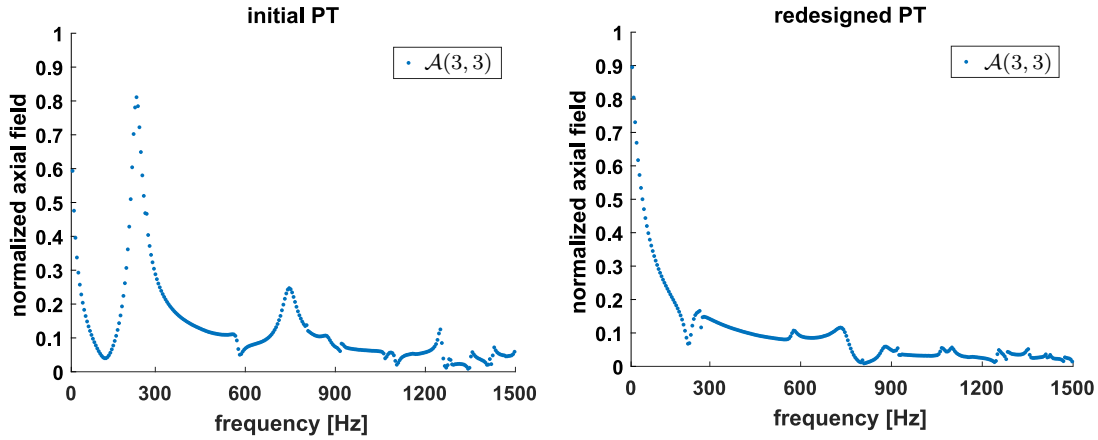

Figure 4.14 – Plots comparing the secondary field spectra generated by a GC switch-off, before (left) and after (right) the stray field optimization via PFs. The $\mathcal{A}(3,3)$ term of the axial field component shows significantly reduced resonances for the redesigned prototype (PT).

features, that are significantly reduced with the redesigned PT. This is another indicator for the causal connection between magnetomechanical interactions in the cryostat and MRI relevant field distortions. The optimized X-GC design using participation factors reduced the ghosting artifact, but a definite connection to the secondary eddy currents could not be demonstrated. The simulation results imply that the PF optimization also reduced secondary fields, which possess the same symmetries as mechanical modes of the cryostat, that have been addressed with the optimization.

The frequencies of the computed resonances do not agree with the frequencies where the ghosting effects were measured. This discrepancy is consistent with earlier ECL results, where measured and simulated peak positions in the low frequency range did not match due to inaccurate mechanical boundary conditions. Despite this disagreement concerning the correct eigenfrequencies, the simulation appears to be capable of reproducing principal influences of variations in the GC-$\boldsymbol{B_0}$-cryostat system. When the problems in determining the eigenfrequencies in the low frequency range can be overcome, the simulation possesses the potential to also formulate quantitative predictions. As already mentioned in section 3.3.1, the main suspect, expected to be responsible for the modal discrepancies, are the inaccurately modeled cryostat ends and their mechanical connection to the inner bores.

The second method, reentering the displacement results as boundary condition for another simulation, allows to separate the secondary fields reaching the FOV according to the vessels they originate from. In the simulation it is easily possible to only reenter the movement of the CS while fixating the other shields. Comparing the resulting fields to the ones presented above reveals hardly any differences, proving that the CS is majorly responsible for emitted secondary fields. So far the ECL simulations suggested that only secondary fields generated on the CS get absorbed at the HeV and practically no field transmits through the CS. This includes the secondary fields emitted by the OVC towards the HeV. This simulation demonstrates that secondary fields emitted by the OVC can also be ignored in the FOV compared to secondary fields originating from the CS.

This section has shown, that the 3D FEM framework is capable of computing magnetomechanical field effects in the FOV. This is remarkable, since it demonstrates that the simulation can handle magnetic fields with 10^7 difference in magnitude simultaneously ($B_0 \approx 1\,\mathrm{T}$ and secondary fields $\approx 0.1\,\mu\mathrm{T}$), which is numerically challenging. Moreover, it was argued, that movements of primary currents are of minor importance for computing fields in the FOV. Concerning the simulation point of view the obtained results indicate, that the redesign of the X-GC effectively reduced the disturbing fields in the FOV with geometrical properties comparable to the oppressed mechanical modes. To complete the picture on the connection between ghosting artifacts and secondary fields, the next section will show that such - so far only simulated - fields are also measurable in operating MRI systems and can be made responsible for ghosting artifacts.

4.3 Measuring magnetic fields generated by cryostat vibrations

The conclusions drawn in the previous sections will now be compared to actual measurements to establish a connection between ghosting artifacts and mechanical vibrations. Since the GC prototype investigated so far was no longer available, another ghosting artifact, in a different MRI system, is analyzed. Therefore different MR experiments are performed to determine the magnetomechanical features (i.e. onset behavior and time constant) of the responsible field disturbance. Then measurements

are presented, which utilize a pickup coil to confirm these properties and additionally allow the identification of mechanical modes by measuring secondary eddy current fields.

4.3.1 Time constant determination using EPI phase correction

The problem investigated is a ghosting artifact present at a particular 3 T MRI system and ω_{EPI} using the X-gradient for the read-out. The system is peculiar, since other MRI systems of the same type do not show extraordinarily strong ghosting when operating that gradient axis at that frequency. Consequently, an exceptional error in the build up of the particular system is assumed to be responsible for the phenomenon. The artifact was also not eliminated with an exchange of the installed GC. Thus, it can be excluded that the root cause is associated with the gradient coil and its construction tolerances, including tolerances in the GC wire pattern and in the shape of the GC stray field.

Figure 4.15 I illustrates the ghosting artifact when imaging a sphere with 10 cm radius using a 64×64 image matrix. The intensity distribution of the ghosts is comparable to the simulated one in figure 4.6 right.

Many procedures have been developed to reduce ghosting artifacts by means of data post-processing, either purely based on the image data (e.g. [53,54]) or using additional measurements (e.g. [55–61]) for calculating correction parameters.

All of these approaches have their capabilities, but are also limited in their general applicability or come at costs of increased noise or time consumption. A prevalent, robust and time efficient method uses short additional measurements, as first described by Heid [57], to evaluate the development of the magnetization phases over three successive echos without phase-encoding blips. The first and the third echo are thereby acquired with the same read-out gradient polarity and should ideally create identical data (the T_2^* decay can be neglected for typical ω_{EPI}). The discrepancies in the phase are then used to compensate for them in the entire EPI image.

This approach is capable of compensating discrepancies between even and odd echos, which occur identical within each read-out gradient cycle. An example would be a time

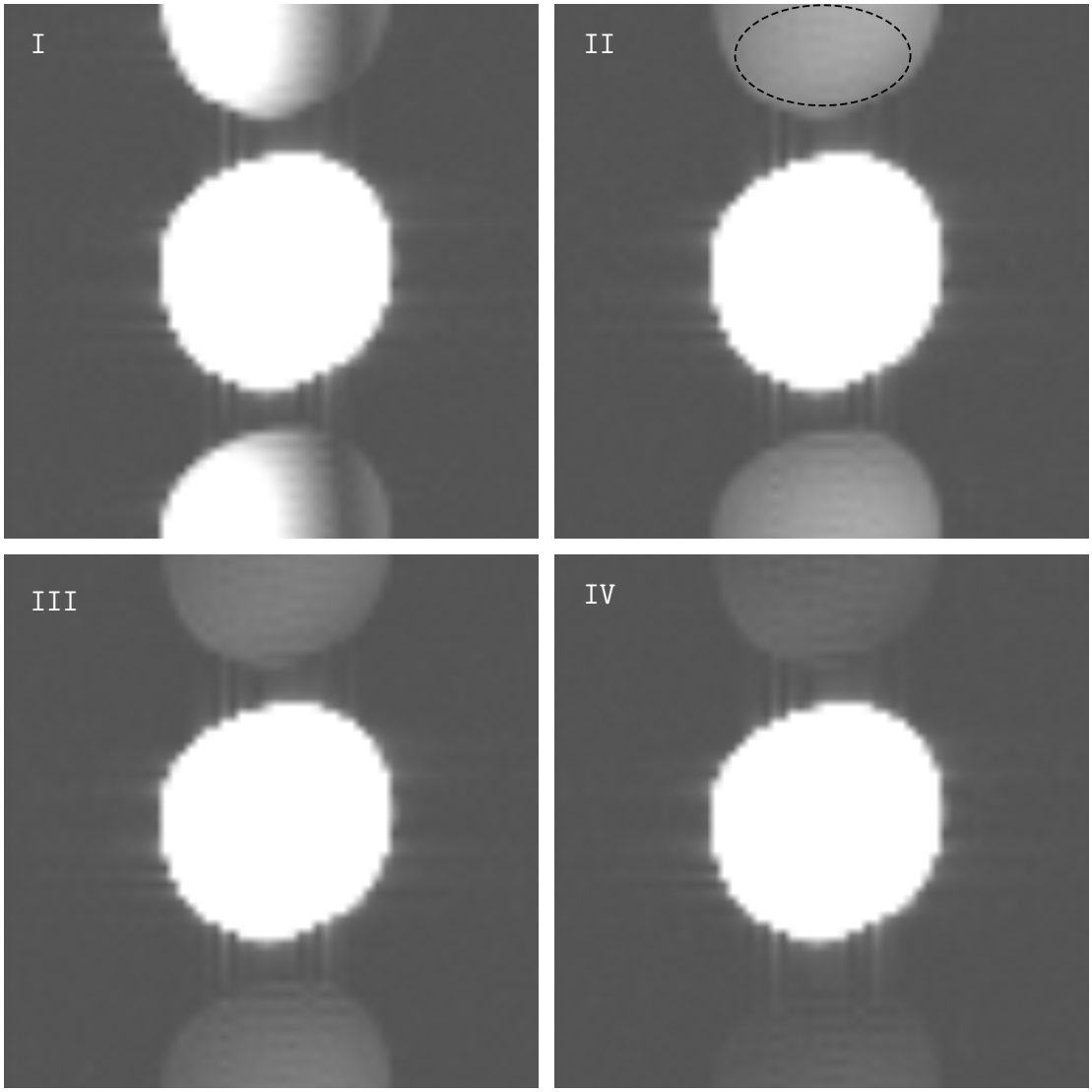

Figure 4.15 – EPI images for comparing the influence of EPI phase correction with a different number of gradient pre-cycles. In `I` no correction was applied. `II`, `III` and `IV` were phase-corrected with 0, 1 and 2 additional pre-cycles. The dotted line in `II` indicates the area which was evaluated for calculating the average magnitude of the ghosting artifacts.

delay in the RF receive chain, as this would lead to a mismatch between the point in time when the echo maximum appears and when the center of each k-space line is sampled. Variations that change over time between the even and odd echos can, however, not be compensated [62]. The signal disturbance of mechanical cryostat vibrations should therewith not be eliminated, as the phase correction scan does not cover its steady state.

Figure 4.15 II was acquired with the same EPI sequence as I but using the described additional phase correction scan for ghosting compensation. Thus, the ghosting signal visible in II is present due to undesired phase contributions which are not covered by the phase correction scan.

There is the possibility to prepend additional read-out gradient cycles (one period with ω_{EPI}) directly beforehand the phase correction scan. These pre-cycles provide more time for potential dynamic processes to reach their steady state. In figures 4.15 III and IV one or respectively two additional cycles were run in advance of the phase correction measurement.
It can be observed, that the pre-cycles reduce the intensity of the ghosting, indicating that the correction scan is executed at a time interval more similar to the state when the EPI sequence is acquiring the k-space center. The average gray scale value of the ghosting artifacts from II to IV (evaluated over the area indicated by the dashed ellipse in II) give 303 ± 46, 159 ± 22 and 88 ± 16.

Approximating the temporal evolution of these gray scale values via an exponential decay $\exp(-t/\tau_1)$ yields an estimate time constant of

$$\tau_1 = (7 \pm 2)\,\mathrm{ms} \tag{4.23}$$

The appearance of the remaining ghosts, thereby allows the interpretation, that the disturbing field must be of a rather homogeneous spatial distribution as simulated in figure 4.1 (bottom row).

Assuming a mechanical resonance of the cryostat as root cause of the uncompensated ghosting, the resonance should share this time constant. Knowing the time behavior of the oscillating distortion should allow a successful phase correction via the method

described by Feiweier [62]. The undesired change in the phase evolution of the magnetization can be compensated computationally before the reconstruction of the image. Information (temporal and spatial) on the distortion can be obtained in advance by simulations (i.e. as presented in Sec. 4.2.4). Alternatively simultaneous measurements of the CS movement should allow to calculate the resulting field distortions and to include their effects for an artifact reduced reconstruction.

4.3.2 FID after sinusoidal gradient activity

As the calculation of the time constant of the field disturbance was estimated indirectly with the ghosting intensity and only with a few data points, the validity is not entirely proven. To analyze this time constant more precisely, the disturbing field was investigated with another MR measurement, allowing a direct field measurement. A spherical MRI phantom with 10 cm radius is placed inside the FOV of the MRI system and the gradient (used for the EPI read-out) is driven with a sinusoidal current and the investigated EPI frequency for several periods, so that the mechanical oscillations can reach the steady state. The sinusoidal current is slightly adapted to compensate the field generated by the primary eddy currents. No slice-select gradient is played out, so a signal generated by the entire phantom is measured. Thus, the effects to be seen will represent an average over the complete sphere.

When the sinusoidal gradient excitation ends, an FID is measured with a flip angle of $90°$ (see Eq.2.19). During the FID no spatial encoding is applied. In an ideal case, the phase of the complex valued FID signal should remain constant. Any changes indicate distortions in the homogeneous field. Inhomogeneities in $\boldsymbol{B_0}$ are constant in time and lead to a linear change of the phase. Remaining parts of the primary eddy currents fields, which are not compensated by adaptions of the gradient current, also change slowly compared to the time constant of approximately 7 ms of interest. Consequently, the magnetic fields induced by mechanical vibrations should be traceable more clearly when considering the derivative of the phase over time, given they lead to a significant distortion. More precisely the field effects produced by the fade-off of that vibration should be visible. Since the onset and fade off time constants of damped forced oscillations are identical, this measurement allows a verification of the time constant determined in equation 4.23.

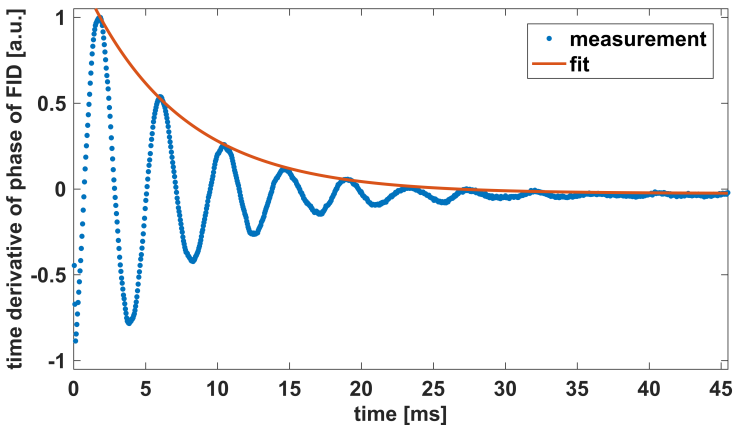

Figure 4.16 – Plot of the time derivative of the phase of the FID signal, acquired after a sinusoidal gradient excitation with the EPI frequency. For an undistorted FID a straight line would be expected, so the present oscillation is a consequence of disturbing fields. The red graph shows an exponential fit to the oscillation amplitude with a time constant of $6.7\,\text{ms}$.

Figure 4.16 illustrates the derivative of the phase of the FID together with a least squares fit curve, estimating the amplitude decay of the local oscillation maxima. The fitted function was

$$\mathcal{F}(t) = c_a \exp\left(-\frac{t}{\tau}\right) - c_b \tag{4.24}$$

The resulting time constant yields

$$\tau_2 = (6.7 \pm 0.2)\,\text{ms} \tag{4.25}$$

and is therewith in good agreement with τ_1. Consequently, it appears evident, that the remaining ghosting artifact, which could not be compensated with the phase correction, is a cause of the oscillating field distortion. These measurements prove the existence of a field distortion but can not give direct information about the root of the disturbance. In the next section it will be demonstrated that the time constant can as well be associated with a mechanical oscillation in the cryostat.

4.3.3 Pickup coil measurements at 3 T

MR measurements are typically limited to the volume where $\boldsymbol{B_0}$ is very homogeneous. This limits the capability to identify sources of distortions that lie outside of this FOV.

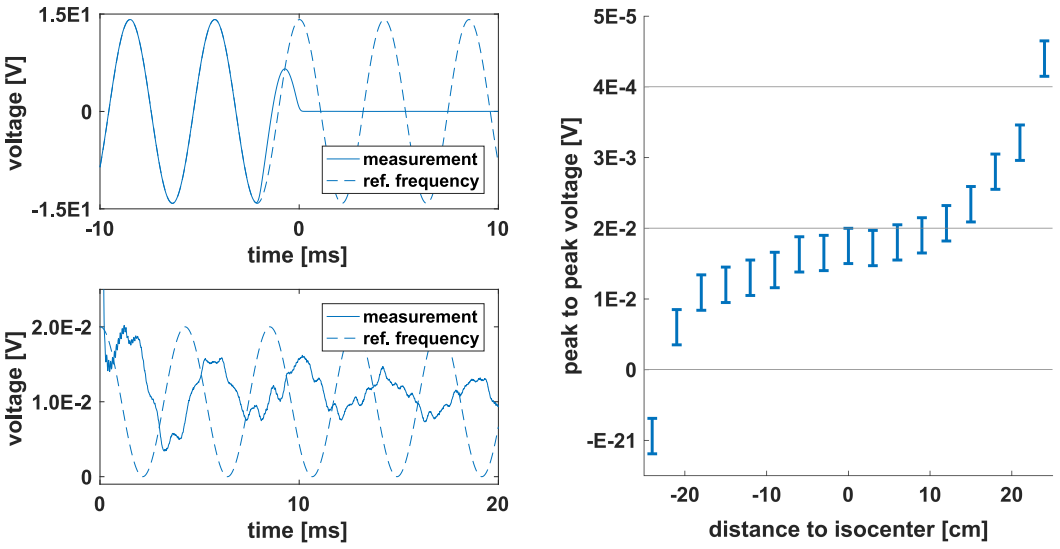

Figure 4.17 – Measurement results with the pickup coil along the axis of the investigated gradient within the inner bore. The left plots show two time windows of an exemplary signal acquired at ≈ 10 cm distance to the isocenter. The GC activity is switched off at 0 on the time axis. The dashed graphs serve as aid to compare phase and frequency of the exciting and excited signal. On the right plot, a clear signal offset can be seen, confirming the field distribution expected for the solid ghosting artifacts in figure 4.15I .

To overcome this restriction, a pickup coil was used as sensor. It allows the measurement of dynamic magnetic field variations, independent of the background field. The coil employed here has been cylindrical with a length of 1.5 cm, a radius of 2 cm and an inductance of 214 µH. For measuring the induced voltages it has been connected to a commercially available digital oscilloscope (PicoScope 4824). All measurements have been averaged eightfold and filtered with the 1 kHz low-pass filter included in the PicoScope software, if not stated differently.

The first experiment using the pickup coil aimed on reproducing the results obtained by the FID phase analysis in the FOV of the MRI system. The relevant gradient was driven with a sinusoidal current for 12 periods, enclosed by a smooth onset and fadeout characteristic to reduce higher harmonic contributions in the potentially excited magnetomechanical vibrations. An exemplary signal acquired with the pickup coil is shown in the plots on the left of figure 4.17, where the dashed line represents a virtually ongoing excitation as reference for comparing its phase and frequency to

the measured signal after the GC switch off (set as 0 on the time axis). The upper plot demonstrates the signal difference of the excitation and the resulting effects. This highlights the problem that the oscilloscope has to be operated in an input range wide enough to avoid damage due to the voltage induced by the gradient excitation. As a consequence, the accuracy of the oscilloscope is reduced for the comparable small aftereffects, which are plotted in the lower graph. One can recognize an oscillation with a similar frequency as the excitation possessing a phase difference in the region of $\pi/2$. However, the signal is corrupted by interfering distortions and is not practical for calculating the decay time constant or exact phase relationships. An evaluation of these properties is done with a higher quality signal later in this section. For the measurements in the FOV, only the the peak-to-peak voltages of the first period after the excitations will be investigated in the following.

The peak-to-peak amplitude at different positions in the FOV can be used to double check the hypothesis that the distortion is spatially homogeneous within the FOV. For that purpose the pickup coil was placed in the isocenter of the magnet and then sequentially moved along the axis of the applied gradient. The orientation of the coil was chosen to measure the axial field components. Positions of the coil further away from the isocenter than $25\,$cm were omitted, since the voltages induced by the excitation gradients would become excessively high for the oscilloscope. It is possible to expand the measurement region, when reducing the amplitude of the gradient excitation, but in this case the signal of interest also loses amplitude and therewith accuracy. For the purpose of this experiment the coverage of $50\,$cm proved to be enough.

The results of the measurements are shown on the right in figure 4.17, illustrating the constant offset that was suggested by the appearance of the solid ghosting artifact after the phase correction (compare Fig. 4.15). There is also a linear trend visible between $-10\,$cm and $+10\,$cm, but it is clearly inferior to the constant offset and lies within the error margin. The measurements with the pickup coil in the FOV show that it is possible to detect the distortion fields responsible for the ghosting artifact, which are assumed to be present due to magnetomechanical interactions. As already indicated by the right plot in figure 4.17 the signal increases towards the magnet bore. Since the GC activity is needed to excite the signal, it is, however, not possible to

measure directly at the cryostat inner bore, as the GC induced voltages would exceed the measurement range of the oscilloscope. Using smaller GC current amplitudes would also reduce the signal of interest, providing no benefit for the measurement accuracy, as the disadvantageous ratio between the voltage induced by the excitation and the response remains. The same argument holds for other means for adapting the voltages, seen by the oscilloscope, to the measurement range (i.e. using a pickup coil with less inductance or connecting additional resistors).

To improve the signal quality, the measurement position was allocated at the cryostat ends. Here, the distance from the pickup coil to the cryostat is clearly smaller than in the inner bore, as the GC is not placed in between. According to the simulations, it has been assumed that a relatively high contribution of the ends to the cryostat vibrations should be present at the investigated excitation frequency. Consequently, the achievable ratio between the voltage induced by fields present after the excitation and the excitation itself should be larger than in the FOV, if the vibrating cryostat is the source of the distortions.

The measurements were acquired along a radial line covering the radial extent of the cryostat ends as far as possible. The pickup coil was attached directly to the cover of the MRI system (a few cm away from the OVC). Due to the curved design of the housing connecting the inner bore and the ends (compare Fig. 1.1) the evaluated region is limited to the entirely flat part, which is slightly shorter than the radial length of the CS ends. The coil was oriented to acquire the axial (z) field component. The circumferential position of the line was chosen to be parallel to the direction of the exciting gradient, since the generated field amplitude and consequently the expected mechanical vibration should be maximal there.

Figure 4.18 shows selected results obtained by these measurements. In the left plot, the measured signal with the maximal peak-to-peak value is shown together with the virtual ongoing excitation. Comparing the amplitudes to figure 4.17 indicates, that the signal to noise ratio is improved for the first milliseconds. The signal can be used to calculate a time constant for the signal decay, using the the local peak values as fitting points for an exponential decay (see Eq. 4.24).

The computation of the time constant yields

$$\tau_3 = (6.1 \pm 0.8)\,\text{ms} \tag{4.26}$$

which lies within the range of the time constant estimates τ_1 and τ_2 determined earlier (Eq. 4.23 and Eq. 4.25). The fit is illustrated in the left plot of figure 4.18.

An evaluation of the phase relationship between the excitation and the measurement is impossible, since the frequency of the measured damped oscillation is higher than the reference and additionally the signal becomes clearly distorted after $15\,\text{ms}$. The frequency difference indicates that the cryostat ends possess no resonance at the frequency responsible for the ghosting artifacts. Consequently, the ghosting relevant field distortions in the FOV most likely originate from the cryostat inner bores.
The difference in frequency also explains why the time constant τ_3 calculated here is considerably different from τ_1 and τ_2, although the error margins overlap. The mechanical and magnetic coupling between the inner bore and the ends is not infinitely strong, leading to more or less individual component eigenmodes, which posses different damping properties. But the components are made of similar materials, moving in a comparable magnetic field at slightly different frequencies. So it is realistic that the damping and therewith the time constants are similar but not identical.

Still, this finding is no proof for the field disturbance being a consequence of cryostat vibrations. The signal could originate from something else within the cryostat. Considering the peak-to-peak voltage measurements along the radial position of the cryostat ends (Fig. 4.18), provides further evidence for the connection of the field distortion and the cryostat vibration. The peak-to-peak voltage is a measure for the axial field (orthogonal to the cryostat ends) and it is significantly changing with the position. This allows an approximate reconstruction of the magnetic field distribution.

Assuming the field is generated by eddy currents on the cryostat ends provides the information, that the eddy current orientation (only considering the direction perpendicular to the line sampled by measurements) is inverting once between the inner and outer radius. A very simplified approach would be to locate the 'central' paths of responsible eddy currents at the positions where the sign of the peak-to-peak voltage alters.

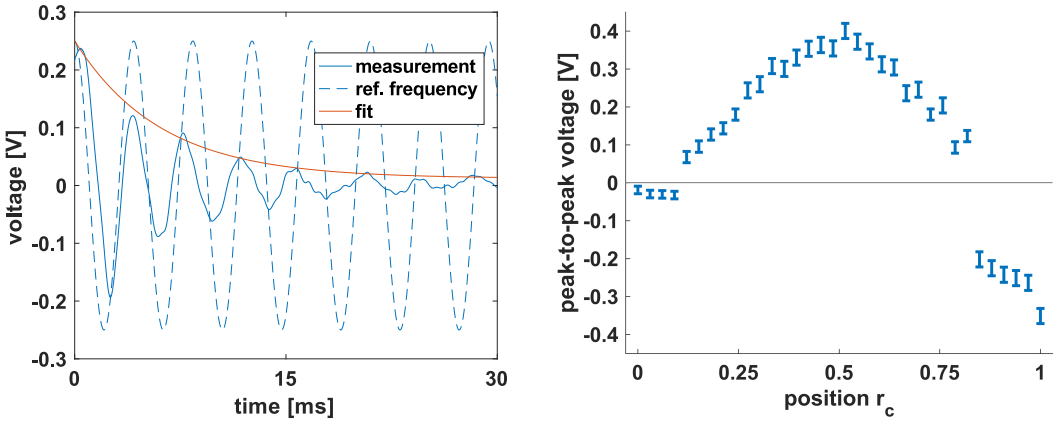

Figure 4.18 – Measurement results with the pickup coil along the axis of the investigated gradient at the cryostat ends. The signal with the maximal peak-to-peak voltage is exemplary shown on the left, including a virtual ongoing excitation signal (dashed) and an exponential fit (red) to the maximal peak values with a timeconstant of $6.2\,\mathrm{ms}$. Comparing the right plot, indicating the axial field distribution, with figure 4.19, suggests the presence of a first order radial mode on the cryostat ends, generating secondary eddy currents.

This observation would fit to the eddy current distribution produced by a first order mechanical mode in radial direction. Figure 4.19 gives an approximate impression of the expected eddy current paths and the resulting fields $\boldsymbol{B}_e$ generated by a first radial mode of the cryostat ends. The left picture illustrates a cross-section through the cryostat focusing on the cryogenic shield end. For simplicity, the illustration assumes that the ends (black horizontal line) are completely straight and the $\boldsymbol{B_0}$ field is symmetric to the central point of the ends. The dashed line represents the aspired mode shape of the ends.

Because of the inhomogeneity of $\boldsymbol{B_0}$ the movement of the ends induces eddy currents I, which, generate a magnetic field to minimize the change of magnetic flux through the ends. As discussed in section 4.1.2, particularly with figure 4.3, the magnetic flux changes can be separated into two main contributions.
Due to the changing position of the conductive layer, the amplitude of the orthogonal magnetic field component is altered. This amplitude is either increasing or decreasing for the entire first order mode shape, depending on whether the movement is directed towards or away from the main coils. So the eddy currents will produce a

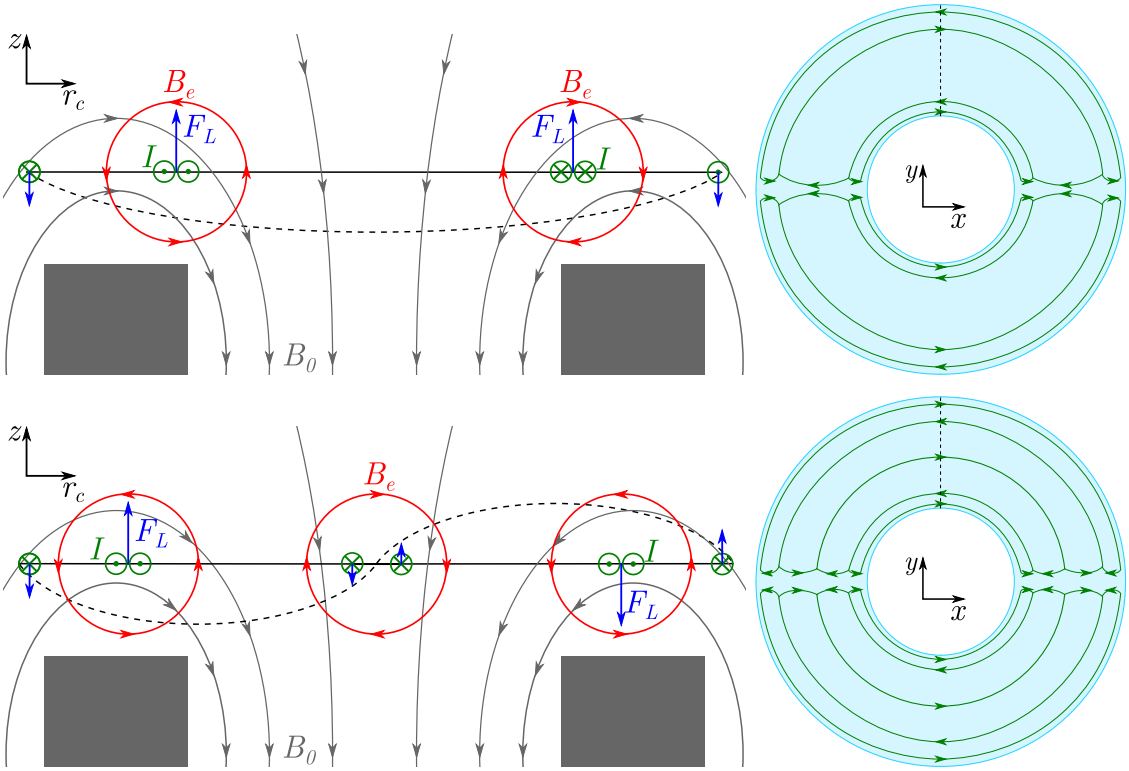

Figure 4.19 – Schematic illustrations of the magnetic fields $\boldsymbol{B_e}$ (red) generated by a movement of the cryostat ends (dashed line) in their first (top) and second (bottom) radial mode within the main magnetic field of the superconductors (gray). The eddy current distribution $\boldsymbol{I}$ (green) tries to prevent the movement via their interaction with the radial component of $\boldsymbol{B_0}$, generating Lorentz forces $\boldsymbol{F_L}$ (blue). Radial Lorentz forces are not drawn in the image. The right illustrations give examples of the eddy current paths regarding an entire cryostat end in a plane view. Here the dashed line indicates the position of the cross-section pictured on the left.

magnetic field of similar qualitative shape as the axial $\boldsymbol{B_0}$, trying to compensate this primarily distance dependent variation. Consequently, the eddy currents are arranged along r_c comparable to the main coil windings. Since the modal displacement is largest in the center, the main eddy current paths are shifted towards the center.

The second contribution to the change of magnetic flux occurs due to the larger area, which is exposed to the radial $\boldsymbol{B_0}$ field by the movement. The orientation of the radial $\boldsymbol{B_0}$ component alters once along the mode length, generating two eddy current loops. Superimposing these with the first described induced cur-

rents gives the main eddy current paths as documented in the picture. In total and according to Lenz's law, the sum of the resulting Lorentz forces is oriented to counteract on the movement. For clarity reasons the drawings only consider axial forces.

The frontal view on the ends on the right of the figure contains the anticipated eddy current paths for a first radial mode when it excited by a Y-gradient. The dashed line indicates the position of the cross-section illustrated on the left. The movement of the upper and lower part are anti-symmetric.

Considering an asymmetry as given in the real magnet-cryostat-setup, where the outer main coil is positioned further away from the cryostat than the inner coil, results in a $\boldsymbol{B_0}$ field which is weaker at the outer half of the end than further inside. For the investigated magnets also the number of windings on the outer coils were less than on the inner ones, generating less magnetic field strength with the same driving current. Accordingly, the $\boldsymbol{B}_e$ amplitude is also smaller there, allowing the conclusion that the measured peak-to-peak voltages are in agreement with the theoretically expected situation.

To provide evidence that there is indeed an agreement between the measurements and the theoretical explanations, supplemental measurements are done on a different MRI system in section 4.3.4. If the measured peak-to-peak voltages are induced by a mechanical vibration, a similar spatial distribution should be observable, since comparable mode shapes at similar frequencies must exist as long as the geometry is comparable. Moreover, the pattern needs to change when a different mode is excited by changing the excitation frequency. A second order mode for example, as illustrated in the lower pictures of figure 4.19, should produce a local maximum and minimum in the peak-to-peak voltages along the measured line. Due to the spatial symmetries in the displacement and the magnetic field, the radial inner and outer half of the conductive layer possess a symmetric eddy current distribution as well. In order to minimize the change of magnetic flux generated by this mode shape, an additional current at the 'knot' in the center of the mode shape is needed. This leads to an optimized compensation of the flux change, since the axial component of $\boldsymbol{B}_e$ is strongest at positions where large displacements occur.

This section presented a series of measurements utilizing a pickup coil for measuring magnetic flux changes independently from the static magnetic background field. MR experiments are usually limited to the FOV, where the background field is homogeneous. The pickup coil measurements have confirmed, that the disturbing field, generating the ghosting artifacts seen in section 4.3.1 possess a constant non-zero amplitude distribution in the EPI read-out direction. The time constant of the decaying signal agrees with the ones obtained from the MR experiments, confirming that the field responsible for the ghosting is also measurable with the pickup coil. Measurements on the cryostat ends allowed to propose the shape of a cryostat movement, potentially responsible for the measured signal.

In the next section similar measurements with the pickup coil have been performed on an MRI system possessing 0.5 T field strength. The obtained results will prove that the signals measured by the pickup coil are a consequence of cryostat movements induced by magnetomechanical interactions.

4.3.4 Pickup coil measurements at 0.5 T

As mentioned in the section above, the proposed movement of cryostat ends (Fig. 4.19) generating the measured peak-to-peak voltages (Fig. 4.18 right), should be reproducible at other systems. To test this prediction, further loop coil measurements were conducted on an MRI system with similar cryostat dimensions and materials as the one of the preceding section. As an exception for experimental purposes, the system investigated in the following was operated at 0.5 T.

The similar geometry and composition of the cryostat ends should provide comparable mechanical eigenmodes and frequencies, which should thus produce similar results as above. The smaller field strength is of advantage, since the damping of the mechanical vibration should decrease with weaker Lorentz forces. As a result, the signal acquired by the pickup coil should be detectable over a longer time window, which allows a more accurate evaluation of the phase relationship. This reduced damping also needs to be considered for the duration of the exciting sinusoidal current. It needed to be expanded, to allow the oscillations to obtain a steady state. For the following measurements 24 periods proved to fulfill this requirement.

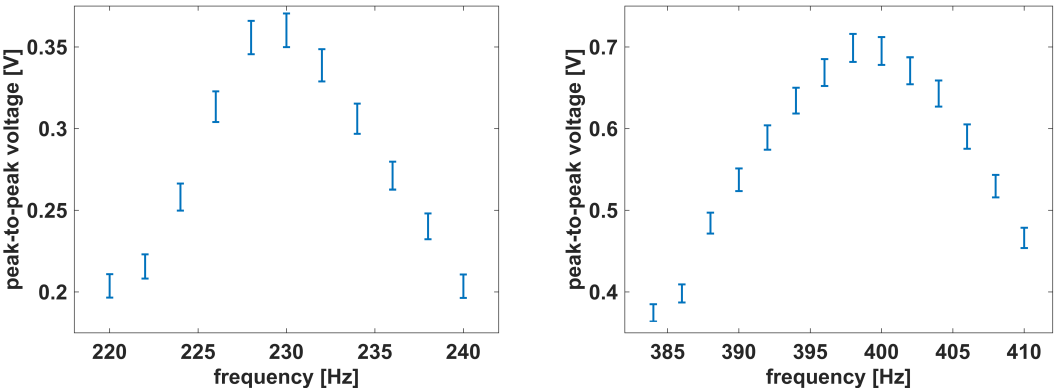

Figure 4.20 – Measurements for identifying eigenfrequencies of the mechanical modes of the cryostat ends on the 0.5 T system. The left plot shows a local maximum at 230 Hz, the right plot at 398 Hz.

The frequency for the excitation was determined by analyzing the peak-to-peak voltage over a broad frequency range. In case of a resonance, a local maximum should be observable. The coil position was deduced from the previous measurements (Fig. 4.18). At a quarter of the radial length of the cryostat the magnetic fields should provide sufficient signal for the first as well as the second radial mechanical mode. In figure 4.20 the spectra near the two investigated resonances at 230 Hz and 398 Hz are plotted.

Figure 4.21 shows the signal obtained at 230 Hz for two time windows. It is clearly visible in the left plot, that the signal is decaying significantly slower than at the 3 T system. This confirms the presence of stronger damping with increased field strength. At 3 T the signal was barely present after 30 ms (see Fig. 4.18 left) while at 0.5 T the oscillation is still observable after 60 ms. The temporal loss of signal amplitude at 15 ms, which recovers, suggests a beat oscillation. It is explained by a resonance excited on the inner bore at a slightly different frequency. The contribution of the interfering frequency appears to be minor, since the phase and frequency relation of the measured signal corresponds well to the excitation signal.

The dashed red line in the plots visualizes the virtually ongoing excitation signal, allowing to compare the frequencies and phases of the signals. The frequencies appear to be very similar in this case and the evaluation of the phase relationship yields a value close to

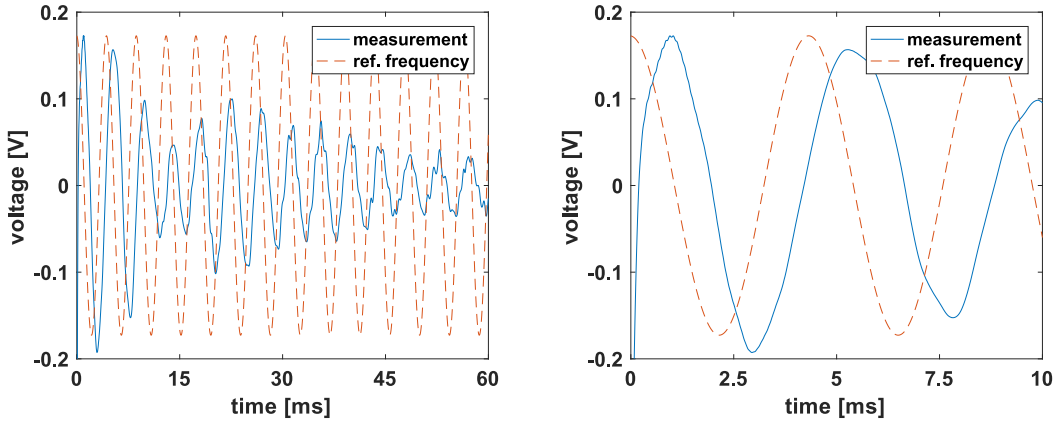

Figure 4.21 – Two plots, covering different time windows, of an exemplary signal acquired at a radial position of 0.25 after an excitation with $230\,\mathrm{Hz}$. The red dashed line again represents the virtually ongoing excitation to allow a frequency and phase comparison.

$\pi/2$. This can be seen in the right plot of figure 4.21, zooming in on the first $10\,\mathrm{ms}$. The phase relation was also determined mathematically by calculating a convolution of the measured signal $\mathcal{M}(t)$ with the virtual reference signal $\mathcal{V}(t,\vartheta)$, an oscillation with the frequency ω and amplitude $\mathcal{V}_0 \neq 0$.

$$\mathcal{C}(\vartheta) = \int_0^\infty \mathcal{M}(t)\ \mathcal{V}(t,\vartheta)dt = \int_0^\infty \mathcal{M}(t)\ \mathcal{V}_0 \mathrm{sin}(\omega t + \vartheta)dt \tag{4.27}$$

For the computation the integral obviously has to be discretized. The upper integration limit is set by the measurement duration or the point in time where the signal falls below the noise level. The value of ϑ, where $\mathcal{C}(\vartheta)$ becomes maximal marks the phase difference between the excitation and the measured signal, independent of $\mathcal{V}_0$. This approach is only reasonable as long as $\mathcal{M}(t)$ possesses the same periodicity as $\mathcal{V}(t,\vartheta)$. For the calculation of the phase it offers the advantage that it automatically includes the amplitude and therewith the quality of the measured signal. The noisy signal at later time points is not corrupting the evaluation as much as it would e.g. in a least-square fit.

For the exemplary signal of figure 4.21 this method yields a phase difference of $\vartheta \approx \pi/2 + 0.021 \mathrel{\hat{=}} 91.2°$. Considering the degrading quality of the measured signal over time and the presence of the beat oscillation, this result is in good agreement

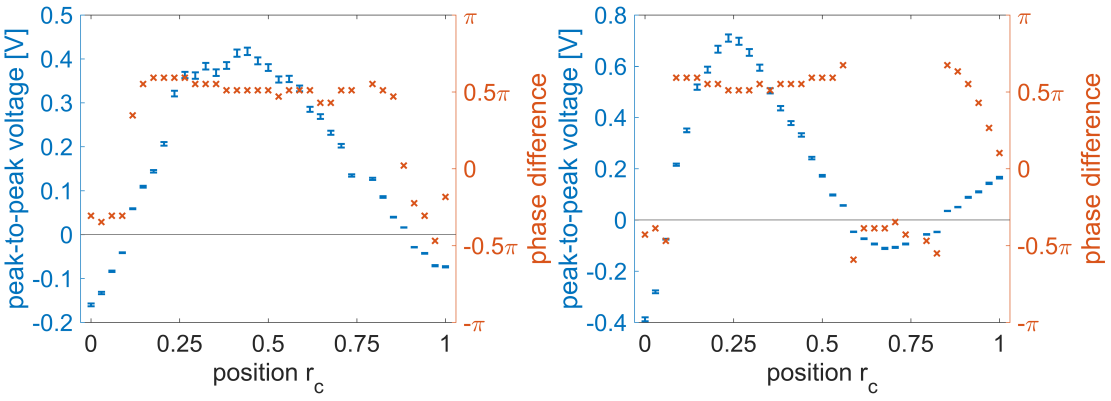

Figure 4.22 – The measurement results for the spatial distribution of the peak-to-peak voltages along the cryostat ends with an excitation frequency of $230\,\mathrm{Hz}$ (left) and $398\,\mathrm{Hz}$ (right). In addition the phase between the excitation and the signal is plotted in red. Comparing the results to the figure 4.19, allows an assignment of the two measurement series to mechanical vibration modes of the CS ends. The first order radial mode can be assigned to the left plot and second order mode to the right plot.

with the theoretically derived value for magnetomechanically generated secondary fields (Sec. 4.1.2). To support this result with additional measurements, ϑ was also calculated for the following measurements, varying the pickup coil position.

For both resonance frequencies, determined by the peak-to-peak voltage spectra (Fig.4.20), the measurement along the radial length of the ends was performed. The setup was identical to the measurements done for obtaining the right plot of figure 4.18, with the excitation frequency and the duration adapted.

The results of these measurements are presented in figure 4.22. In the left plot ($230\,\mathrm{Hz}$) the peak-to-peak voltages (blue) show a distribution very similar to the one seen at the 3 T system measurements (see Fig. 4.18) associated with a first order radial vibration mode. In the right plot ($398\,\mathrm{Hz}$) one can see a clear change of the distribution. This distribution fits to the expectations for a second order mode, containing a local maximum and minimum. The smaller amplitudes towards the larger radial positions are reasonable, since the $\boldsymbol{B_0}$ field is, in practice, weaker at the outer radial positions than illustrated in the symmetric drawing of figure 4.22.

As long as the peak-to-peak voltages are high, the phase values (plotted red in both plots on the according right axes) are close to $\pm\pi/2$. The phase relationship between the exciting signal and the response signal due to movement is expected to have this value, if a magnetomechanical resonance is excited (see Sec. 4.1.2). The deviations from $\pm\pi/2$ for small peak-to-peak voltages are not considered relevant. In the case of the according small signals, the beat oscillation and the relatively high noise prevent a correct calculation of the phase value, leading to the observed deviations.

Section 4.3 started with presenting an EPI ghosting artifact at a 3 T system, which could be ascribed to an undesired field oscillation in the FOV with varying amplitude. The oscillation was reproduced using a simple MR experiment, allowing the identification of a clear exponential decay or respectively an onset behavior of the oscillation. The spatial origin of the disturbance field is, however, not traceable with MR measures due to the limitation of this type of measurements to the comparably small region of the FOV.

Simulations were not suitable for this problem as well, since the field distribution appeared to be symmetric in space, which demands a break of the anti-symmetry of the gradient fields. Current simulation approaches simplify the real geometry of the setup to enable simulations at all, including the assumption of clear symmetry relations. Without knowledge of the cause for the symmetry breaking effect, a correct reproduction by simulation is almost impossible.

Hence, additional measurements were conducted using a pickup coil, allowing field measurements in- and outside of the FOV. Although the quality of the signal acquired with the pickup coil is spoiled relatively strong by noise and other interferences, it was possible to reproduce the spatial distribution of the disturbance in the FOV. Consequently, it is proven, that the disturbance is not generated in the RF transmit or receive chain of the MRI system. The pickup coil measurements within the magnet bore also show that the signal increases the closer the coil is positioned to the MRI cryostat. This behavior suggests that the origin of the disturbance lies within the MRI cryostat.

To improve the signal quality measured by the pickup coil, it was positioned at the cryostat ends. The signal obtained there showed a time constant comparable to the one seen in the MR measurements. Yet, the frequency of the signal was different, suggesting that the disturbing signal responsible for the ghosting artifact originates at the inner bore. Sampling the signal spatially from the inner to the outer bore, allowed the identification of a potential mechanical mode shape. The same result was generated on another system with 0.5 T field strength, possessing longer time constants, which allowed more accurate evaluations of the pickup coil signals. This reduced time constant is another indicator for the magnetomechanical nature of the oscillation, since this behavior is expected for mechanical oscillations taking place in differently strong magnetic fields.

Finally, the evaluation of the distinct change in the signal distribution along the radial length of the ends, when varying the excitation frequency, showed that mechanical resonances of the MRI cryostat vessels generate measurable magnetic field oscillations.

5 Discussion

The two preceding chapters presented various simulations and measurements to document magnetomechanical interactions in different MRI systems. Combining all findings provides the conclusion that particular EPI ghosting artifacts are caused by vibrations of the MRI cryostat, dominantly of the cryogenic shield. This allows to propose dedicated countermeasures. One promising measure, which was successfully applied for a prototype setup, is a GC stray field optimization using modal participation factors.

For demonstrating the connection between cryostat-movement induced field effects and corrupted imaging, an exemplary ghosting artifact was analyzed via various experiments. It was possible to track the origin of these oscillations down to the inner bores of the magnet cryostat. Due to better accessibility, further measurements were conducted on the ends of the cryostat, allowing to identify a frequency dependent spatial distribution of these disturbances. From this spatial distribution, it was possible to derive according vibration shapes of the cryostat, being a strong indicator for ascribing the cause of the disturbing magnetic field to such vibrations. This knowledge can be used to expand already existing phase correction methods, which aim on reducing the ghosting artifacts by compensating the effect of disturbing fields in a post-processing step. A measurement of the CS movement simultaneously with the EPI scan can provide information on the strength and time dependency of the occurring disturbance and would allow the dedicated compensation of the resulting effects. Further research on the presented simulation approach also has the potential to gather this information purely computational.

A deeper insight into the processes, responsible for the disturbing fields, was gained by simulations of the interactions between the gradient stray field and the cryostat. This way achieved by a novel 3D FEM framework, allowing the simulation of all three

gradient axes. By applying this framework for the analysis of the ECL behavior of various GC prototypes in different magnets, it was demonstrated, that the magnetomechanical interactions, generating the strongest secondary eddy currents, happen on the CS. An indicator for this is the high correlation found between the kinetic energy of the CS and the ECL on the HeV. When the CS is moving strongly, also high ECL on the HeV is observed. The movement of the CS generates secondary eddy currents, which emit fields, that induce eddy currents (and according losses) in the HeV. That the secondary effects taking place on the OVC are of minor importance was shown by transient simulations. In these simulations the cryostat vessels were moved separately using dynamic mechanical boundary conditions, allowing the evaluation of according field effects in the FOV. These simulations confirmed the dominance of the CS in the magnetomechanical interactions, which is attributed to its material properties. The CS possesses a small density and a high conductivity in comparison to the OVC material. These circumstances lead to strong accelerations due to Lorentz forces and consequently high velocities generating the (problematic) secondary eddy currents.

Whereas the simulations show reliable results in the frequency range above $1500\,\mathrm{Hz}$, the quality and predictive power of the presented simulations is currently very limited for frequencies below $1500\,\mathrm{Hz}$. This can be explained by the different relevance of the CS components for the two frequency ranges. Above $1500\,\mathrm{Hz}$ the major magnetomechanical effects are observed at the CS inner bore, the cylindrical tube between GC and main magnet coils. Below $1500\,\mathrm{Hz}$ the CS ends, connecting the inner and the outer bore tubes, are also relevant for the system behavior. This higher influence of the cryostat ends requires a more detailed description of their properties, including the geometrical transitions to the inner and outer bores. Current research is aiming to improve the FE-model in this respect to better replicate the actual behavior. For this purpose the pickup coil measurements, identifying eigenfrequencies and mode shapes of resonances, can be a helpful tool for comparing and calibrating the simulation model.

In addition to the importance of the CS ends, the simulations revealed a pattern in the mode structure of the CS inner bore, separating the frequency regimes above and below $1500\,\mathrm{Hz}$. For higher frequencies basic cylinder modes with a circumferential order of 1 occur and dominate the ECL spectra. In the low frequency range only cylinder

modes with higher circumferential order could be found. Despite the lack of accuracy in the low frequency range, this identified pattern allowed a GC design optimization, reducing ghosting artifacts in echo-planar-imaging.
Using modal participation factors, derived from the spatial distributions of the GC stray field and the main magnetic field on the CS inner bore, it is possible to analyze how strongly these modes with higher circumferential order are principally excited for a given GC-magnet setup. A modification of the GC stray field, which reduced the according PFs, has shown a clear decrease in the EPI ghosting level and in simulations of the field effects in the FOV. This method can potentially be included into the design process of gradient coils, describing additional constraints for the optimization of the conductor pattern. An upper limit for PF values of predefined cryostat modes (expected to be crucial) could be a simple example for such a constraint. Therewith, the optimization of the magnetomechanical PFs is considered a valuable tool for designing gradient coils, being able to support ECL as well as EPI ghosting reduction and potentially further effects involving cryostat vibration.
Taking all presented observations into account, particularly the successful mitigation of EPI ghosting with the systematic GC design optimization, this thesis provides evidence that magnetomechanical interactions within the cryostat potentially corrupt MR images.

Other measures than GC stray field modifications for reducing the excitation of the problematic cryostat vibrations could be changes to the architecture or material properties of the cryostat. For example systematic slits to prevent according eddy currents or additional structures to stiffen the mechanics could be introduced. However, the implementation of such measures is also complex as it involves other considerations like the strongly restricted space within the cryostat or thermal shielding. Thus, the best choice for a first attempt to mitigate the excitation of undesired cryostat movement appeared to be an optimization of the GC stray field.

Although the FE-simulations presented can not provide quantitatively precise results for general applications, yet, the qualitative and especially comparative statements deduced from the simulations proved to be valid. As a consequence, the simulations are preferably applied to improve performances of GCs for which related measurement data are already available.

Reasons for the quantitative differences between computations and measurements are manifold. The common denominator is the necessity to simplify the real setups making simulations feasible at all. These simplifications start on large scales, by limited model sizes and implying symmetries that are not perfect, and ends on small scales, by discretizing the FE-mesh with linear or quadratic ansatz functions although the effect to be described is behaving exponentially (e.g. skin effect). Without any claim for completeness some other aspects to mention are material parameters, which are all based on more or less precise measurements or experience values and are assumed to be ideal isotropic. Moreover, the damping in the system is not considered correctly, as was seen in section 3.1.5, and construction tolerances can have essential influence for local effects or individual systems (see Sec. 3.2.2). Lastly, many physical effects are purposely neglected, for example magnetoresistance, movements of the coils themselves due to eddy currents and crosstalk of different GC axis. It is still worked on identifying the inaccuracies majorly responsible for the quantitative mismatches.

The experiments and simulations presented, have created a deeper insight into the magnetomechanical interactions in clinical MRI cryostats. They allowed a systematical optimization of gradient coil designs in respect of EPI ghosting and eddy current losses heating the cryostat. The former can improve the reliability of EPI used in diagnostic imaging without additional time consuming and potentially erroneous ghosting correction methods. This advantage results from addressing the root cause of the problematic field disturbance, the excitation of mechanical cryostat resonances.
The reduction of eddy current losses in the cryostat can help to construct MRI systems that operate safely with less cooling demands and therewith less energy consumption. Eventually, the achieved advances in the simulation framework can help to accelerate the development of superconducting MRI systems that can be operated without liquid helium baths for the main magnet.

References

[1] P. C. Lauterbur. Image Formation by Induced Local Interactions: Examples Employing Nuclear Magnetic Resonance. *Nature*, 242(5394):190–1, 1973.

[2] M. Rausch, G. Gebhardt, M. Kaltenbacher, and H. Landes. Magnetomechanical field computations of a clinical magnetic resonance imaging (MRI) Scanner. *Compel*, 22(3):576–88, 2003.

[3] M. Rausch, G. Gebhardt, M. Kaltenbacher, and H. Landes. Computer-aided design of clinical resonance imaging scanners by coupled magnetomechanical-acoustic modelling. *IEEE Transactions on Magnetics*, 41(1):72–81, 2005.

[4] P. D. Ledger, A.J. Gil, R. Poya, M. Kruip, I. Wilkinson, and S. Bagwell. Solution of an industrial relevant coupled magneto-mechanical problem set on an axisymmetric domain. *Applied Mathematical Modelling*, 40(3):1959–71, 2016.

[5] W. Pauli. Über den Einfluss der Geschwindigkeitsabhängigkeit der Elektronenmasse auf den Zeemaneffekt. *Zeitschrift für Physik*, 31(373), 1925.

[6] W. Demtröder. Kern-, teilchen- und astrophysik. *Springer-Verlag*, Berlin, Germany, second edition, 2005, ISBN: 3540214518.

[7] C. P. Slichter. Principles of Magnetic Resonance. *Springer-Verlag*, Berlin, Germany, 3rd ed., 1990, ISBN: 9783540501576.

[8] D. W. McRobbie, E. A. Moore, M. J. Graves, and M. R. Prince. MRI: From Picture to Proton. *Cambridge University Press*, Cambridge, UK, 2006, ISBN: 9780521865272.

[9] M.F. Reiser, W. Semmler, and H. Hricak. Magnetic Resonance Tomography. *Springer-Verlag*, Berlin, Germany, 3rd ed., 2008, ISBN: 9783540293545.

[10] J. Larmor. On the Theory of the Magnetic Influence on Spectra; and on the Radiation from moving ions. *Philosophical Magazine*, 44(271):503–512, 1897.

[11] A. Abragam. The Principles of Magnetic Resonance. *Oxford University Press*, London, UK, 1961 reprinted from corrected sheets 1973.

[12] E. L. Hahn. Spin Echos. *Physical Review*, 80:580–594, 1950.

[13] E. L. Hahn. Detection of sea-water motion by nuclear precession. *Journal of Geophysical Research*, 65(2):776–777, 1960.

[14] M. E. Haacke, R. W. Brown, M. R. Thompson, and R. Venkatesan. Magnetic Resonance Imaging. Physical Principles and Sequence Design. *John Wiley & Sons*, NS, 1999, ISBN: 9780471351283.

[15] D. B. Plewes and W. Kucharczyk. Physics of MRI: a primer. *Journal of magnetic resonance imaging : JMRI*, 35(5):1038–54, 2012.

[16] J.MLS. Hutchinson, R.J. Sutherland, and J.R. Mallard. NMR Imaging: Image recovery under magnetic fields with large non-uniformities. *Journal of Physics E.*, 11:217–221, 1978.

[17] M. A. Bernstein, K. F. King, and X. J. Zhou. Handbook MRI Pulse Sequences. *Elsevier Academic Press*, Burlington, Massachusetts, USA, 2004, ISBN: 9780120928613.

[18] A. Kumar, Welti D., and Ernst R. R. NMR Fourier zeugmatography. *Journal of Magnetic Resonance*, 18:69–83, 1975.

[19] Edelstein W. A., Hutchinson J. M. S., Johnson G., and Redpath T. Spin warp NMR imaging and applications to homan whole-body imaging. *Physics in Medicine & Biology*, 25(4):751–756, 1980.

[20] P. Mansfield. Multi-planar image formation using NMR spin echoes. *J. Phys. C: Solid State Phys*, 10(3), 1977.

[21] M. K. Stehling, R. Turner, and P. Mansfield. Echo-Planar Imaging: Magnetic Resonance Imaging in a Fraction of a second. *Science*, 254(5028):43–50, 1991.

[22] M. Poutstchi-Amin, S.A. Mirositz, J.J. Brown, R.C. McKinstry, and T. Li. Principles and applications of echo-planar imaging: a review for the general radiologist. *Radiographics*, 21(3):767–79, 2001.

[23] R. Turner, D. Le Bihan, J. Maier, R. Vavrek, L.K. Hedges, and Pekar J. Principles and applications of echo-planar imaging: a review for the general radiologist. *Radioology*, 177(2):407–14, 1990.

[24] H. C. Torrey. Bloch Equations with Diffusion Terms. *Physical Review*, 104(3):563–5, 1956.

[25] D. Le Bihan, E. Breton, D. Lallemand, P. Grenier, E. Cabanis, and M. Laval-Jeantet. MR imaging of intravoxel incoherent motions: application to diffusion and perfusion in neurologic disorders. *Radiology*, 161(2):401–7, 1986.

[26] DIN EN 60601-2-33, Medical electrical equipment - Part 2-33: Particular requirements for the basic safety and essential performance of magnetic resonance equipment for medical diagnosis (IEC 60601-2-33:2010), November 2017.

[27] O.C. Zienkiewicz and R.L. Taylor. The Finite Element Method. *Butterworth - Heinemann*, 2, 2003.

[28] K.-J. Bathe. Finite Element Procedures. *Prentice Hall*, Upper Sadle River, New Jersey, USA, 1996, ISBN: 0133014584.

[29] T.J.R. Hughes. The Finite Element Method. LinearStatic and Dynamic Finite Element Analysis. *Prientice Hall*, 1987.

[30] M. Kaltenbacher. Numerical Simulation of Mechatronic Sensors and Actuators. *Springer-Verlag*, Berlin Heidelberg, Germany, second edition, 2007, ISBN: 9783540713593.

[31] D. V. Hutton. Fundamentals of finite element analysis. *McGraw-Hilll*, New York, New York, USA, 2004, ISBN: 0071122311.

[32] T. Belytschko, W.K. Lui, and B. Moran. Nonlinear Finite Elements for Continua and Structures. *Wiley*, 2000.

[33] K. J. Binns, P. J. Lawrenson, and Trowbridge C.W. The Analytical and Numerical Solution of Electric and Magnetic Fields. *Wiley*, Chichester, 1993, ISBN: 9780471924609.

[34] H. Landes. Technical report. Coupled Magneto-Mechanical Solver for B_0 coupling. *WisSoft*, Erlangen, Germany, 2008.

[35] H. Landes, M. Kaltenbacher, M. Ertl, A. Lohfink, and A. Krug. Oral presentation. Eigenvalue Problems for Coupled Magneto-Mechanical Systems. *CADFEM Users conference*, Stuttgart, Germany, 2006.

[36] H. Landes, P. Dietz, A. Krug, and A. vom Stein. Oral presentation. Simulations in Ultra-High-Field MAgnetic Resonance Imaging. *ANSYS Conference & 28th CADFEM Users' Meeting*, Aachen, Germany, 2010.

[37] H. Kerner and W. von Wahl. Mathematik für Physiker. *Springer*, Berlin Heidelberg, Germany, second edition, 2006, ISBN: 9783540724797.

[38] C. A. Ströhlein, A. Krug, and H. Landes. Feldstörungen und Wirbelstromverluste in MRT Systemen aufgrund magneto-mechanischer Interaktionen. *Proceedings of the 34th CADFEM ANSYS Simulation Conference in Nuremberg, CADFEM GmbH*, Grafing bei München; Germany, 2016, ISBN: 3937523138.

[39] J.P. Webb. Edge Elements and what they can do for you. *IEEE Transactions on Magnetics*, 29(2):1460–1465, 1993.

[40] H. Whitney. Geometric Integration Theory. *Princeton Univ. Press*, 1957.

[41] J.C. Nédélec. Mixed finite elements in $\mathbb{R}^3$. *Numer. Math.*, 35:315–341, 1980.

[42] A. Bossavit and J.C. Verite. A mixed FEM-BIEM method to solve 3-D eddy current problems. *IEEE Transactions on Magnetics*, 18:431–435, 1982.

[43] J.S. Welij. Calculation of eddy current in terms of H on hexahedra. *IEEE Transactions on Magnetics*, 21:2239–2241, 1985.

[44] G. Mur and A.T. Hoop. A finite-element method for computing three-dimensional electromagnetic fields in inhomogeneous media. *IEEE Transactions on Magnetics*, 21:2188–2191, 1985.

[45] A. Kameari. Three dimensional eddy current calculation using edge elements for magnetic vector potential. *Applied Electromagnetics in Materials*, pages 225–236, 1989.

[46] G. Mur. Edge Elements, their Advantages and their Disadvantages. *IEEE Transactions on Magnetics*, 30(5):3552–3557, 1994.

[47] G. Mur. The fallacy of edge elements. *IEEE Transactions on Magnetics*, 34(5):3244–3247, 1998.

[48] M. Jung and Langer U. Methode der finiten Elemente für Ingenieure. *Teubner*, 2001, ISBN: 9783519029731.

[49] T. Fließbach. Mechanik - Lehrbuch zur Theoretischen Physik 1. *Springer-Verlag*, Berlin Heidelberg, Germany, seventh edition, 2015, ISBN: 9783642554315.

[50] L. K. Urankar. Vector potential and magnetic field of current-carrying finite arc segment in analytical form, Part III: Exact computation for rectangular cross section. *IEEE Transactions on Magnetics*, 18:1860–1867, 1982.

[51] C. A. Ströhlein, A. Krug, A. vom Endt, P. Dietz, and H. Landes. Modelloptimierung mittels modaler Partizipationsfaktoren für Simulationen von Magnet-Resonanz-Tomographen. *Proceedings of the 35th CADFEM ANSYS Simulation Conference in Koblenz, CADFEM GmbH*, Grafing bei München; Germany, 2017, ISBN: 3937523146.

[52] L. D. Landau and E. M. Lifschitz. Lehrbuch der theoretischen Physik III - Quantenmechanik. *Akademie-Verlag*, Berlin, Germany, 1979, ISBN: 3055000676.

[53] M. H. Buonocore and L. Gao. Ghost artifact reduction for echo planar imaging using image phase correction. *Magnetic Resonance in Medicine*, 38(1):89–100, 1997.

[54] D. Xu, K. F. King, Y. Zur, and R. S. Hinks. Robust 2D Phase Correction for Echo Planar Imaging Under a Tight Field-of-View. *Magnetic Resonance in Medicine*, 64(6):1800–13, 2010.

[55] F. Schmitt and G. Goertler. Method for suppressing image artifacts in a magnetic resonance imaging apparatus . *US patent*, 5138259A, 22 February, 1990.

[56] H. Bruder, H. Fischer, H.-E Reinfelder, and F. Schmitt. Image Reconstruction for Echo Planar Imaging with Nonequidistant k-Space Sampling. *Magnetic Resonance in Medicine*, 23(2):311–23, 1992.

[57] O. Heid. Robust EPI phase correction. *Proceedings of the 5th Annual Meeting of ISMRM*, 1997.

[58] S. B. Reeder, A. Z. Faranesh, E. Atalar, and E. R. McVeigh. A Novel Object-Independent "Balanced" Reference Scan for Echo-Planar Imaging. *Magnetic Resonance in Medicine*, 9(6):847–52, 1999.

[59] S. M. Grieve, A. M. Blamire, and P. Styles. Elimination of Nyquist ghosting caused by read-out to phase-encode gradient cross-terms in EPI. *Magnetic Resonance in Medicine*, 47(2):337–43, 2002.

[60] N.-k. Chen and A. M. Wyrwicz. Removal of EPI Nyquist ghost artifacts with two-dimensional phase correction. *Magnetic Resonance in Medicine*, 51(6):1247–53, 2004.

[61] R. S. Hinks, B. J. Mock, F. J. Frigo, and Zhao X. Method and apparatus of echo planar imaging with real-time determination of phase correction coefficients. *US patent*, 7259557B2, 19 October, 2005.

[62] T. Feiweier. Method and apparatus for reduction of nyquist ghosts in medical magnetic resonance imaging. *US patent*, 7403002B2, 26 August, 2005.

A Appendices

A.1 Spectrum of a triangle waveform

In addition to section 3.1.1 the frequency spectrum of a triangle wave with frequency $\omega = \frac{2\pi}{T}$ is computed. Due to the periodicity of the waveform the calculation can be limited to one periodic cycle. In the interval $[0,\, T]$ the function give in the right plot of figure 3.1 is defines as

$$I(t) = \begin{cases} I_0 \left(\frac{1}{2} - \frac{2t}{T}\right) & \text{for } t \in \left[0,\, \frac{T}{2}\right[\\ I_0 \left(\frac{2t}{T} - \frac{3}{2}\right) & \text{for } t \in \left[\frac{T}{2},\, T\right[\end{cases} \tag{A.1}$$

The symmetry concerning $\frac{T}{2}$ demands that the Fourier coefficients b_n (see Eqs. 3.5) are 0. $a_0 = 0$ (given by Eq. 3.4) is obvious since the waveform is alternating around zero. For the remaining coefficients a_n with $n > 0$ the computation can be simplified to

$$\begin{aligned} a_n &= \frac{I_0}{T} \int_0^{T/2} \cos(n\omega t)\, dt - \frac{4I_0}{T^2} \int_0^{T/2} t \cos(n\omega t)\, dt = \\ &= 0 - \frac{4I_0}{T^2} \left[(n\omega)^{-2} \left(\cos(n\omega t) + n\omega \sin(n\omega t)\right)\right]_0^{T/2} = \frac{1}{n^2}\, \frac{I_0}{\pi^2}(1 - \cos(n\pi)) \end{aligned} \tag{A.2}$$

A.2 Cylindrical and spherical coordinatesystems

The description of the cryostat and its behavior is mainly treated in an axial symmetric coordinate system, adapting to the cylindrical symmetry of the cryostat.

This coordinate system is related to the Cartesian coordinates via

$$\begin{aligned} x &= r_c \cos\varphi_c \\ y &= r_c \sin\varphi_c \\ z &= z \end{aligned} \tag{A.3}$$

where r_c, φ_c and z are named radial, circumferential and axial component of the cylindrical coordinate system.

For the calculation of the spherical harmonics (Eq. 4.22) it is practical to use a spherical coordinate system. It is described by the spherical radius r_s, the azimuth φ_s and the inclination θ_s, which are given by

$$\begin{aligned} x &= r_s \cos\varphi_s \sin\theta_s \\ y &= r_s \sin\varphi_s \sin\theta_s \\ z &= r_s \cos\theta_s \end{aligned} \tag{A.4}$$

A.3 Eddy current losses for Z-gradients in 2D and 3D

As described in section 3.2.1, a transition from 2D to 3D FE simulations also demanded a switching in the underlying element formulation from nodal to edge elements. It was demonstrated that the calculation of the transient magnetics is accurately possible with the edge formulation. This can also be confirmed for the linearized harmonic solution.

The design A of the optimized Z-gradient in section 3.1.6 was constructed in 3D via the rotation of the 2D mesh. Figure A.1 illustrates the comparison of the 2D and 3D results for the high frequency ECL. Besides minor mismatches, which can be explained by numerical inaccuracies, the agreement of the 2D and 3D simulations is excellent, justifying the three dimensional application of the method.

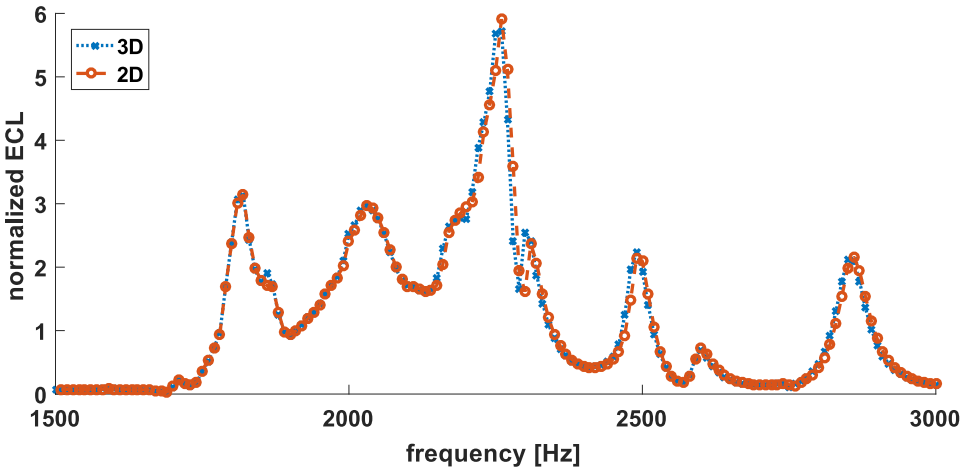

Figure A.1 – Simulated ECL spectra for an axial symmetric problem with a 2D and a 3D mesh. The results for both meshes agree with a high accuracy over the entire frequency range.

A.4 Biôt-Savart accuracy

For the application of the Biôt-Savart formulation (see Sec. 2.6.1) it has to be investigated, whether the FE Biôt-Savart method is calculating a magnetic field distribution sufficiently accurate, compared to the purely analytical formulation. Of special interest are the fields produced on the CS radius, since the strongest magnetomechanical interactions are expected there.

Two setups were investigated to assess the differences of the magnetic fields produced by a conductor modeled with its correct geometry and by a simplified Biôt-Savart line current. A 2D axial symmetric model with a single conductor pointing in normal direction of the plane is analyzed. As drawn in figure A.2 the magnetic field is evaluated along a line in z-direction at a radial distance $\Delta y = 30\,\mathrm{mm}$. The axial (z) and radial (y) dimensions of the conductor were $15\,\mathrm{mm}$ and $4\,\mathrm{mm}$ respectively, representing typical dimensions for secondary layer GC conductors.
The corresponding Biôt-Savart filament was positioned in the geometrical center of the conductor. Along the line of evaluation the element size was chosen to be $6\,\mathrm{mm}$ in accordance with axial resolutions utilized in the fully coupled simulations.

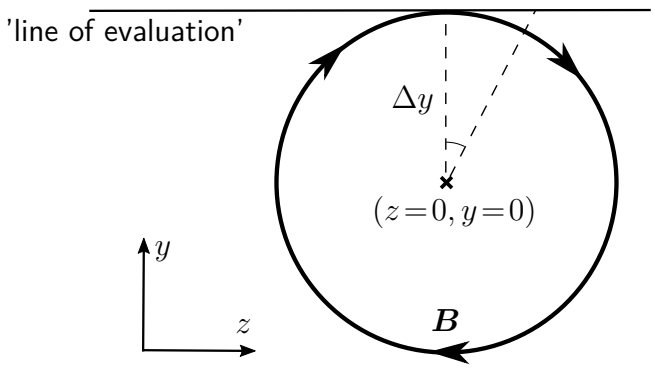

Figure A.2 – Illustration of the simulation setup for the investigation of the influence of the spatial extent of a typical GC conductor in comparison to a Biôt-Savart filament. The magnetic field $\boldsymbol{B}$, generated by a current carrying conductor, is evaluated along a line perpendicular to the conductor. The cross marks the geometrical center of the conductor and origin of the coordinate system. Δy is the distance to the line of evaluation.

The result of the comparison of the magnetic field magnitude simulated by the FE-conductor and the Biôt-Savart conductor are presented in figure A.3. The deviation at the peak value is $2.4\,\%$. The average difference in the surrounding $\pm 9\,$cm is $0.7\,\%$. This is an acceptable error margin, considering the differences which are introduced by construction tolerances (see Sec.3.2.2). Thus, the accuracy loss by the replacement of the FE-conductor by Biôt-Savart filaments is acceptable for the benefit of a simplified model construction.

In the second setup, the applicability of the Biôt-Savart formulation for 3D simulations is investigated in combination with the complexity of an entire Y-GC wire pattern. This time, the standard to compare to is the purely analytical Biôt-Savart calculation, that is employed in the design process of the GCs using Wolfram Mathematica. For the comparison a circumferential line over 90° on CS is evaluated with a 0.9° resolution. The result (Fig. A.4) yields differences smaller than 0.1% for the fields magnitude. Thus, the usage of FE Biôt-Savart filaments is unproblematic compared to other inaccuracies. Nonetheless, it should be mentioned, that coarsening the FE mesh in general increases the deviation of the Biôt-Savart approach and the analytical one.

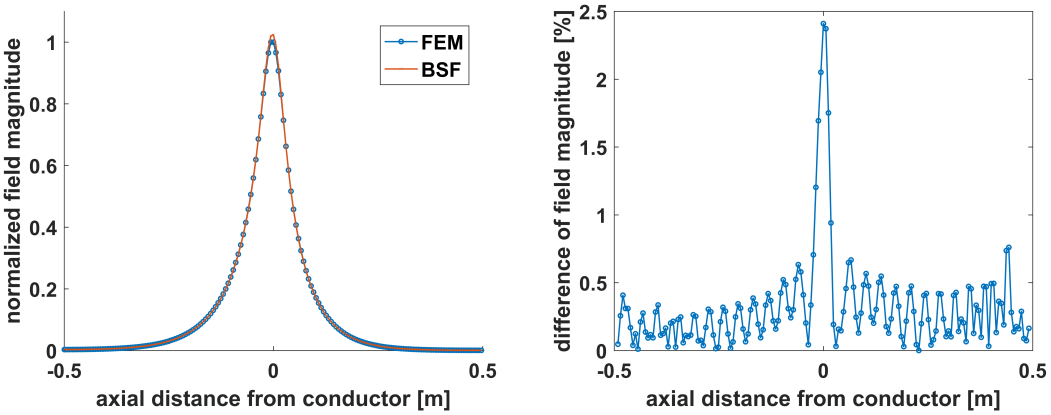

Figure A.3 – Two plots for comparing the magnetic field generated by a Biôt-Savart filament and a FE modeled conductor loop. The line of evaluation along the z-direction lies at a radial distance of $\Delta y = 30\,\mathrm{mm}$, which is a typical condition the positions of a secondary GC layer and the CS. On the left the field magnitude is plotted and on the right the difference of both fields in relation to the FE conductor values is shown.

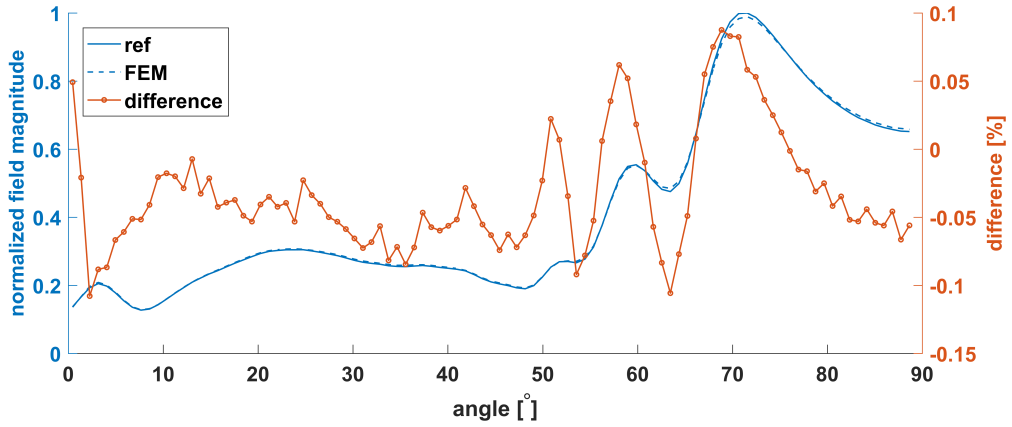

Figure A.4 – Comparison of Mathematica and FE Biôt-Savart field calculation. The magnetic field magnitude values obtained by the Biôt-Savart formulations are plotted on the left axis, normalized to the maximal value of the reference curve calculated with Wolfram Mathematica. The deviation of both calculations is plotted on the right axes and given as percentage of the reference values.

Acknowledgments

I would like to express my gratitude to Andreas Krug, Eva Eberlein and Peter Dietz who readily shared their knowledge and experience concerning MRI gradient coil development and beyond, giving orientation and advice over the years. Thank you for having confidence in me.

I wish to thank Wolfgang Nitz, the supervisor of this thesis, who assured that the focus of my research was not lost while granting me the freedom to follow my own approaches. I really appreciated the uncomplicated and honest correspondence, supplying expertise as well as a more general perspective.

A special acknowledgment goes to Hermann Landes for supporting me in countless discussions on numerical simulations and Finite Element modeling. Thank you so much for your time and humor.

My gratitude is also given to Annette Stein, Axel vom Endt, Daniel Niederlöhner, Gudrun Ruyters, Jens Grabinger, Martin Meiler, Michael Köhler and Stefan Dickopf, who provided support or solutions to various problems I came across.

Many thanks to all the persons mentioned above and the entire team of the 'gradient coil lab' for the friendly, respectful and simply comfortable working atmosphere I was allowed to be part of.

Lastly, needless to mention, I am grateful to my family and friends, having my back and taking care of everything else.